Fabrication and characterization of magnetic insulator Y3Fe5O12 thin films and measurement of the spin Seebeck effect by harmonic analysis.

Romanque Albornoz, Cristian Alberto

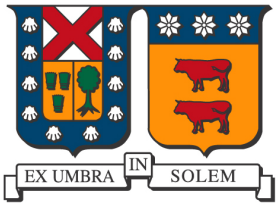

Universidad Técnica Federico Santa María
Departamento de Física

Fabrication and characterization of magnetic insulator $Y_3Fe_5O_{12}$ thin films and measurement of the spin Seebeck effect by harmonic analysis.

Cristian Alberto Romanque Albornoz

Valparaiso, Monday 25th July, 2022

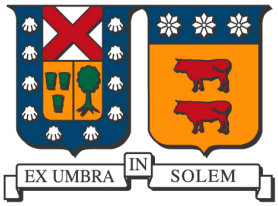

Universidad Técnica Federico Santa María
Departamento de Física

Fabrication and characterization of magnetic insulator $Y_3Fe_5O_{12}$ thin films and measurement of the spin Seebeck effect by harmonic analysis.

Tesis de grado presentada por

Cristian Alberto Romanque Albornoz

como requisito parcial para optar al grado de Doctor en Ciencias, mención Física

Supervisor:
Dr. Carlos Garcia Garcia

Valparaiso, Monday 25th July, 2022

TITULO DE LA TESIS:
Fabrication and characterization of magnetic insulator $Y_3Fe_5O_{12}$ thin films and measurement of the spin Seebeck effect by harmonic analysis.

AUTOR:
Cristian Alberto Romanque Albornoz

TRABAJO DE TESIS, presentado en cumplimiento parcial de los requisitos para el Grado de Doctor en ciencias mención Físicas de la Universidad Técnica Federico Santa María.

Dr. Carlos Garcia Garcia _____

Dr. Pedro Landeros Silva _____

Dr. Tomas Corrales Iturriaga _____

Dr. José Santiso López _____

Valparaiso, Monday 25$^{\text{th}}$ July, 2022

"No basta saber, se debe también aplicar.
No es suficiente querer, se debe también
hacer"
– *Goethe*

Esta tesis esta dedicada a mi familia
Alberto, Francisco y María

Contents

List of Figures

List of Tables

Chapter 1
Introduction

Nowadays, about two-thirds of the energy produced globally is dissipated into the environment in the form of waste thermal energy (or heat) and is projected to be one of the largest sources of sustainable, abundant, ubiquitous, inexpensive, clean, and fuel-free energy available in a natural and artificial environment [1]. Waste heat refers to the inevitable byproduct of power generation processes, industrial process or another process by using energy which is not put into a useful form like electricity and is lost, wasted or dumped into the local environment, *it simply vanishes into the surrounding environment*.

According to a report by Lawrence Livermore National Laboratory, more than 55 % of the primary energy produced in Chile in 2011 is rejected as waste heat [2]. Moreover, roughly more than 60% of primary energy worldwide is dissipated into the environment as waste heat over a wide range of temperature [3]. It is this huge amount of waste heat that human activities have caused and is continuing contribute directly or indirectly to the global warming [4]. Thus, energy harvesting of this waste-heat could have a significant role in reducing the environmental impact in industrial processes, transportation, residential usage and data centers, thereby reducing greenhouse gas emissions, and consequently helping in mitigating both energy and climate challenges [5, 6].

On the other hand, the exponential increase in computing power experimented in the last decades is accompanied by the down-scaling of electronic devices: a large number of transistors in an increasingly reduced area. In 1965 Gordon Moore predicted an exponential relation between the number of transistors per area unit and time [7], which states that the number of transistors on a silicon chip would double every year, later in 1975 this estimate was revised to a doubling every two years [8]. Indeed, recently the number of transistors on a central processing unit (CPU) has been reported as "50 billion transistors on a chip the size of a fingernail" [9]. However, the decrease in transistor size has fundamental limits reflected in the

available energy resources, properties of the physical space, a significant increase in energy consumption and unsustainable levels of ohmic energy wasted that then negatively impacts the performance of the chip [10, 11].

More than 60 years ago, in December of 1959 at a meeting given to the American Physical Society, Richard Feynman outlined a vision of what would later be called nanotechnology and spintronics [12], imagining *"that we could arrange atoms one by one, just as we want them"* and *"circuits that utilize quantized energy levels or the interaction of quantized spins"* [13].

The rapid advance to the miniaturization of electronic components brings us closer and closer to the critical point where quantum effects are increasingly relevant. But what is the limit? When Stephen Hawking was asked what are the fundamental limits to microelectronics, he said that the maximum limit was the speed of light and the size of a single atom [14]. Waste heat generated by electronics like CPUs is a complex problem. This can damage components, obstruct the reliable operation of the components and it represents a large amount of energy going to waste.

One way to recover these energy losses is by converting directly the waste heat into electricity by using thermoelectrics without any environmental pollution, using solid-state devices without moving parts [15]. A significant portion of this waste heat occurs as low-grade heat, below 232 °C [16, 17] ($>$ 50% of the total dissipated heat sources in industries), in this temperature range conventional thermoelectric devices are capable of recovering wasted heat and converting it into electricity, but is difficult to scavenge efficiently. The power conversion efficiency is limited by the small temperature differentials that are well below the fundamental Carnot limit, the maximum theoretical efficiency of a heat engine operating between a hot and a cold temperature, T_H and T_C, respectively, (also known as Carnot efficiency) [18] and their use is costly and impractical [19].

Spin caloritronics has recently emerged from the combination of spintronics, magnetism and thermoelectrics whose aims are the study the interaction between spin and charge in the presence of temperature bias and the generation and control of spin currents in solids and explore new material functionalities based on a spin-heat interconversion [20, 21]. Spin caloritronics is the spin analogue to the classical field of

thermoelectricity. Figure 1 shows a schematic illustration of interconversion process between differents particles or quasiparticles currents.

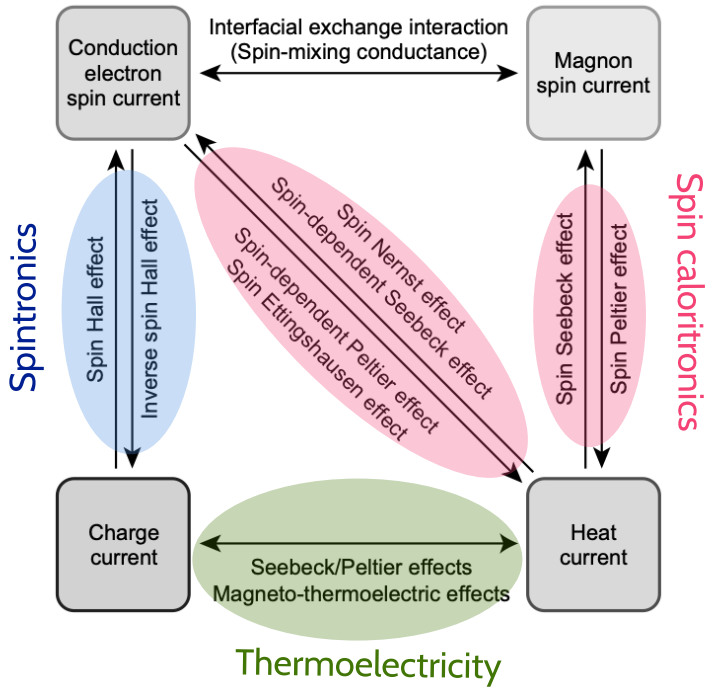

Figure 1. Schematic illustration of interconversion process between spin current, charge current and heat current. Adapted from reference [22].

The interaction of spin and heat gives rise to various physical phenomena and new functions in magnetic materials. For example, the spin Seebeck effect (SSE) generates pure spin currents owing to the magnetization dynamics induced by a temperature gradient applied across the interface of a magnet and a metal bilayer, this could lead to an efficient way to convert heat into electricity. Since the discovery of SSE in 2008 by Uchida *et al*. in a ferromagnetic metal (NiFe), it has been reported in a wide range of materials, including ferromagnetic semiconductors, non-magnetic materials [23] and ferromagnetic insulators. In the ferromagnetic layer, a spin current

is generated from the temperature gradient, and injected into the normal metal where it is transformed into a transverse usable electric voltage by inverse spin Hall effect (ISHE).

The study of spin caloritronics has drawn great interest in the last years because of their strong potential in power generation from waste, solar, geothermal or body heat through solid-state devices without: moving parts, emission of noise, vibrations, or pollutants also environmentally friendly materials, a task for which nanoscale systems are particularly suitable [24, 25]. Additionally, in contrast with the conventional thermoelectric technology, based on the coupling of heat and charge currents in conductors and semiconductors, thermal spin conversion has several advantages, for example the conversion efficiency in conventional thermoelectric devices is described by the dimensionless thermoelectric figure of merit (ZT):

$$ZT = S^2 \sigma T / \kappa \tag{1}$$

where κ is the electronic thermal conductivity, σ is the electrical conductivity, T is the operation temperature and S is the Seebeck coefficient. Consequently, in materials dominated by electronic thermal transport, ZT is strictly limited by the Wiedemann-Franz law (WFL) (1853) [26], given by equation 2, which establishes a link of proportionality between heat and charge transport due to electrons (and holes) in solids.

$$\kappa / \sigma = L_0 T \tag{2}$$

In the above equation, κ and σ are thermal and electrical conductivity respectively, $L_0 = 2.4 \times 10^{-8} J^2 K^{-2} C^{-2}$, for free electrons, is a constant called Lorenz number and T is the absolute temperature.

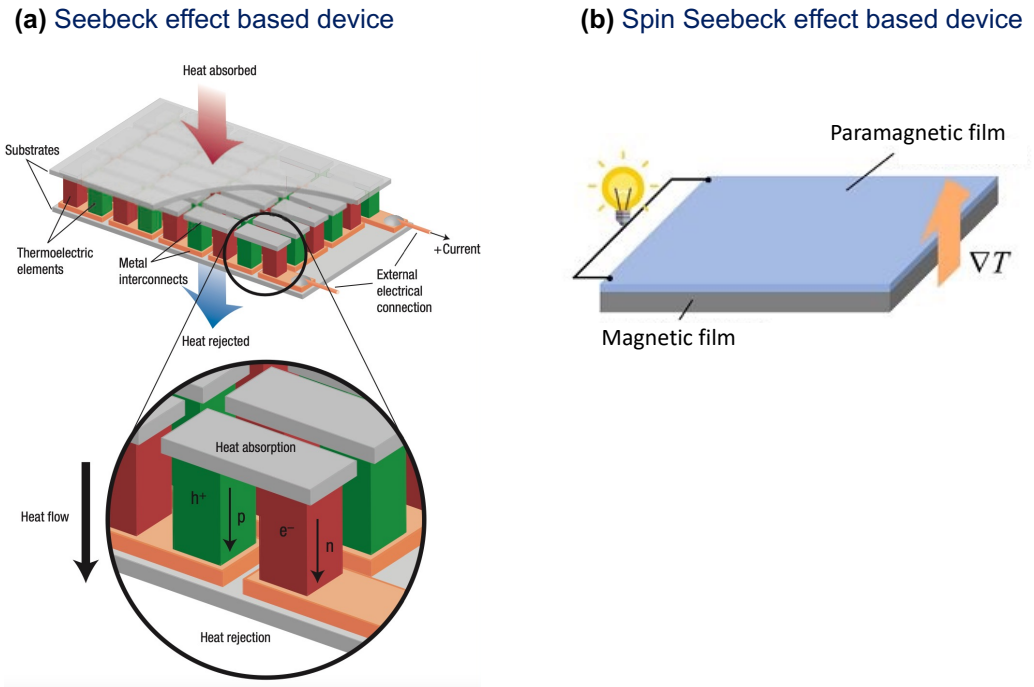

Figure 2. Comparison of conventional thermoelectric device based on the Seebeck effect and thermoelectric device based on the spin Seebeck effect. **(a)** A thermoelectric module made from thermocouple of p- and n-type thermoelectric legs. Image taken from [15] **(b)** The spin-Seebeck device consists of two thin film layers of metallic substances, or magnetic insulator and metallic substances. Adapted from reference [27].

As shown in figure 2(a), a conventional thermoelectric device consists of a series of thermocouples of n-type and p-type semiconductor elements (called legs). The thermocouples are electrically interconected in series but thermally connected in parallel [28]. In this standard configuration the thermoelectric device utilizes the longitudinal Seebeck effect, where the electrical current is generated in the direction parallel to an applied temperature gradient. This longitudinal configuration involves technical complexity in its manufacturing [29]. Nevertheless, the fundamental difficulty in thermoelectric technology is that σ and κ are mutually contraindicated in a given material. For efficient devices, good electric and poor thermal conductivity is required, vastly complicating the design [15]. As shown in figure 2(b), in thermal spin conversion based on SSE this limitation is overcome thanks to orthogonal paths for

heat and charge currents, that allows the flow through different parts of the sample, therefore free from WFL limitations. Also, this makes it possible to use at least two different materials that can be optimized independently, which allows that the SSE based device performance scales with extrinsic dimensions (enlarging the device area). These advantages of spin caloritronics over conventional thermoelectricity have potential to improve waste heat recovery rates, increasing energy efficiency.

Among one of the options that spin caloritronics offers, the use of magnetic insulators is particularly attractive, which offer the possibility of transporting spin currents through spin waves or magnons without the need for electron transport [30] , this is an advantage since in such materials the joule heating is insignificant [31]. The small energy losses in insulators enable transport of spin information across large distances in a micrometers scale [32, 33], much further than in metals. Within this group of materials, rare-earth iron garnets allow to tune their magnetic properties by doping with various elements.

1.1 Outline of this thesis

The present PhD. thesis is organized as follows. **Chapter 2** gives a general overview of the fundamental physics of spintronic, spin-dynamic and spin-caloritronics. **Chapter 3** begins as a brief overview of the magnetic insulator Yttrium Iron Garnet (YIG), it also introduces its physical properties and the sample preparation using pulsed laser deposition technique. The chapter continues with a description of the X-ray structural characterization techniques. Finally, I present the experimental results of the magnetic characterization performed using ferromagnetic resonance technique. Part of this chapter has been developed in collaboration with the group of Dr. Jose Santiso at the Institut Català de Nanociència i Nanotecnologia (ICN2) in Bellaterra (Barcelona), Spain. **Chapter 4** describes an alternative measurement technique for the longitudinal spin Seebeck effect, based on harmonic analysis of the signal measured in the YIG/Pt bilayer system. Finally **Chapter 5** concludes the thesis, and discusses the outlook for further experimental work on iron garnets and spin-caloritronic topics.

Chapter 2
Theoretical fundamentals

This chapter gives an overview of the theoretical background necessary to understand the experimental study presented in this thesis. It starts with a brief description of the theory of ferromagnetism, spin currents, spin waves and the mechanism for detecting it in thin films. After this general introductory section a closer look at the spin Seebeck effect basics will be made.

2.1 Ferromagnetism and magnetic insulators

Ferromagnets are materials that exhibit a spontaneous magnetization due to the alignment of the elementary permanent moments below a critical temperature called Curie temperature. The magnetization exists in the ferromagnetic material in the absence of an externally applied magnetic field, but above Curie temperature, thermal fluctuations destroy this alignment so the material becomes paramagnetic. Although these moments do interact via their dipolar magnetic fields, the interaction giving rise to the spontaneous alignment is orders of magnitude stronger and has a quantum mechanical origin. This is called the exchange interaction and is discussed in detail in subsection 2.3.

In some materials, the quantum mechanical coupling between moments is such that adjacent moments tend to line up along opposite directions. The long-range order can be described in terms of two anti-parallel interpenetrating ferromagnetic sublattices. If the net magnetizations of the two sublattices are equal and consequently the net magnetization is zero, the material is called an *antiferromagnet*. If the net magnetizations are unequal, the net magnetization will not cancel out hence having a spontaneous magnetization. This type of magnetic order is called *ferrimagnetism* [34, 35]. In general, ferrimagnets are not limited to two sublattices; the distinguishing characteristic is that the equilibrium magnetization of at least one of the sublattices must be opposite to the others. This arrangements are represented schematically in figure 3.

Materials of particular importance for microwave and spintronic applications are magnetic oxides known as ferrites and magnetic garnets [36, 37]. This material has some sort of magnetic order while being electrically insulating. In contrast to conducting magnetic materials, no parasitic currents can be induced into insulating ferromagnets. This simplifies the description of the dynamics of the materials and is advantageous for their use in spintronic applications.

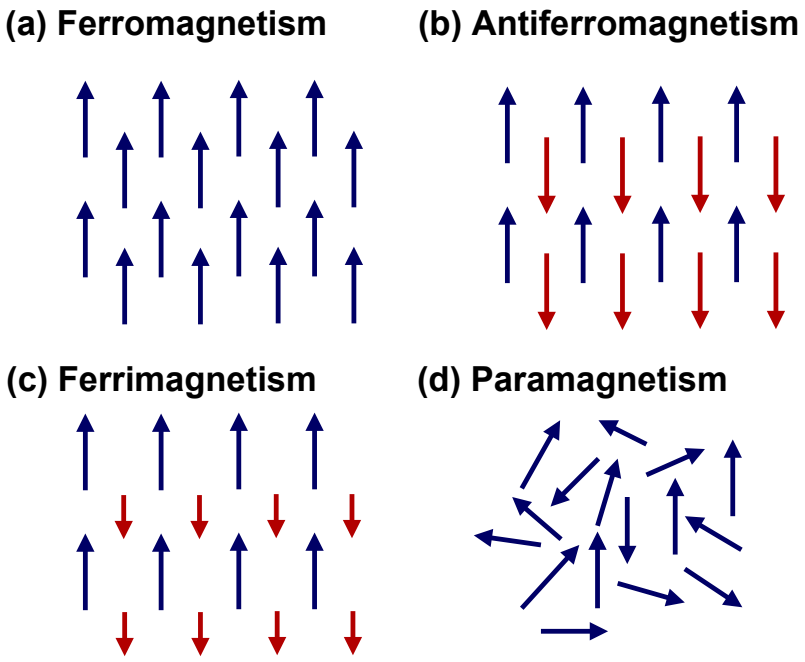

Figure 3. Two-dimensional qualitative models of fundamental magnetic orderings. **(a)** Ferromagnetism, **(b)** Antiferromagnetism, **(c)** Ferrimagnetism and **(d)** Paramagnetism: In the absence of an external magnetic field, the spins are randomly oriented, such that the material possesses no net macroscopic magnetization. Red arrow denotes a second magnetic sublattice.

2.2 Spin currents

An electron has three inherent properties; charge, mass and spin. The electron spin can be visualized as the angular momentum associated with the electron spinning around its axis. Nevertheless, this picture is certainly incomplete and should not be taken literally since this picture includes the fatal defect that the speed of rotation of electrons would have to be larger than the speed of light [38]. We know that

spin is an intrinsic angular momentum associated with elementary particles, which has no corresponding physical analogue in the macroscopic world. In late 1924, Wolfgang Pauli proposed that this angular momentum as an inner degree of freedom of the electron and only can have two quantized states [39], "spin-up" parallel to the quantization axis or "spin-down" along antiparallel direction. Pauli called this new quantum property of the electron a "two valuedness not describable classically" [40]. Thus we could imagine each electron being a tiny magnet, having a north-pole and south-pole.

The magnetism of materials is carried by electron spin, while electrical transport is carried by the motion of electron charge. The fields of magnetism and electrical transport have been developed almost independently, until the first convergence of these fields came in 1988, with the discovery of giant magnetoresistance (GMR) by Albert Fert [41] in France and Peter Grüenberg [42] in Germany. The pioneering work of Fert and Grünberg also led to the birth of a new field called spintronics, an acronym for spin transport electronics that was first introduced in 1996 to designate a program of the U.S. Defense Advanced Research Projects Agency (DARPA) [43]. Classical electronics exploits the electron charge to designate binary information, whereas in spintronics the spin of the electron is used for switching purposes and to communicate information. In this context, a new key concept emerges out: spin current.

Consider a continuous charge distribution in which the carrier velocity of a small volume is given by $\boldsymbol{v}_d$, then, neglecting relativistic effects, the charge current density is $\boldsymbol{j}_c = \rho \boldsymbol{v}_d$. If there are n electrons per unit volume, each with charge $-e$, then the charge density is $\rho = -ne$ and the current density is $\boldsymbol{j}_c = -ne\boldsymbol{v}_d$ [44]. As well as its mass and elemental charge, an electron has an intrinsic angular momentum, called spin. The spin is a quantum mechanical observable described by the spin angular momentum operator $\hat{\mathbf{S}}$. There are just two eigenstates that we can call spin-up ($\uparrow$) and spin-down ($\downarrow$) (projection of the electron spin in certain quantization axis) which correspond to the eigenvalues $\pm\frac{\hbar}{2}$, respectively[45]. As a consequence of this additional electron degree of freedom, the existence of a charge current implies the existence of a spin flow, called spin current [46].

In a picture suggested by N. Mott [47] and later derived from the Boltzmann transport theory, it is possible to distinguish between two carrier species: electrons in the spin-up state and electrons in the spin-down state, moving separately through individual channels. Each channel has its own charge current density $\boldsymbol{j}_{\uparrow} = -en_{\uparrow}\boldsymbol{v}_{d\uparrow}$ and $\boldsymbol{j}_{\downarrow} = -en_{\downarrow}\boldsymbol{v}_{d\downarrow}$, where $n_{\uparrow(\downarrow)}$ and $\boldsymbol{v}_{d\uparrow(\downarrow)}$ denote the carrier densities and carrier velocity for spin-up and spin-down electrons. Therefore the charge current density can be written as:

$$\boldsymbol{j}_c = \boldsymbol{j}_{\uparrow} + \boldsymbol{j}_{\downarrow} \tag{3}$$

Besides the flow of charge, an electric current also carries a flow of angular momentum. However, the definition of spin current is not a simple as that of charge current, but in a simple and intuitive picture, spin current density can be defined as the product of the spin carried by a particle and their velocity, in analogy to the definition of charge current density given by the product of electron charge and their velocity. In this model, the transport of angular momentum is described by the spin current density $\boldsymbol{j}_s = \boldsymbol{j}_{s\uparrow} + \boldsymbol{j}_{s\downarrow}$ [48], where $\boldsymbol{j}_{s\uparrow} = \frac{\hbar}{2} n_{\uparrow}\boldsymbol{v}_{d\uparrow}$ and $\boldsymbol{j}_{s\downarrow} = -\frac{\hbar}{2} n_{\downarrow}\boldsymbol{v}_{d\downarrow}$, are the spin current densities for each spin species. Using the definition of the change current densities for each channel, we finally obtain that the spin current density can be written as:

$$\boldsymbol{j}_s = -\frac{\hbar}{2e}\left(\boldsymbol{j}_{\uparrow} - \boldsymbol{j}_{\downarrow}\right) \tag{4}$$

The spin current density is given in units of $A\hbar/em^2$, whereas the charge current density $\boldsymbol{j}_c$ and two carrier species densities $\boldsymbol{j}_{\uparrow}$ and $\boldsymbol{j}_{\downarrow}$ are given in units of A/m^2. From spin current density expression, equation 4, three possible current configurations can be identified as shown in figure 4. *Pure charge current*: when the two species of conduction electrons have the same population and are moving in the same direction, a flow of pure electrical charges is generated and no net angular momentum is transported, like depicted in figure 4(a). *Pure spin current*: if these two species of conduction electrons are moving in opposite directions, the net charge current density is zero and a flow of pure spin current density is created, see figure 4(c). *Spin-polarized current*: an unbalanced distribution of spin species gives rise to nonzero values for both charge and spin current density. An illustration of this can be seen in figure 4(b).

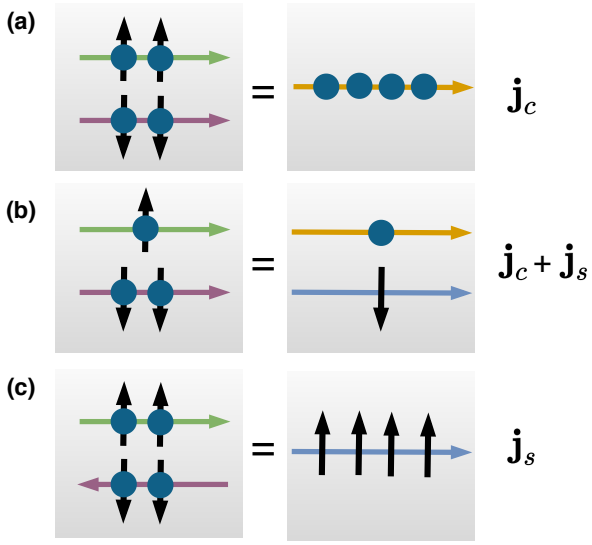

Figure 4. Illustration of different types of electric currents. **(a)** Pure charge current. **(b)** Spin polarized charge current and **(c)** Pure spin current.

Clearly, this definition of spin current density is still somewhat controversial and not sufficient to correctly describe the spin transport, since, among other reasons, the spin current density is not a conserved quantity. In contrast, charge current is a conserved quantity that can be described through its well-known continuity equation. The spin current decay, and consequently the quick loss of information being carried by the spins, is a serious problem for the realization of practical spintronic devices because the electron spin does not travel very far in most materials. This means that miniaturization and operation on a very short time-scales (less than one nanosecond) is required [49, 50]. However, at the nanoscale, considering spin current density as a conserved quantity, it is a very good approximation [46, 51].

Unlike charge currents, the transport of spin current can be realized using the coherent precession of magnetic moments, for which the classical magnetization is temporal and spatially dependent, called spin waves, and their quanta, called magnons, leading to magnonic spin currents. This spin transport mechanism is discussed in detail in the next subsection.

2.3 Spin-wave spin currents

Another mechanism that carries a spin current is the collective motion of magnetic moments, called spin waves (magnons) [52]. The concept of a spin wave was first predicted by Felix Bloch in 1930 [53] who described ferromagnetism in crystalline materials whose atoms are arranged in a periodic lattice. Spin waves can transport spin currents without any electronic displacement [30], this enables the generation and transport of spin currents in magnetic insulators. In order to describe spin-wave spin current in ferromagnetic materials, we begin with a phenomenological model for exchange interaction in many-electron systems known as Heisenberg model [54], which gives an intuitive picture of spin wave, described by Hamiltonian operator (also called the Heisenberg Hamiltonian) [55]:

$$\hat{\mathbf{H}} = -\sum_{\langle i,j \rangle} J_{ij} \hat{\mathbf{S}}_i \cdot \hat{\mathbf{S}}_j \tag{5}$$

where the sum is over all nearest neighbors, J_{ij} are the exchange coupling constants, also known as the exchange energy integral, and $\hat{\mathbf{S}}_{i(j)}$ is the Heisenberg spin operator at the $i(j)$-th site. This interaction is a direct consequence of the Pauli's exclusion principle and the Coulomb interaction, and depends on the overlap of the electron's wave function. For small interatomic distances, $J_{ij} < 0$ and antiparallel alignment of the electronic spins is preferred, then antiferromagnetic coupling occurs. With increasing distance, $J_{ij} > 0$ and ferromagnetic state becomes favorable, i.e., the energy is minimized when the spins are parallel to each other. Finally, for very large distances, the coupling vanishes and paramagnetism appears [56, 57].

Within the Heisenberg model, the classical ground state has all spins parallel. If one of the spins deviates from their ground state direction, the nearest-neighbor spins tend to deviate too, this perturbation propagates along the system mediated by the exchange interaction and the system starts a collective motion of phase-coherent precession around the equilibrium direction. These collective excitations of spins are the spin waves. In a simplified view, a spin wave can be regarded as a collective precession of the magnetization with a periodic spatial phase shift, wavelength λ and, inversely, wave vector $\boldsymbol{q} = (2\pi/\lambda)\boldsymbol{e_q}$, where $\boldsymbol{e_q}$ corresponds to the phase fronts propagation direction [58]. The dispersion relation can be obtained in a classical

analogy, which describes the spin wave energy as a function of wave vector. Spin waves are quantized, and the quanta of spin waves are called magnons. A magnon carries the angular momentum of $1\hbar$, which corresponds to a spin-flip in the crystal lattice. Magnons can be described as weakly interacting quasiparticles that obey Bose-Einstein statistics.

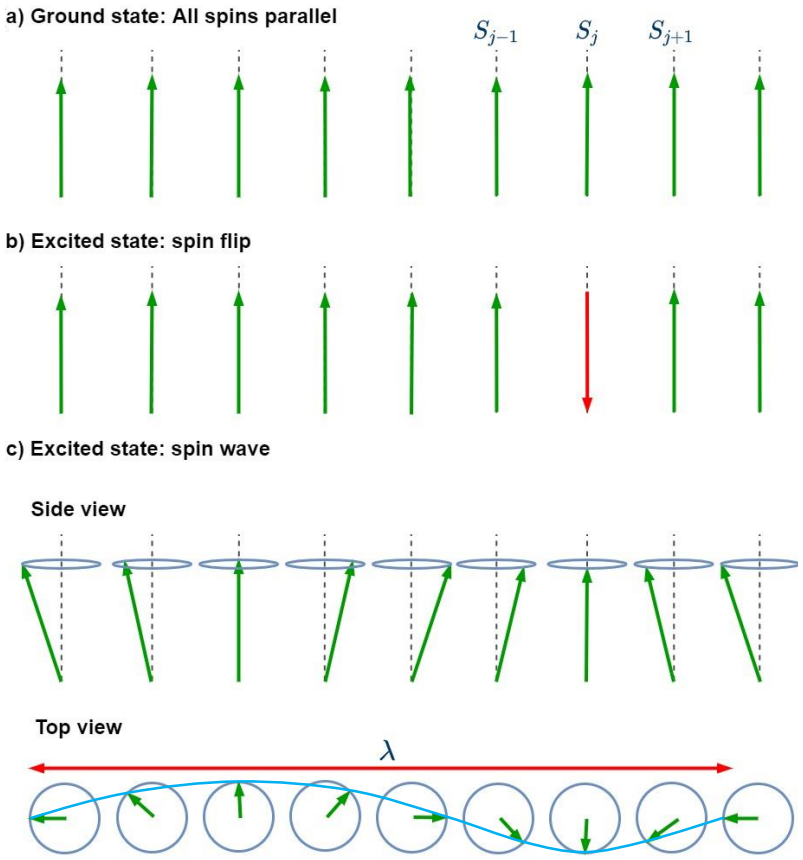

Figure 5. Sketch of a spin-wave in a one dimensional ferromagnetic chain. **(a)** In the ground state all spins are aligned. **(b)** Ferromagnetic chain in an excited state with one spin reversed **(c)** Spin wave mode: a periodic precession of the spins around their ordered direction. The distance between the two spins at the ends corresponds to one wavelength λ or analogous by a wavevector $\boldsymbol{q}$. The magnon is a delocalized spin-flip that can move along the chain.

In the following, we derive the spin wave dispersion relation from a semiclassical approach, for which we make the simplifying assumption that the spin interaction

is only between nearest-neighbors and $J_{ij} = J$ is constant. In a one dimensional approach, we consider N spin each of magnitude S on a line (as in figure 5(a)), so the hamiltonian in the equation 5 reduces to:

$$\hat{\mathbf{H}} = -2J \sum_i \hat{\mathbf{S}}_i \cdot \hat{\mathbf{S}}_{i+1} \tag{6}$$

Starting from the Heisenberg exchange Hamiltonian we use Eherenfest's theorem to write down the classical equations of motion for expected value of $\hat{\mathbf{S}}_j$, *ergo*:

$$\begin{aligned} \frac{d\langle \hat{\mathbf{S}}_j \rangle}{dt} &= \frac{1}{i\hbar} \langle [\hat{\mathbf{S}}_j, \hat{\mathbf{H}}] \rangle \\ &= \frac{2J}{\hbar} \langle \hat{\mathbf{S}}_j \times (\hat{\mathbf{S}}_{j-1} + \hat{\mathbf{S}}_{j+1}) \rangle \end{aligned} \tag{7}$$

In the ground state all spins are parallel, say along the z axis. If the spin is deviated slightly from z and we treat each spin as classical vector $\mathbf{S}_j = S_j^x \hat{\mathbf{x}} + S_j^y \hat{\mathbf{y}} + S_j^z \hat{\mathbf{z}}$, were $S_j^z = S$ and $S_j^x, S_j^y \ll S$. By neglecting higher order terms in S_j^x and S_j^y we can express equation 7 in linearized cartesian components:

$$\begin{aligned} \frac{dS_j^x}{dt} &= \frac{2JS}{\hbar}(2S_j^y - S_{j-1}^y - S_{j+1}^y) \\ \frac{dS_j^y}{dt} &= -\frac{2JS}{\hbar}(2S_j^x - S_{j-1}^x - S_{j+1}^x) \\ \frac{dS_j^z}{dt} &= 0 \end{aligned} \tag{8}$$

These equations admit solutions of the form $S_j^x = Ae^{i(qja-\omega t)}$, $S_j^y = Be^{i(qja-\omega t)}$ [55], where q is a wave vector and a is the interatomic spacing (lattice constant). Substituting these trial solutions in the above equations leads to $A = iB$ corresponding to circular precession of each spin about the z axis, and consequently:

$$\hbar\omega = 4JS(1 - cos(qa)) \tag{9}$$

The equation 9 represents the dependence of the spin wave frequency on the wave number and is called *dispersion relation*. In a semi-classical picture, we can interpret the spin wave as an excitation in which the precession phase varies linearly

from site-to-site as illustrated in figure 5(c). Spin waves with small wave numbers (*i.e.* $q \approx 0$) are especially interesting for many magnonic phenomena [59]. Through binomial expansion in the long-wavelength limit $qa \ll 1$ the dispersion relation becomes quadratic:

$$\hbar\omega = 2JSq^2a^2 \tag{10}$$

If an external static magnetic field is applied $\boldsymbol{H} = H\hat{\boldsymbol{z}}$, the dispersion relations given by equations 9 and 10 must be modified, adding a constant term that represents the Zeeman energy given by $\hbar\gamma\mu_0 H$, where γ is the gyromagnetic ratio. The revisited dispersion relation for low-wave number spin wave shows that the spin wave energy is determined only by the magnetic field intensity. Since the frequencies of spin waves with $qa \ll 1$ are in the microwave range, it is possible to excite the uniform precession mode with microwave radiation in a ferromagnetic resonance experiment, explained in detail in subsection 2.7

If we were to add together several closely spaced frequency components, we can form a $wave - packet$ that moves along the chain in the same manner as a particle. This particle is called *magnon* and represents the movement along the chain of a region where the probability of a flipped spin is high. The movement is enabled by the probability that spins will exchanged places with the nearest neighbor effectively moving the location of the flipped spin [60].

An individual magnon carries a spin $\hbar$ and energy $\epsilon_q = \hbar\omega_q$ [61]. Since magnons carry spin, net flow of magnons gives rise to a pure spin current.

2.4 Thermal excitation of magnons spin current

In equilibrium at finite temperature, magnons follow the Bose-Einstein statistic, and are naturally present by thermal excitation in magnetic materials. However, a net flow of spin angular momentum, that is, the magnon spin current, is not generated under thermal equilibrium conditions because magnons with wavenumbers $\boldsymbol{q}$ and $-\boldsymbol{q}$ exist in equal number [22].

In thermal equilibrium, and in the longwave limit, the total number of magnons excited at finite temperature T and quasi-momentum $\boldsymbol{q}$ is calculated by integrating the

magnon density of states over all frequencies after multiplying by the Bose-Einstein distribution function [55], thus the result can be written as:

$$N_{\boldsymbol{q}} = \int D(\omega) n^0_{\boldsymbol{q}}(\omega, T_m) d\omega \tag{11}$$

where $D(\omega)$ is the magnon density of states and $n^0_{\boldsymbol{q}}(\omega, T_m)$ is the Bose-Einstein distribution function, it gives the average number of magnons excited at temperature T in the mode $\boldsymbol{q}$ (see equation 12), with zero chemical potential because the energy and therefore magnon number is not conserved [62], this is because magnons can decay through magnon-phonon scattering events that transfer their angular momentum and energy to the crystal lattice. The occupation function is then just the Planck distribution function:

$$n^0_{\boldsymbol{q}}(\omega, T_m) = \frac{1}{e^{\hbar\omega_q / k_B T_m} - 1} \tag{12}$$

where $\hbar\omega_q$ is the magnon energy, k_B is the Boltzmann constant and T_m is the magnon temperature.

The magnon spin current is generated when there is an imbalance in the number of $\boldsymbol{q}$ and $-\boldsymbol{q}$ magnons due to the influence of some external perturbations [22]. In this context, magnon spin current can be generated electrically via electric magnon injection [63], optically [64] and thermally by establishing a thermal gradient in a ferromagnetic material (the so-called spin Seebeck effect explained later in the subsection 2.6). If a magnetic insulator is subject to a temperature gradient, the magnon density becomes position-dependent, such that the magnon density is non-uniform and magnons would diffuse from high to low-temperature region, leading to a diffusive magnon current. When the rate of creation of magnons is similar as the annihilation rate, the magnetization of the system is almost constat with time, then the system is in a quasi-equilibrium state in which the population of magnons and their density is constant but depends on the position. To parameterize the nonequilbrium magnon density, a magnon chemical potential $\mu_m(\boldsymbol{r})$ (or magnon spin accumulation) is introduced to the magnon Bose-Einstein distribution function, therefore the equation 12 becomes:

$$n_{\boldsymbol{q}}(\omega, \mu_m, T_m) = \frac{1}{e^{(\hbar\omega_q - \mu_m(\boldsymbol{r}))/k_B T(\boldsymbol{r})} - 1} \tag{13}$$

To find the total number of magnons we simply add up the effective number of magnon in excess of equilibrium in each momentum state, so the average magnons density is:

$$\begin{aligned}\delta n_m(\boldsymbol{r}) &= \sum_{\boldsymbol{q}} \frac{1}{V}\left[n_{\boldsymbol{q}}(\omega,\mu_m,T_m) - n^0_{\boldsymbol{q}}(\omega,T_m)\right] \\ &= \int \frac{d\boldsymbol{q}}{(2\pi)^3}\left[n_{\boldsymbol{q}}(\omega,\mu_m,T_m) - n^0_{\boldsymbol{q}}(\omega,T_m)\right]\end{aligned} \tag{14}$$

Similarly we find the spin current density by weighting the sum by the magnon group velocity $\boldsymbol{v_q}$ and the spin carried by a single magnon; $\hbar$:

$$\begin{aligned}\boldsymbol{j}_m(\boldsymbol{r}) &= \sum_{\boldsymbol{q}} \frac{\hbar}{V}\boldsymbol{v_q}\left[n_{\boldsymbol{q}}(\omega,\mu_m,T_m) - n^0_{\boldsymbol{q}}(\omega,T_m)\right] \\ &= \int \frac{\hbar d\boldsymbol{q}}{(2\pi)^3}\boldsymbol{v_q}\left[n_{\boldsymbol{q}}(\omega,\mu_m,T_m) - n^0_{\boldsymbol{q}}(\omega,T_m)\right]\end{aligned} \tag{15}$$

The distribution of the magnon number under the influence of a thermal gradient can be calculated with the Boltzmann transport equation under the relaxation time approximation [65, 66] in the stationary regime, as follows below:

$$\begin{aligned}n_{\boldsymbol{q}}(\omega,\mu_m,T_m) - n^0_{\boldsymbol{q}}(\omega,T_m) &= -\tau_{\boldsymbol{q}}\boldsymbol{v_q}\cdot\nabla n_{\boldsymbol{q}}(\omega,\mu_m,T_m) \\ &= -\tau_{\boldsymbol{q}}\boldsymbol{v_q}\cdot\left[\frac{\partial n^0_{\boldsymbol{q}}}{\partial T}\nabla T_m + \frac{\partial n^0_{\boldsymbol{q}}}{\partial \mu}\nabla\mu_m\right]\end{aligned} \tag{16}$$

here, $\tau_{\boldsymbol{q}}$ is the $\boldsymbol{q}$-magnon spin relaxation time, and characterizes the speed of recovery of the equilibrium state. Using equation 16 in equation 15, one obtains that the resultant total magnon spin current $(\boldsymbol{j}_m)$ has two contributions [67, 68, 69] driven by gradients in both magnon temperature $\left(\boldsymbol{j}_m^{\nabla T}\right)$ and chemical potential $\left(\boldsymbol{j}_m^{\nabla\mu_m}\right)$, *i.e.*:

$$\boldsymbol{j}_m = \boldsymbol{j}_m^{\nabla T} + \boldsymbol{j}_m^{\nabla\mu_m} \tag{17}$$

2.5 Spin-to-charge and, vice versa, conversion mechanism: Spin Hall effect and Inverse spin Hall effect

In a simple picture the spin Hall effect (SHE) describes the transversal spin current induced by a longitudinal charge current in a non-magnetic material as sketched in

figure 6(a). It was predicted by Dyakonov and Perel in 1971 [70], and experimentally observed for the first time by Kato *et al*. in 2004 [71].

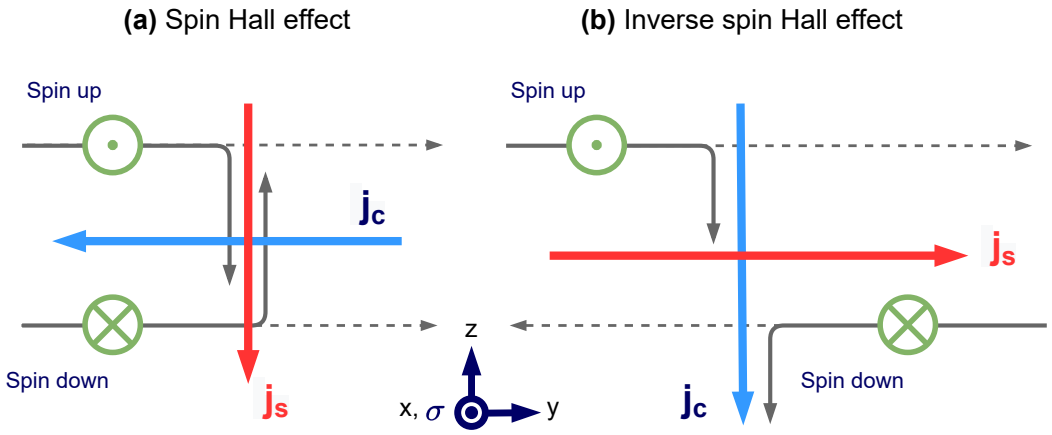

Figure 6. **(a)** A schematic illustration of the direct spin-Hall effect (SHE), a charge current $\boldsymbol{j_c}$ induces a transverse spin current $\boldsymbol{j_s}$ **(b)** A schematic illustration of the inverse spin-Hall effect (ISHE), spin down electrons are initially moving in the $-y$ direction, while spin up electrons are moving towards $+y$. Both spin species are deflected to the $-z$ direction, inducing a charge current $\boldsymbol{j_c}$. $\boldsymbol{\sigma}$ denotes the spin-polarization vector. The electrons accumulated on the sides of the conductor induces an electric field $\boldsymbol{E}_{ISHE}$ transverse to $\boldsymbol{j_s}$.

The SHE is a relativistic phenomenon due to spin-orbit coupling (SOC) between the electron spin and its orbital momentum, observed in the material through which the charge current flows.

In the rest frame of a moving electron, the electric field of a crystal lattice can be Lorentz transformed into an effective magnetic field. This effective magnetic field interacts with the spin of the electron and influences its moving direction [72], consequently, the electrons gain momentum in the transverse direction respect to their initial flow direction, originating a spin-dependent asymmetric scattering which leads to the spatial separation of electrons with opposite spin direction. For a non-magnetic material with an unpolarized charge current, the two different spin species are accumulated at the transversal edges of the sample and, therefore, a gradient in the spin-chemical potential emerges, giving rise to a pure spin current.

SOC can be illustrated drawing an analogy using the Magnus effect [73], where

a spinning ball in a fluid deviates from its straight path in a transverse direction that depends on the sense of rotation [74]. The inverse effect is named inverse spin Hall effect (ISHE) [75, 76], was observed for the first time in semiconductors during the 1970's [77] and 1980's [78] decades. In ISHE, a spin current is injected into a material with high SOC and due to the same reason mentioned above they get scattered perpendicular to their moving direction. As a result of their opposite spin and their opposite moving direction, all electrons get scattered into the same transverse direction, resulting in a pure charge current. The concept is schematically illustrated in figure 6(b). Both SHE and ISHE can be originated by intrinsic and extrinsic mechanism [79]. The extrinsic mechanism is caused on spin-dependent scattering of electrons by impurities. The intrinsic or Berry-phase mechanism is caused by the electronic band structure of the material, therefore exists even in absence of any impurity. Due to the Berry phase curvature [80], electrons gain an anomalous contribution to their velocity that is transverse to the applied electric field and thus gives rise to anomalous transport current [81].

Due to the same number of spin-up and spin-down electrons in a non-magnetic sample, the SHE does not induce an electric field [82] and spin currents cannot be detected by conventional electronic devices. In counterpart, the charge current established by ISHE, under open circuit conditions, generates an electric voltage which can be measured by conventional electronic methods.

In the SHE the charge current $\boldsymbol{J}_c$ (in units of A/m^2) induces an effective spin current $\boldsymbol{J}_s$ (in units of J/m^2) perpendicular to itself and the magnetization axis according to following equation [83]:

$$\boldsymbol{J}_s = \theta_{SH} \boldsymbol{J}_c \times \boldsymbol{\sigma} \tag{18}$$

On the other hand, the ISHE effect is therefore given by

$$\boldsymbol{J}_c = \theta_{SH} \boldsymbol{J}_s \times \boldsymbol{\sigma} \tag{19}$$

In the above equations $\boldsymbol{\sigma}$ is the spin polarization unit vector of $\boldsymbol{j}_s$ and denotes the direction of the spin polarization, e is the absolute value of electron charge and θ_{SH} is a phenomenological parameter named spin Hall angle which characterizes

the charge-to-spin current and vice versa conversion efficiency, determined by the ratio between the transverse spin Hall conductivity σ_{SH} and the longitudinal charge conductivity σ_c [84]

$$\theta_{SH} = \frac{\sigma_{SH}}{\sigma_c} \tag{20}$$

The strength of the SOC and thus the spin Hall angle is proportional to the proton atomic number to the fourth (Z^4) and is particularly large in for 4d and 5d transition metals (heavy metals) such as platinum (Pt) [75], tantalum (Ta) [85] or tungsten (W) [86], and alloys containing heavy metals such $CuBi$ [87] and $AuPt$ [88]. The reported values of θ_{SH} vary significantly, in particular for Pt values has been reported ranging from 0.0037 to 0.12 [89, 90]

2.6 Spin Seebeck effect

The generation, manipulation, and detection of spin currents play a critical role in the field of spintronics. The use of both, charge and spin currents is considered a promising avenue for future computing, communication and lost energy harvesting technologies. For the generation of pure spin currents there are several well-established methods, among them SHE, optical pumping [91], spin pumping effect [92] generated by the ferromagnetic resonance (FMR)[30, 93] and more recently the spin Seebeck effect (SSE).

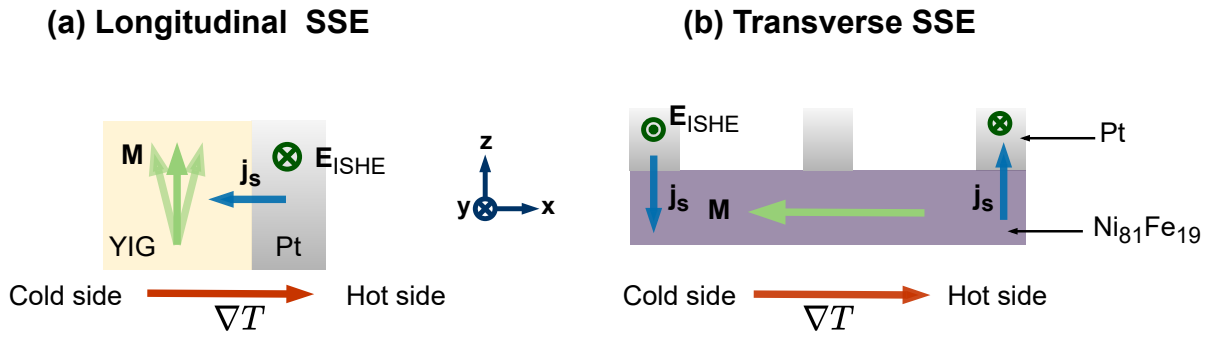

Figure 7. Schematic illustrations of spin Seebeck effect in the two configurations in which can be observed **(a)** longitudinal and **(b)** transverse configurations. $\boldsymbol{j}_s$ (blue arrow) is the spin current, $\boldsymbol{E}_{ISHE}$ (dark green arrow) is the inverse spin Hall effect electromotive force and $\boldsymbol{M}$ (light green) is the magnetization. In transverse, configuration the thermal gradient and the in-plane magnetic field are applied along the $x-$direction. In this configuration, the obtained voltage is observed along the Pt strip and changes continuously along the temperature gradient.

The SSE is a three-step process that enables the conversion of thermal energy into electrical energy [94]. The first step is the generation of a spin current, a flow of spin angular momentum as a result of a temperature gradient applied, in a magnetic material. Next, the thermally generated spin current is injected into an adjacent normal metal (NM) possessing strong spin-orbit coupling (typically Platinum) via the interfacial exchange interaction [95, 96]. Then, the electronic spin current is converted into a measurable transverse electric voltage by the inverse spin Hall effect [97, 20]. This phenomenon is the spintronic-version of the conventional Seebeck effect, a

typical thermoelectric phenomenon that directly converts the temperature gradient in conductors to electric field [98], found by Thomas Seebeck almost 200 years before [99]. The SSE was first reported by Uchida *et al*. in 2008 [100] in the system composed by the soft ferromagnetic metal $Ni_{81}Fe_{19}$ film with a thin platinum (Pt) strip. In 2010, the SSE was also observed in the ferromagnetic semiconductor $GaMnAs$ [101] and magnetic insulators (MI) [102, 103].

The SSE can be observed in two different configurations [20], depending on the direction of the spin current with respect to the direction of the thermal gradient: one is the transverse configuration (see figure 12(b)), so-called transverse SSE (TSSE), in which the spin current is transverse to the in-plane applied temperature gradient. In this configuration, the measured voltage changes sign from the hot and cold side, and vanishes in the middle of the sample. The other configuration occurs when the spin current flows parallel to the out-of-plane applied temperature gradient, this configuration (see figure 7(a)) is called longitudinal SSE (LSSE).

The TSSE is not without controversies. For instance, a temperature gradient out-of-plane can be originated while applying a thermal gradient in the plane, then other thermomagnetic effects are expected, such as planar and anomalous Nernst effects (ANE) [104] and LSSE [105].

Today, the most common setup for SSE research is the longitudinal configuration in magnetic insulators/normal metal bilayer (MI/NM) since the signal from spurious effects, such as short circuit current and anomalous Nernst effect (ANE), which have the same magnetic field dependence as SSE, in conductive ferromagnetic material are suppressed [103, 106, 107].

In this context, since the first observation of SSE in the ferrimagnetic insulator yttrium iron garnet $Y_3Fe_5O_{12}$, this material has become particularly interesting to study spin transport, due to their unique magnetic properties such as low Gilbert damping, long magnon spin diffusion length ($\lambda_{sd} \approx 10\ \mu m$ [32]), high resistivity and high Curie temperature. The magnon spin diffusion length is the distance over which a spin current can propagate without losing its polarization, and can be described as follows:

$$\lambda_{sd} = \sqrt{D\tau} \tag{21}$$

where D is the magnon diffusion constant and τ is the magnon spin relaxation time.

2.6.1 Theory of LSSE in magnetic insulators

The origin of SSE can be found in the spin pumping from thermally excited magnons caused by an interfacial temperature difference between magnons in the FM layer and the electrons in the NM layer, such that the spin current density pumped into the NM is $j_s = L_s(T_m - T_e)$, where T_m is the temperature of magnons, T_e is the temperature of electrons and L_s is the interfacial spin Seebeck coefficient. This theoretical explanation was given by Xiao *et al*. in 2010 [108], based on the physics of magnon-phonon interaction in magnetic insulators, first investigated by Sanders and Walton in 1977 [109].

In this theoretical framework the magnon and phonons in the FM layer are considered as two weakly interacting subsystems, each with their own temperature. On the other hand, the electron-phonon interaction is sufficiently strong, such that the temperature of phonons and electrons subsystems in the NM layer are the same.

The magnetization in the FM is represented by a single domain and can be regarded as a macrospin $\boldsymbol{M} = M_s V \boldsymbol{m}$, where M_s is the saturation magnetization, V is the total volume of the FM and $\boldsymbol{m} = \boldsymbol{M}/|\boldsymbol{M}|$ is the unit vector parallel to magnetization.

At non-zero temperature, the magnetization $\boldsymbol{M}$ in FM layer is thermally activated and therefore $d\boldsymbol{M}/dt \neq 0$. This leads to a spin pumping driven spin current ($\boldsymbol{J}_{s,pump}$), proportional to the magnon temperature T_m, into the NM which is given by equation 22 [92]. This is accompanied by a back flow spin current $\boldsymbol{J}_{s,back}$ given by equation 23 [110, 83], caused by a random torque on the magnetization in FM layer, originated by thermal noise in electron spins in NM layer. $\boldsymbol{J}_{s,back}$ is called Johnson-Niquist spin current [106] noise and is proportional to T_e.

$$\boldsymbol{J}_{s,pump}(t) = \frac{\hbar}{4\pi}\left(g_r^{\uparrow\downarrow}\boldsymbol{m}(t) \times \frac{d\boldsymbol{m}(t)}{dt} - g_i^{\uparrow\downarrow}\frac{d\boldsymbol{m}(t)}{dt}\right) \tag{22}$$

$$\boldsymbol{J}_{s,back}(t) = -\frac{M_s V}{\gamma}\gamma\boldsymbol{m}(t) \times \boldsymbol{h}_r(t) \tag{23}$$

In equation 22, $g_r^{\uparrow\downarrow}$ and $g_i^{\uparrow\downarrow}$ are the real and imaginary part of the dimensionless spin mixing conductance [111], $G^{\uparrow\downarrow} = g_r^{\uparrow\downarrow} + i g_i^{\uparrow\downarrow}$, at the FM/NM interface.

Spin mixing conductance is a key quantity introduced by the scattering theory that describes the efficiency of the transfer of spin angular momentum per unit area through an FM/NM interface; a higher spin-mixing conductance means that more spin angular momentum can be transferred from the NM layer into the magnetic layer and viceversa. It is defined in terms of the spin-dependent transmission and reflection matrices [112, 113]. $g_r^{\uparrow\downarrow}$ is associated with the "in-plane" or "Slonczewski" torque along the in-plane direction and is perpendicular to $\boldsymbol{M}$. $g_i^{\uparrow\downarrow}$ describes an exchange magnetic field acting on the magnetization, which results in spins being pumped in the direction of the precessional motion, and it is usually an order of magnitude smaller than $g_r^{\uparrow\downarrow}$ so it can be neglected [114]. In equation 23, γ is the gyromagnetic ratio and $\boldsymbol{h}_r(t)$ is a random magnetic field from various sources such as thermal or contact noise. Therefore, the net thermal spin current across the FM/NM interface is given by:

$$\boldsymbol{J}_s(t) = \boldsymbol{J}_{s,pump}(t) + \boldsymbol{J}_{s,back}(t) \tag{24}$$

The ensemble average of $\boldsymbol{J}_s(t)$ provide the dc spin current density along the magnetization equilibrium direction, i.e.[115]:

$$J_s = \langle \boldsymbol{J}_s(t) \rangle \approx \frac{\gamma \hbar g^{\uparrow\downarrow} k_B}{2\pi M_s V_a} (T_m - T_e) \tag{25}$$

where k_B is the Boltzmann constant, V_a is the magnetic coherence volume. At room temperature the magnetic coherence volume in YIG is about $V_a \approx 2.2\ (nm)^3$. $g^{\uparrow\downarrow}$ is the real part of the spin mixing conductance per unit area at the interface and per conductance quantum $e^2/\hbar$.

Equation 25 indicates that in thermal equilibrium state (i.e. $T_m = T_e$) no net spin current is generated across the MI/NM interface, this means that the pumped spin current is canceled out by the spin-current noise. On the other hand, out of thermal equilibrium a finite net spin current flows through the MI/NM interface. These cases are illustrated in figures 8(a), 8(b) and 8(c).

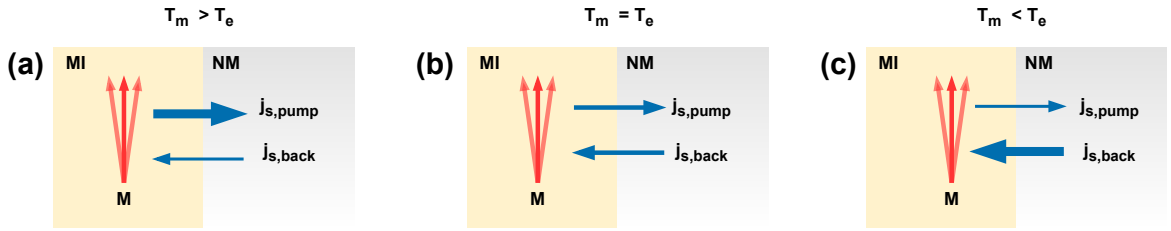

Figure 8. Spin current generation by SSE. Under the application of a thermal gradient, magnetization dynamics get thermally activated pumping a spin current into the NM. Additionally, a backflow spin current is induced by thermal noise of the electrons in the NM **(a)** $T_m > T_e$ **(b)** $T_m = T_e$ thermal equilibrium **(c)** $T_m > T_e$.

2.7 Ferromagnetic resonance (FMR) and two-magnon scattering relaxation process in thin films

Ferromagnetic resonance (FMR) is one of the basic experimental methods to study magnetization dynamics in ferromagnetic materials.

Conventionally, FMR is modeled in terms of the Landau-Lifshitz-Gilbert (LLG) equation [116, 117], given by equation 26. In the following, we will only consider the case when the magnetic field is applied in the plane of the sample. When a static external magnetic field $\boldsymbol{H}$ is applied to a ferromagnet, it causes the magnetization to align itself to the field direction. If a weak, time-dependent microwave field $\boldsymbol{h}(t)$ is applied in addition, the perpendicular components to the magnetization will exert a torque that can cause magnetization precession, so that the energy of the microwave field is absorbed. When the frequency of microwave field coincides with the precessional frequency, the energy is strongly absorbed by the magnetic system from the microwave field $\boldsymbol{h}(t)$, resulting in magnetization precession in a uniform mode, i.e. with all the spin precessing in-phase. This phenomenon is known as ferromagnetic resonance (FMR).

In a real ferromagnetic system, dissipative interactions should be considered, therefore the motion of the magnetization around its equilibrium position is described by the LLG equation of motion:

$$\frac{d\boldsymbol{M}}{dt} = -\gamma \boldsymbol{M} \times \boldsymbol{H}_e + \frac{\alpha}{M_s}\left(\boldsymbol{M} \times \frac{d\boldsymbol{M}}{dt}\right) \tag{26}$$

where $\boldsymbol{H}_e$ is the effective magnetic field, which is given by the superposition of an externally applied magnetic field ($\boldsymbol{H}_{ext}$), that includes both the dc magnetic field and the microwave magnetic field, and the internal magnetic field ($\boldsymbol{H}_{int}$), composed by the demagnetizing field and the magnetocrystalline anisotropy field. $\boldsymbol{H}_e$ is given by equation 27. M_s is the saturation magnetization of the sample, γ is the electron gyromagnetic ratio and α is a dimensionless damping parameter, known as the Gilbert damping parameter. The first term on the right-hand side of equation 26 describes the precession of the magnetization around the effective magnetic field. In the absence of damping, this leads to the Larmor precession with frequency $\omega = \gamma H_e$, known as the Larmor frequency for an infinite and isotropic ferromagnet. The second term on the right-hand side of equation 26 describes a viscous-like damping, proportional to the rate of changing of the $\boldsymbol{M}$, that drives the magnetization to spiral towards the applied magnetic field direction as shown in figure 9. LLG equation is a macro-spin approach since the magnetization dynamics in the ferromagnet is described only by the dynamics of the total magnetization and the dissipation leads only to the damping of the precession cone angle, while the magnitude of $\boldsymbol{M}$ remains constant.

$$\boldsymbol{H}_e = \boldsymbol{H}_{int} + \underbrace{\boldsymbol{H}_{dc} + \boldsymbol{h}(t)}_{\text{External magnetic field}} \tag{27}$$

In this work, we are interested in describing the magnetization dynamics in thin films and mainly, obtain the eigenfrequency of the magnetization precession.

For this purpose, let's consider a thin film without anisotropies except for demagnetization effects caused by the creation of "magnetic charges" on the surface of a ferromagnet caused by uncompensated magnetic moments. This leads to the so called demagnetizing field that reduces the internal effective magnetic field. The external magnetic field is composed by a static part lying in the x-direction and a transverse dynamic magnetic field along the y-direction, therefore, the magnetization of the sample will also be composed of static and dynamic parts.

$$\boldsymbol{H}_{ext} = H_0\hat{x} + h_y(t)\hat{y} \tag{28}$$

$$\boldsymbol{M} = M_x\hat{x} + m_y(t)\hat{y} + m_z(t)\hat{z} \tag{29}$$

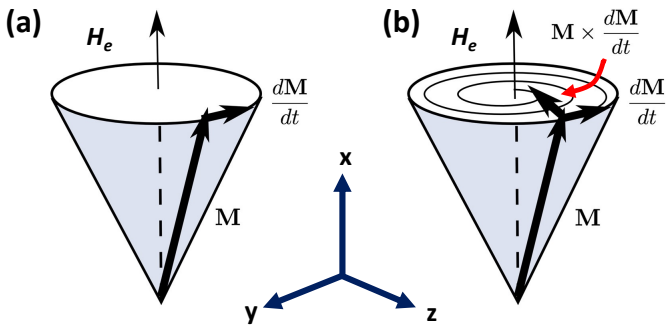

Figure 9. Schematic illustration of the precession of the magnetization vector around the effective field. **(a)** without damping, the magnetisation $\boldsymbol{M}$ precesses along the applied field on a constant orbit due to the precession torque $-\gamma \boldsymbol{M} \times \boldsymbol{H}_e$. **(b)** With damping, the Gilbert damping is responsible for the relaxation of magnetisation towards the equilibrium state, due to which the magnetisation follows a helical trajectory around $\boldsymbol{H}_e$. Image adapted from reference [118].

Since the thickness of the film is much smaller than the lateral sizes, only the out-of-plane demagnetization field must be taken into account.

$$\boldsymbol{H}_d = -N_y m_y(t)\hat{y} \tag{30}$$

where N_y is the out-of-plane demagnetizing factor equal to 4π for a plane infinite ellipsoid, which is a good approximation for a thin film. Then, the effective magnetic field within the sample reads:

$$\boldsymbol{H}_e = H_0\hat{x} + \left(h_y(t) - 4\pi m_y(t)\right)\hat{y} \tag{31}$$

In order to solve the LLG equation we assume harmonic time dependencies of dynamic parts of $\boldsymbol{H}_{ext}$ and $\boldsymbol{M}$, that is:

$$m_{y,z}(t) = m_{y,z}e^{i\omega t} \tag{32}$$

$$h_y(t) = h_y e^{i\omega t} \tag{33}$$

where $\omega = 2\pi f$ is the angular frequency of $\boldsymbol{h}(t)$. For small angle precession, the LLG equation can be linearized in vicinity of the equilibrium direction, where we

can do the following approximations $M_x = M_s$ and $\frac{dM_x}{dt} = 0$. By substituting the equations 29 y 31 into LLG equation 26 and approximating to first order, we obtain the following system of coupled equations:

$$i\omega m_y = -\gamma H_0 m_z - \alpha i\omega m_z \tag{34}$$

$$i\omega m_z = -\gamma M_s h_y + \gamma \left(H_0 + 4\pi M_s\right) m_y + \alpha i\omega m_y \tag{35}$$

The resonant frequency ω_r for a given applied magnetic field can be found setting $\alpha = 0$ and $h_y = 0$, i.e. free and nondamped oscillations, that give rise to eigenoscillations and the eigenfrequency of the precession [61], and solving the system of coupled equations 34 and 35 for ω, yielding the famous Kittel's equation [119] for FMR in the special case of a thin film that is magnetized in-plane:

$$\omega_r = \gamma \sqrt{H_0(H_0 + 4\pi M_s)} \tag{36}$$

In order to describe a more realistic system, it is customary to replace the saturation magnetization in equation 36 by the revisited Kittel equation given by equation 37, in which the saturation magnetization $4\pi M_s$ is replaced by the so-called effective magnetization field $4\pi M_{eff} = 4\pi M_s - H_{ani}$ and H_{ani} is the effective out-of-plane uniaxial anisotropy field that can be described by equation 38. The origin of H_{ani} is associated with the magneto-crystalline anisotropy present in the (111)-oriented YIG film.

$$\omega_r = \gamma \sqrt{H_0(H_0 + 4\pi M_{eff})} \tag{37}$$

$$H_{ani} = \frac{2|K_1|}{M_s} + \frac{4|K_2|}{M_s} \tag{38}$$

In the above equation $K_1 = -6100\, erg/cm^3$ and $K_2 = -260\, erg/cm^3$ are the first and second order cubic anisotropy constants [120], for YIG crystals, respectively and M_s refers to the saturation magnetization.

The resonant frequency depends on both frequency and magnetic field, so both parameters must be swept in FMR experiments. In a broadband FMR experiment, a microwave source is connected to a coplanar waveguide (CPW) using coaxial

cables and microwave probes. The FM sample is placed on the CPW. The microwave frequency is held constant and the magnetic field is swept determining the resonance field H_{res}. At resonance, the sample will absorb energy from the CPW. The output signal at the CPW travels toward a detector diode (Schottky diode) and is converted to an electric signal. This signal is measured by monitoring the microwave losses in the sample as a function of the applied magnetic field. The measurement is then repeated for a range of frequencies to obtain the resonance frequency as a function of the magnetic field. In order to improve the signal-to-noise ratio (SNR), we use a lock-in detection technique, where the applied magnetic field is weakly modulated at low frequencies $\omega_{mod} = 2\pi f_{mod}$ (with f_{mod} in the range of 100 to 200 Hz) and a lock-in amplifier is used to detect and amplify the corresponding AC component of the diode voltage.

If we consider the power absorbed as a function of magnetic field as $\mathbf{P}(H_0 + \delta H)$, where H_0 is the static magnetic field and $\delta H = he^{i\omega_{mod}t}$ is the modulated component, the small modulation of the magnetic field implies that the power absorbed by the sample oscillates as well. As shown in equation 39, the power absorbed can be expanded around the static magnetic field H_0 by using Taylor series. By ignoring the higher-order terms, we obtain that the output signal is proportional to the first derivative of the absorbed power and the FMR resonant curve is similar to figure 10.

$$\mathbf{P}(H_0 + \delta H) \approx \mathbf{P}(H_0) + \frac{\partial \mathbf{P}(H_0 + \delta H)}{\partial H}\bigg|_{H_0} \delta H + O(2f_{mod}) \tag{39}$$

In the above equation, the first term is a f_{mod}-independent term, which is removed by the lock-in amplifier.

Figure 10(a) illustrates the employed experimental setup. This is prototypical for a broadband FMR measurement setup with CPW mounted between the poles of an electromagnet, that provides the static magnetic field H_0, and modulation Helmholtz coils. The sample is placed with the ferromagnetic layer facing the center conductor of the CPW. Radio-frequency currents were injected into the coplanar waveguide and induced an inhomogeneous microwave magnetic field h_{rf}, which oscillates in the sample plane perpendicularly to H_0.

From the FMR spectrum it is possible to extract two important parameters: the

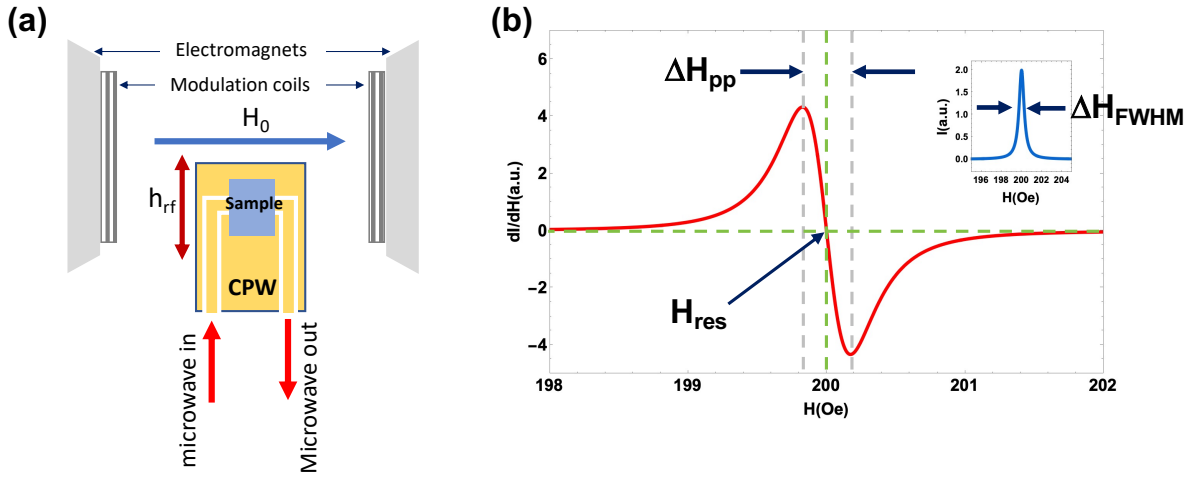

Figure 10. **(a)** Schematic of the broadband FMR setup. The coplanar waveguide (CPW) is mounted between the poles of an electromagnet and modulation coils. Ferromagnetic resonance in the sample is excited using a microwave current flowing through the CPW. H_0 denotes the applied static magnetic field and h_{rf} is rf-magnetic field. **(b)** Schematic measurement spectra. First derivative FMR spectrum with definition of some of its parameters; resonance field and peak-to-peak linewidth. The inset shows the corresponding FMR absorption spectrum with the definition of FWHM linewidth.

resonance line position and the full width at half maximum (FWHM) of the resonance peak linewidth ΔH_{FWHM}. The linewidth contains information about various magnetic loss mechanisms. Two factors determine the losses [121]; the material properties, so-called intrinsic mechanism, and the imperfections of the material, so-called extrinsic mechanisms. The intrinsic damping mechanism is linearly proportional to the microwave frequency and can be accounted by the Gilbert damping parameter α. It is mainly caused by scattering of spin waves with electrons and phonons. Whereas the extrinsic damping contribution comes from magnetic inhomogeneities or defects within the magnetic sample that can locally modify the internal magnetic field [122]. The extrinsic factor is frequency independent and approaches zero for a sample free of defects. These both contributions to the linewidth are summarised by the following empirical expression [123]:

$$\Delta H_{FWHM} = \Delta H_0 + \frac{4\pi\alpha f}{\gamma} \tag{40}$$

where ΔH_0 is an offset constant due to extrinsic mechanisms, known as inhomogeneous broadening, coming from long range magnetic inhomogeneities within the magnetic material [124], which produce localized variations in the resonance field, but that in sum contribute to the broadening of the linewidth independently of the frequency. The second term in the right-hand side of equation 40 is the intrinsic contribution to the linewidth and it is proportional to the frequency with a slope determined by α. The peak-to-peak linewidth ΔH_{pp} is related to the ΔH_{FWHM} by [125]:

$$\Delta H_{FWHM} = \frac{\sqrt{3}}{2}\Delta H_{PP} \tag{41}$$

Figure 10(b) shows a representative FMR linewidth ΔH_{PP} and ΔH_{FWHM}.

In addition to the inhomogeneous line broadening ΔH_0, inhomogeneities can also give rise to a non-Gilbert-type damping [126], in which the energy is redistributed within a magnetic system, through a process in which only two magnons are involved, i.e. one magnon is destroyed and another, with the same energy, is created [127].

Defects or inhomogeneities in the crystal, to name a few, grain boundaries, lattice strains due to the substrate imperfections in thin films, material surface defects, and magnetic roughness of the NM/FM interface [128], act as scattering centres. The interaction of magnons with inhomogeneities leads to the redistribution of magnon populations over the spin-wave spectrum. When a magnon with zero wave vector, $q = 0$, and frequency ω scatters by an inhomogeneity, it is transformed into another magnon with the same frequency, following the conservation of energy, but with different wavevector $\boldsymbol{q} \neq 0$, since, around the defects, the space translational symmetry is broken, which allows scattering processes where the momentum is not conserved [129, 130]. In order to reach equilibrium, the magnetic energy has to be transfered directly to the lattice system therefore the magnetization precession undergoes rapid relaxation [61]. This mechanism is so-called two-magnon scattering [131] (TMS) process an it is illustrated in figure 11. It is an extrinsic spin damping mechanism and contributes to the FMR linewidth. For a homogeneously in-plane magnetized thin film, TMS- peak-to-peak linewidth contribution can be approximately expressed as [132, 133, 134]:

$$\Delta H_{TMS,PP} = \frac{2}{\sqrt{3}}\Gamma_0 \, sin^{-1}\left[\frac{\left[f^2 + (f_0/2)^2\right]^{1/2} - f_0/2}{\left[f^2 + (f_0/2)^2\right]^{1/2} + f_0/2}\right]^{1/2} \tag{42}$$

where $f_0 = (\gamma/2\pi)4\pi M_{eff}$, and M_{eff} is the effective magnetization. The coefficient Γ_0 represents the strength of the TMS contribution to the linewidth, this term is given by a complex function of average distribution of crystalline defects (which are assumed to have rectangular shape) and the exchange stiffness of the ferromagnetic material. When the orientation of the applied field (and the magnetization) is in plane, the TMS strength coefficient can be considered constant [132]. This parameter is fitted to the experimental data. The expression given by equation 42 shows a nonlinear frequency dependence which distinguishes the TMS contribution from other Gilbert like damping contributions.

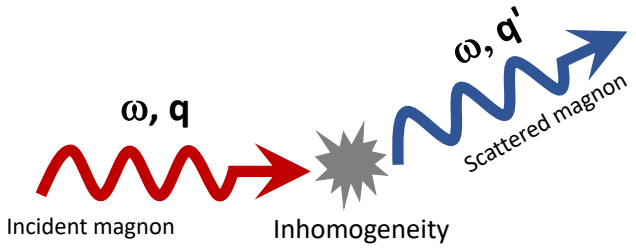

Figure 11. Diagramatic representation of the two magnon scattering. One magnon with zero wavevector ($\boldsymbol{q} \approx 0$) is scattered by a inhomogeneity into another magnon with the same energy or frequency ω but with a different wavevector.

Combining equations 40 and 41 and including the extrinsic contribution given by 42, the measured frequency linewidth is therefore often expressed in the more complete form as follows:

$$\Delta H_{PP} = \Delta H_{0,PP} + \frac{8\pi\alpha f}{\sqrt{3}\gamma} + \Delta H_{TMS,PP} \tag{43}$$

Since the extrinsic mechanism of magnon relaxation, like TMS processes, implies an additional pathway for magnetic damping, this is generally undesirable in magnonic devices. However, since such contributions are subject to control through sample preparation and via the application of electric field [135], their identification

and understanding is of great technological importance. For example, it is possible to suppress the ringing effect of magnetization after precessional reversal in certain devices like magnetoresistive random access memory (MRAM)[136].

Chapter 3
Materials, fabrication & characterization methods

This third chapter presents an overview of the main materials used in this work and describes the methods and processes used in their fabrication. X-ray reflectivity and diffraction as well as ferromagnetic resonance measurements were performed to characterize the structural and magnetic properties of the films. The film thickness and density were evaluated by X-ray reflectometry. All characterizations were performed at room temperature. The analysis of magnetic properties reveals clear evidence for a nonlinear frequency dependence of the linewidth, attributable to the existence of an extrinsic contribution to the magnetization relaxation process, termed two magnon scattering (TMS). Such scattering process must be considered even in high quality samples [137]. The structural characterization shows high crystalline quality, epitaxial growth and slightly strained interface. From which we can elucidate that TMS could be originated by the existence of structural discontinuities and strain at the interface.

3.1 Yttrium iron garnet

Yttrium Iron Garnet ($Y_3Fe_5O_{12}$, YIG for short) is a synthetic ferrimagnetic insulator Garnet (similar to the semiprecious stone and does not occur naturally on earth) that was discovered by Bertaut and Forrat in 1956 [138]. YIG suites many microwave applications as: circulators, isolators and phase shifter devices for telecommunication applications, and magneto-optical devices for storage and information processing such as: displays, deflectors, optical insulators, read heads, integrated magneto-optical devices [139] and magneto-optical transparencies or spatial-time light modulator, which is a two-dimensional optical device that allows to manipulate light by modulating amplitude, phase and polarization of incident light [140]. Yttrium iron garnet has a complicated cubic crystal structure with eight chemical formula units and three sublattices, thereby, contains 24 Y^{3+} ions, 40 Fe^{3+} ions and 96 O^{2-} ions.

YIG has a large unit cell with lattice parameter at room temperature $a_{YIG} = 12.376$ Å, and it belongs to the space group $Ia\bar{3}d$. Figure 12(a) shows a schematic representation of the YIG's unit cell.

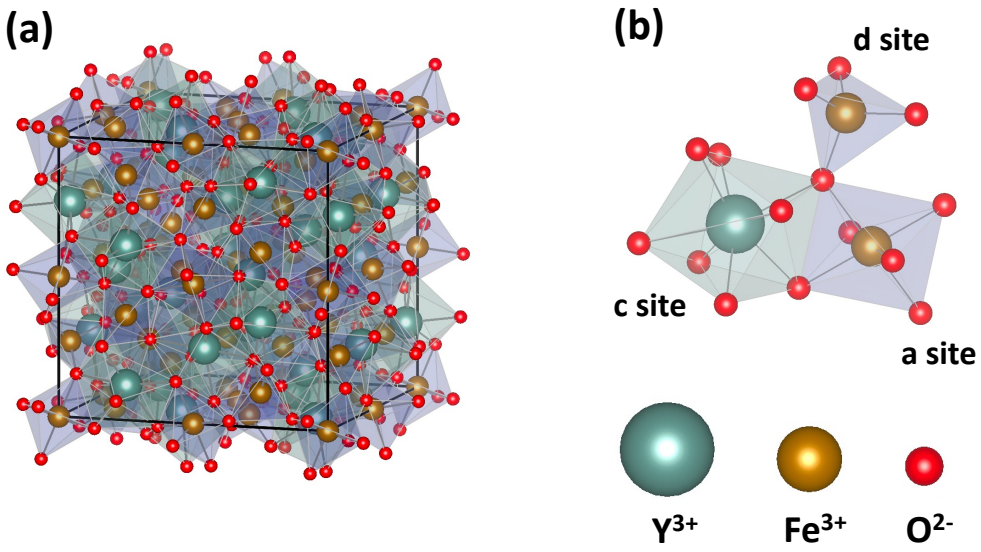

Figure 12. Schematic diagram of the YIG crystal structure. **(a)** Unit cell of YIG [141] **(b)** Part of the unit cell with different sites of cations. Crystal structure model rendered using VESTA [142].

The YIG structure has three crystallographic sites formed of oxygen polyhedra, surrounding the cations. The nonmagnetic (or weak diamagnetic) Y^{3+} ions occupy 24 sites, and are surrounded by eight oxygen ions in a distorted dodecahedral coordination environment, called c-site. The 40 Fe^{3+} are divided between 24 tetrahedral sites, called d-site, and surrounded by four O^{2-} ions, and 16 octahedral sites, called a-site, surrounded by six O^{2-} ions [143]. The ions at the a and d sites have opposite orientation of their spins and consequently collinear and antiferromagnetically coupled via the superexchange interaction mediated by the O^{2-} anions. For each formula unit there are two Fe^{3+} on the octahedral a site, which contribute with $10\mu_B$, and three Fe^{3+} on the tetrahedral d site, which contribute with $15\mu_B$ in the opposite direction, giving rise to a ferrimagnetic state with $5\mu_B$ magnetization at 0 K [144, 145].

Since its discovery, the YIG has become a key material for magnon spintronics due

to its unique magnetic properties [146]: exceptionally low magnetic damping (Gilbert damping, $\alpha \approx 10^{-5}$ [147, 35]), allowing spin-wave propagation to be observed over centimetre distances. YIG is a very good electrical insulator whose band gap is $\approx 2{,}7\ eV$ and consequently exhibits a very high resistivity ($\sim 10^{-12}\ \Omega m$) [30], preventing a possible overlap with other thermoelectric effects or spurious electrical signals. It has a relatively high Curie temperature ($\sim 570\ K$) [148], which allows its applications at room temperature.

YIG films can be grown by a wide range of techniques, such as liquid phase epitaxy (LPE) [149], pulsed laser deposition (PLD) [150] or sputtering [151]. The samples used in this thesis were prepared by PLD on top of paramagnetic insulator single-crystal (111) gadolinium gallium garnet ($Gd_3Ga_5O_{12}$, GGG), due to its excellent lattice-matching with the YIG lattice constant [152, 153], thereby reducing strain and dislocation during the growth of YIG. Thus achieving a film with good crystalline properties.

3.1.1 YIG thin film growth by pulsed laser deposition

Pulsed laser deposition (PLD) is a physical vapor deposition technique using high-energy laser pulses to vaporize the surface of a solid target placed inside a vacuum chamber, under a controlled O_2 atmosphere and temperature. Each laser pulse vaporizes or ablates instantaneously a small volume of material creating a plasma plume. The ablated material from the plume is then allowed to recondense on a substrate, where the film growth occurs [154]. A typical setup for PLD is schematically shown in Figure 13. PLD is one of the most versatile techniques in solid-state physics to deposit stoichiometrically high-quality thin films and multilayers, with fine control on film thickness as well as composition and epitaxial growth characteristics [155].

Epitaxial YIG films were grown by PLD (Surface Tech, Hückelhoven, Germany) from a stochiometric polycrystalline yttrium iron garnet target by using an excimer laser (COMPex 102, KrF gas, wavelength of 248 nm, Lambda Physik, Göttingen, Germany) at $1 - 10\ Hz$ pulse repetition rate, laser fluence of $1.1 - 4.0\ J/cm^2$, and base pressure of $1.4 \times 10^{-3}\ mTorr$. In order to ensure good thermal contact, the GGG substrate was stuck to the sample holder with a silver paste. Before starting the growth, and in order to clean the GGG substrate surface, the substrate was heated at

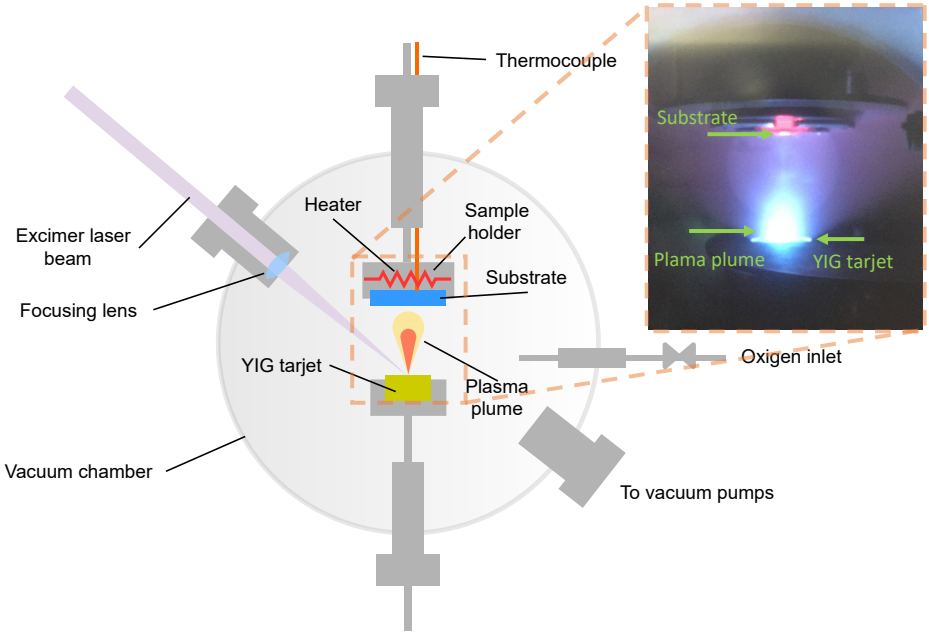

Figure 13. Simplified schematic of a pulsed laser deposition setup. The inset shows a photograph of the laser-induced plasma plume during deposition.

$700 - 800\ ^{\circ}C$ under 10 $mTorr$ of oxygen partial pressure during 30 minutes, allowing the oxidation and elimination of any organic contaminant. After this time, the growth of the film begins, the oxygen partial pressure (PO_2) was set up at 1.5 $mTorr$ (samples YIG 38, YIG 42 and YIG 47) and 20 $mTorr$ (samples YIG 7, YIG 8 and YIG 19), the substrate temperature during film deposition was kept constant to $700 - 800\ ^{\circ}C$ and monitored by a thermocouple. To obtain the desired film thickness, the number of laser pulses varied between 660 to 6000. After growth, films were cooled down to room temperature by switching off the heater of the sample holder, while keeping the same oxygen pressure used for the growth. The growth parameters and the resulting film thickness are listed in table 1. These conditions were selected, after exploring a wide range of values of oxygen pressure and fluences, to test sample structural variations and this effect on the spin dynamics.

Table 1. Main control parameters for pulsed laser deposition for some samples

Sample	Substrate	Temperature	PO_2	Laser Fluence	Laser pulses	Pulse repetition rate
		°C	mTorr	J/cm^2		Hz
YIG 7	GGG(111)	700	20	1.1	1000	1
YIG 8	GGG(111)	700	20	1.1	4000	1
YIG 19	GGG(111)	800	20	1.1	6000	5
YIG 38	GGG(111)	750	1.5	4.0	660	2
YIG 42	GGG(111)	750	1.5	4.0	1000	2
YIG 47	GGG(111)	750	1.5	4.0	720	2

3.2 Platinum

The most widely used electrical method to detect a spin current is the inverse spin Hall effect, which appears in heavy metals like platinum (Pt), Tantalum (Ta), Gold (Au) and Tungsten (W). Platinum metal has been widely employed for this essential role of detecting (and generating) a pure spin current, and Pt thin films on ferromagnet has become indispensable for establishing virtually all the discovered pure spin current phenomena. A large spin Hall angle is therefore beneficial to the SSE experiments. [156].

The magnitude of spin Hall angle depends on the strength of SOC and is proportional to Z^4, where Z is the atomic number, so usually heavy metals (HM) with large Z have a relative large spin Hall angle. Platinum exhibits a θ_{SH} ranging from 0.0067 to 0.33 [157] or even larger, which is considerably larger than the spin Hall angle found in most other metals [89, 90].

After cooling the YIG sample to room temperature, a polycrystalline Pt strip of thickness $t_{Pt} = 10\ nm$ was deposited ex-situ on the top of the YIG film via DC magnetron sputtering (TC-Orion-AJA sputter system) in Ar^+ plasma with pressure of the order of $3 - 8 \times 10^{-3}\ mbar$. The pattern was prepared by using a paper shadowmask.

Prior to the Pt strip deposition, a brief Ar^+ ion etching step was performed to remove any contaminant from the YIG surface to ensure optimal interface quality. In the ion etching, the sample is exposed to a 50 W Ar plasma for 5 seconds. Therefore, the interaction of the ions with the surface removes possible contaminants but also part of the YIG. Figure 14 illustrates the process steps of YIG/Pt bilayer fabrication.

The main principles of the magnetron sputtering process are illustrated in figure

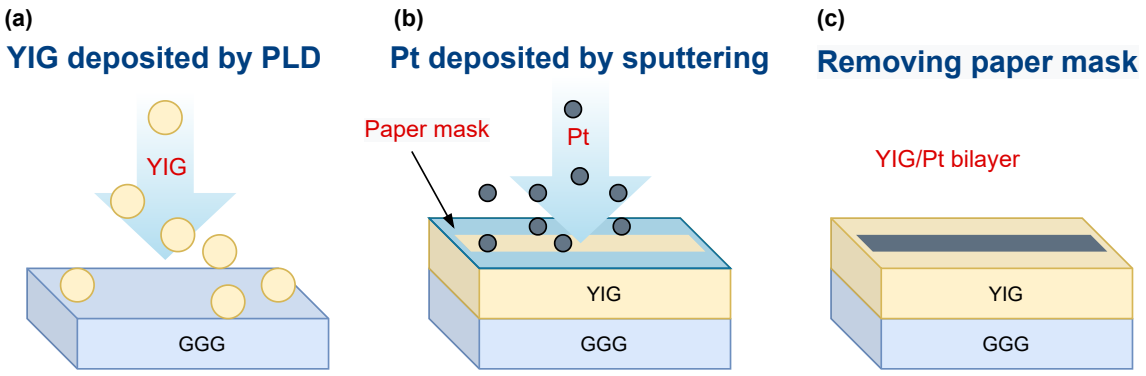

Figure 14. YIG/Pt fabrication procedure. **(a)** YIG deposited by PLD. **(b)** Pt strip is deposited using magnetron sputtering using shadow mask on YIG thin film previously deposited. **(c)** YIG/Pt bilayer finished.

15. Two electrodes are placed in low-pressure argon atmosphere. The conductive material to be deposited (the target) is mounted on the target holder which is held at negative potential. A set of permanent magnets is located under the target holder. A sufficiently high voltage is applied between the electrodes, resulting in the ionization of the argon and the ignition of a glow discharge, creating a plasma where the ions and electrons are separated. The combination of both electric and magnetic fields cause the electron to spiral in the vicinity of the target surface, thereby increasing the probability that electrons will strike the argon gas generating ions. Ar-ions are accelerated towards the target and upon hitting its surface sputter out the material, which subsequently forms a thin film on the substrate, located above the target [158, 159].

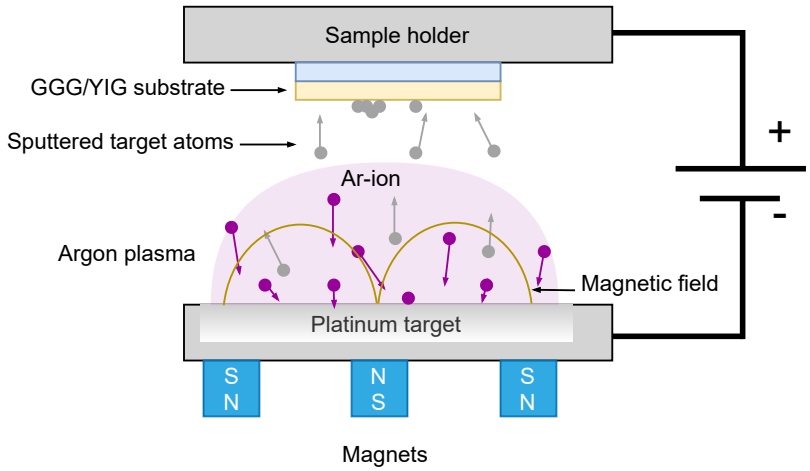

Figure 15. Schematic representation of the magnetron sputtering process. Target atoms are knocked out by Ar^+ ions and deposited at the heated substrate. Permanent magnets confine the plasma.

3.3 Structural characterization

The crystalline quality, thickness, perpendicular lattice parameter, mass density and lattice strain of the grown YIG thin films were investigated by X-ray diffraction and X-ray reflectometry measurement techniques on a commercial high resolution X-ray diffraction device (Malven-Panalytical X'Pert-PRO MRD) using $Cu\ K_{\alpha_1}$ radiation of wavelength $\lambda = 0.15406\ nm$.

3.3.1 X-ray diffraction (XRD)

X-ray diffraction (XRD) is a powerful and non-invasive method for determining how the atoms of crystalline solids are arranged, relying upon the diffraction of electromagnetic radiation by the periodic atomic structure. The interaction of electromagnetic waves with periodic structures produces diffraction effects if the wavelength and the periodicity of the crystals are of similar magnitude. X-rays are used to study both crystalline and amorphous structures because their wavelengths are in the scale of crystal interatomic distances (on the order of $0.15 - 0.4\,nm$) [160]. The incident X-rays are scattered elastically (also named Thomson scattering) by electrons surrounding the atomic nuclei, where the scattering is produced in all directions. Figure 16 shows the basic XRD setup. X-rays fall upon the surface of the sample at an angle θ and

reflected X-rays are detected at angle 2θ. For materials with periodical structure, such as crystals, which are composed of a repeating lattice structure, an incident X-ray beam of a single wavelength λ is reflected successively on the different atomic planes, as shown in the amplification of figure 16, resulting in constructive or destructive interference of scattered radiation. In this process, the wavelength of X-rays is conserved and retains its phase relationship to the incident wave. Bragg's law (1931) [161] gives the simple geometrical condition for constructive interference. For constructive interference, Bragg's diffraction condition is satisfied if the path difference lengths are a multiple integer of the X-rays wavelength:

$$n\lambda = 2d_{hkl}\sin\theta \tag{44}$$

In equation 44, n is an integer corresponding to the order of diffraction, λ the wavelength of the incident beam, d_{hkl} is the lattice spacing between crystallographic planes with hkl Miller indices. The orientation of the family of atomic planes within the crystal is given by three numbers $[hkl]$, and θ correspond to the angle of incidence with respect to the sample's lattice planes for which the peak occurs. Note that for X-ray, θ is typically measured from the plane and not from the normal to it [162].

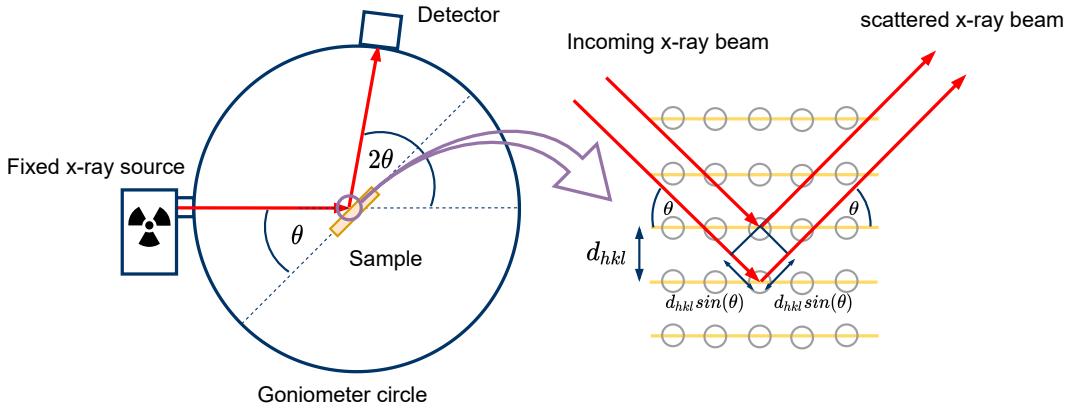

Figure 16. Basic components of an XRD setup, consisting of an X-ray source, sample stage and detector. Magnification shows a schematic description of Bragg's law.

Figure 17 shows high angle XRD $\theta - 2\theta$ scans in the region of of $GGG(444)$ substrate peaks and $YIG(444)$ peaks for samples deposited under similar growth

parameters. Films grown at high laser fluence (4.0 J/cm^2 for samples $YIG38$, $YIG42$ and $YIG47$) showed resolved Laue oscillations, or thickness fringes, flanking the $YIG(444)$ Bragg peak. These satellite oscillations are indicative of high crystalline quality, and smooth film/substrate interface [150]. Laue oscillations are caused by the interference of coherent X-ray waves by the conventional crystalline atomic planes and, in the case of a thin film, by the whole finite film thickness between the free surface and the interface with the substrate. Therefore containing information about the dimension and the crystalline disorder (crystal coherence) of the crystal in the normal direction [163, 164]

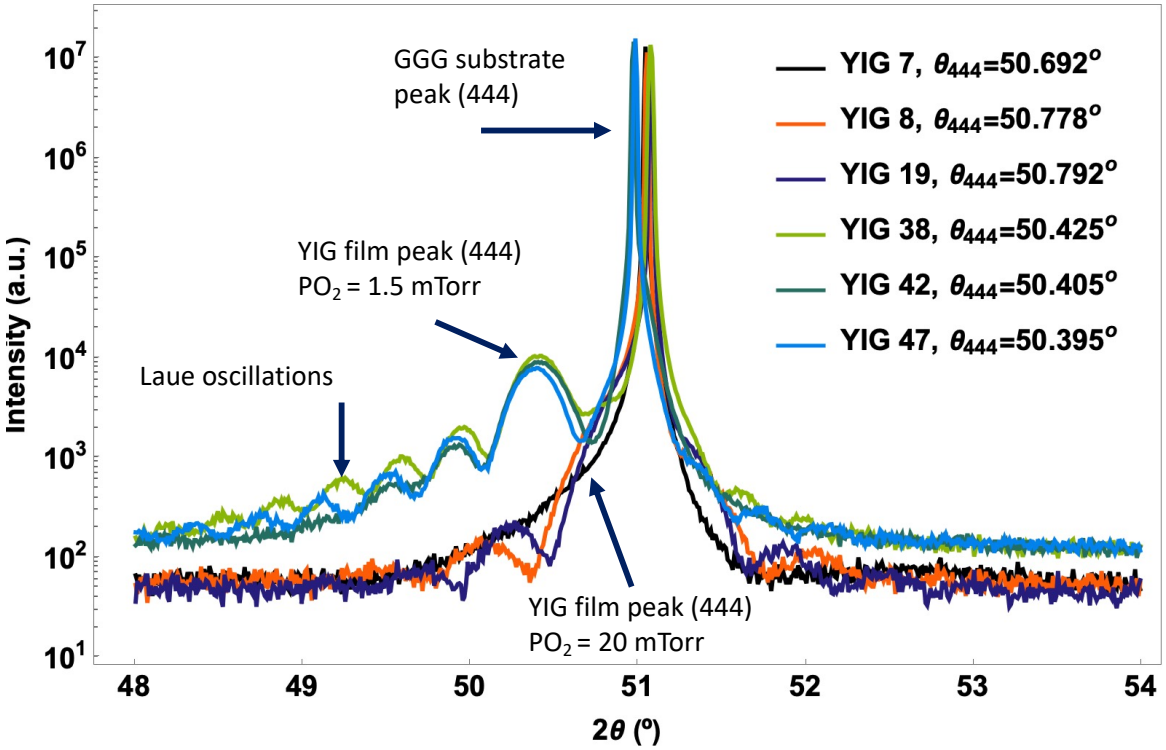

Figure 17. HRXRD 2θ- θ scans around the YIG(444) and GGG(444) peaks for selected films. Samples YIG38, YIG42 and YIG47 show clear Laue oscillations.

The film thickness can be determined from the positions of the satellite oscillations in the XRD pattern using the following equation [165, 166]:

$$t = \frac{\lambda}{2\left(\sin\theta_{i+1} - \sin\theta_i\right)} \tag{45}$$

where t is the film thickness, λ is the X-ray wavelength, and θ_{i+1} and θ_i are two adjacent maxima or minima satellite angles. Additionally, since YIG crystal has a cubic structure, its lattice parameter a_{YIG} can be evaluated from [167]:

$$a_{YIG} = \frac{\lambda\sqrt{h^2+k^2+l^2}}{2\sin\theta} \tag{46}$$

where λ is the X-ray wavelength, θ is the Bragg diffraction angle, and $[hkl]$ are the Miller indices of the corresponding XRD peak. In this work, the out-of-plane parameter and thickness of the films were calculated from the 2θ position of the 444 reflection and their satellite oscillations respectively. In this way, the values determined by the lattice constant are perpendicular to the film surface. Values of the film thickness and the out-of-plane lattice parameter obtained from XRD are listed in table 2.

Compared to the lattice parameter value of $a_{YIG} = 12.376$ Å for bulk YIG, the samples involved in this study show a slight increase in the out-of-plane lattice constant implying in-plane tension or strain between YIG film and GGG substrate. The thin film growth process above a dissimilar crystalline substrate can induce mechanical stress on the thin film when trying to accommodate the lattice structure. Since the material can freely expand or contract in the direction perpendicular to the interface, only stresses in lateral directions occur, called in-plane biaxial stress. In order to perform a structural characterization of the growth films, they are assumed a perfect cubic structure. However, the experimental evidence shows that the crystalline structure of YIG films in this work present a slightly rhombohedral distortion similar to that reported in other studies [168].

The usual measurement to quantify the strain is the out-of-plane lattice mismatch, defined as the relative difference between a nominally unstrained reference lattice parameter (substrate) and the lattice parameter for the strained material (film). Equation 47 provides the definition of lattice mismatch [169, 170], where a_{film} and $a_{GGG} = 12.383$ Å [171] are the bulk lattice constant of an epitaxial film and substrate, respectively.

$$\frac{\Delta a}{a_{GGG}} = \frac{a_{film} - a_{GGG}}{a_{GGG}} \times 100 \tag{47}$$

Table 2. Results from XRR and XRD analysis

Sample	XRR thickness nm	XRD thickness nm	Lattice constant Å	Mismatch %	Critical angle deg	Electron density $(\times 10^6)\ electrons/cm^3$	Mass density g/cm^3
YIG 7	–	5	12.466	0.67	–	–	–
YIG 8	–	14.8	12.447	0.52	–	–	–
YIG 19	18.8	18.4	12.444	0.49	0.2863	3.85	4.07
YIG 38	28.4	27.4	12.529	1.18	0.2990	4.20	4.44
YIG 42	32.8	25	12.533	1.21	0.2891	3.93	4.15
YIG 47	26.2	25.5	12.535	1.23	0.2921	4.01	4.24

If the lattice mismatch is relatively small, the grown film may strain (in-plane tensile strain if $\Delta a/a_{GGG}$ is negative or in-plane compressive strain if $\Delta a/a_{GGG}$ is positive) and the mismatch strain at the interface is compensated by elastic deformation in the perpendicular direction [172]. A cross-sectional atomically resolved transmission electron microscopy (TEM) image of YIG 8/ GGG interface is presented in figure 18(a). The TEM image confirms the previous XRD analysis and reveals a fully strained structure throughout the film thickness with, apparently, no local structure distortions and dislocations at the interface. Using the lattice constant of YIG films obtained from equation 46, the out-of-plane lattice mismatch values has been determined to be in the range between 0.49 % and 1.23 % (see table 2). The average lattice mismatch between YIG and GGG is $\Delta a/a_{GGG} = 0.88\%$. The slight increase in the YIG lattice constant is related to the defect structure of the layers, probably originated from the existence of oxygen and iron vacancies [173, 174] and Ga or Gd diffusion from the substrate [175]. Furthermore, first-principles studies have demonstrated that the intrinsic defects, such as yttrium ions situated in the iron octahedral sites, and vice versa, called antisite defects, result in an increase in the YIG lattice constant [176]. EDS analysis indicates the possible presence of Gd and Ga in the YIG film. A schematic representation of heteroepitaxial growth of strained film is presented in figure 18(b).

Starting from the information obtained by X-ray diffraction, we can be sure that there is a tension in the interface, hence the lattice parameter in the perpendicular direction is slightly greater than the ideal YIG. This tension can be relaxed presumably through dislocations or discontinuities, which can serve as scattering centers.

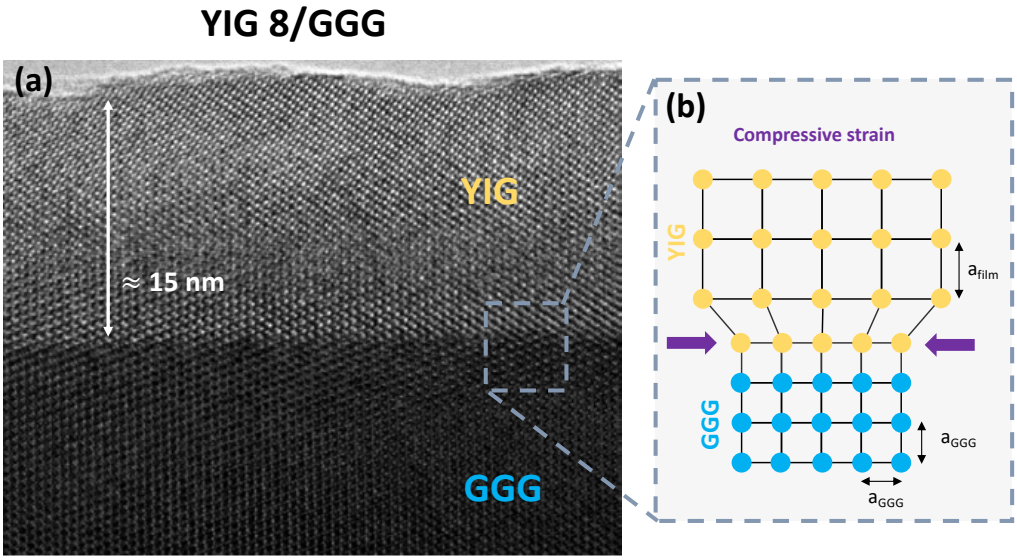

Figure 18. **(a)** TEM image of the YIG 8/GGG interface. **(b)** Schematic of the planar model showing interfacial compressive strain induced by lattice misfit between substrate and film with different lattice parameters.

3.3.2 X-ray reflectivity (XRR)

X-ray reflectivity (XRR) can be used to determine the film thickness, electron density perpendicular to the surface, boundary layers roughness and density of ultra-thin films and film systems on very smooth substrates. The technique involves measuring the reflected X-ray intensity as a function of incidence angle over a range of angles close to the critical angle, θ_c, for total reflection. Above this critical angle, the specularly reflected intensity decreases exponentially, with a form that is dependent on the structural properties of the interface and top surface. For X-ray interaction with matter the index of refraction can be written as [177]:

$$n = 1 - \delta + i\beta \tag{48}$$

where $\delta = \lambda^2 r_e \rho_e / 2\pi$ and $\beta = \lambda \mu_x / 4\pi$, are the dispersion and absorption coefficient of the sample, related to the electronic and mass density of the material respectively. $\lambda = 1.54060$ Å is the wavelength of X-rays which corresponds to the $Cu\ K_\alpha$ wavelength, $r_e = 2.818 \times 10^{-13}\ cm$ is the classical electron radius or Thompson

scattering length, ρ_e is the electron density of the material, and μ_x is the absorption cross-section density. For all materials, except for metals, typical δ values are usually in the range 10^{-5} - 10^{-6} and β is about 10 to 100 times smaller, so β can be ignored [178]. Consequently, the refractive index of X-ray differs slightly from the vacuum value ($n_{vacuum} = 1$). Since n is lower than one, there exists a critical angle of incidence θ_c below which an X-ray beam travelling from the air is totally reflected by the medium (external total reflection), analogously to visible light optics. The critical angle for total reflection can be derived, in absence of attenuation and small angle approximation, by a Taylor expansion of Snell refraction law: $cos(\theta_i) = n\,cos(\theta_t)$ with $\theta_i = \theta_c$, $\theta_t = 0$ and the approximate form of equation 48, $n = 1 - \delta$, what results in:

$$\theta_c \approx \sqrt{2\delta} \tag{49}$$

For incidence angles higher than θ_c, part of the incident beam penetrates into the film and is reflected at the film/substrate interface. The reflected intensity drops according to the Fresnel law.

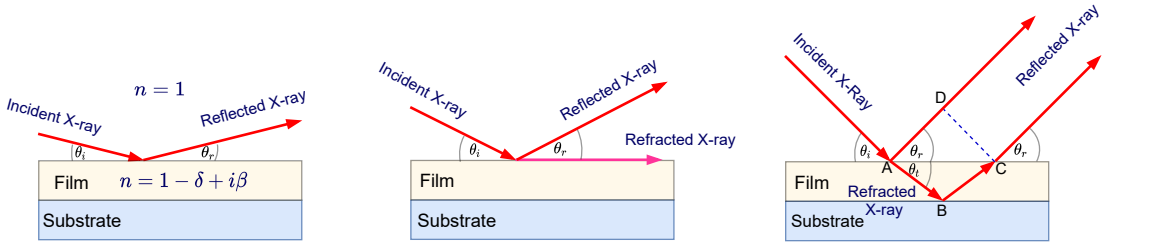

Figure 19. Schematic of X-ray reflectivity measurement. **(a)** When the incident angle θ_i is smaller than the critical angle θ_c, all incident X-rays are reflected. **(b)** When $\theta_i = \theta_c$ incident X-rays are refracted along the boundary between the two media. **(c)** If $\theta_i > \theta_c$ the incoming X-ray can undergo absorption, reflection and refraction.

In a thin film, the incident X-ray beam is reflected by the film surface and the film-substrate interface, what gives rise to periodic oscillations which are the result of constructive and destructive interferences between the reflected waves [179]. This

oscillations are called Kiessig fringes, after H. Kiessig who published on this phenomenon in 1931 [180]. The period of the interference fringes and the decay in the intensity are related to the thickness and the roughness of the film surface and the film-substrate interface, respectively. The thickness of a thin layer can be obtained from the optical pathlength difference between the beam reflected at the air/film and film/substrate interfaces. Figure 19(c) shows the schematic diagram of reflected and refracted X-ray beams on a single layer of thickness t. From this diagram, the difference in the optical path for the reflected rays is given by:

$$\Delta = (AB + BC)n - AD \tag{50}$$

where n is the refractive index of the film, and since $AB = BC = t/\sin\theta_t$ and $AD = 2tn\cos^2\theta_t/\sin\theta_t$, the equation 50 becomes $\Delta = n2t\sin\theta_t$. Constructive interferences are observed whenever the optical phase difference between the beams is a multiple of the wavelength of x-rays. This condition can be expressed by [181]:

$$m\lambda = \Delta = 2t\sqrt{\sin^2\theta_m - \sin^2\theta_c} \tag{51}$$

where λ is the wavelength of X-ray, m is an integer number, corresponding to the diffraction order, t is the film thickness and θ_m is the incidence angle at which the interference maximum of order m occurs. In most cases, the incidence angle is sufficiently small and the equation 51 has the following approximate form [160]:

$$m\lambda \approx 2t\sqrt{\theta_m^2 - \theta_c^2} \tag{52}$$

where m, θ_m and θ_c are extracted from the XRR curves shown in Figures 21(a), 21(c), 21(e) and 21(g).

This relation shows a simple method to determine the layer thickness by analysing the angular distributions of the resulting interference pattern in the reflectivity curve, using the equation 53, averaging on many fringes.

$$t \approx \frac{m\lambda}{2\sqrt{\theta_m^2 - \theta_c^2}} \tag{53}$$

Another approach to evaluate thickness values is based on fitting equation 54:

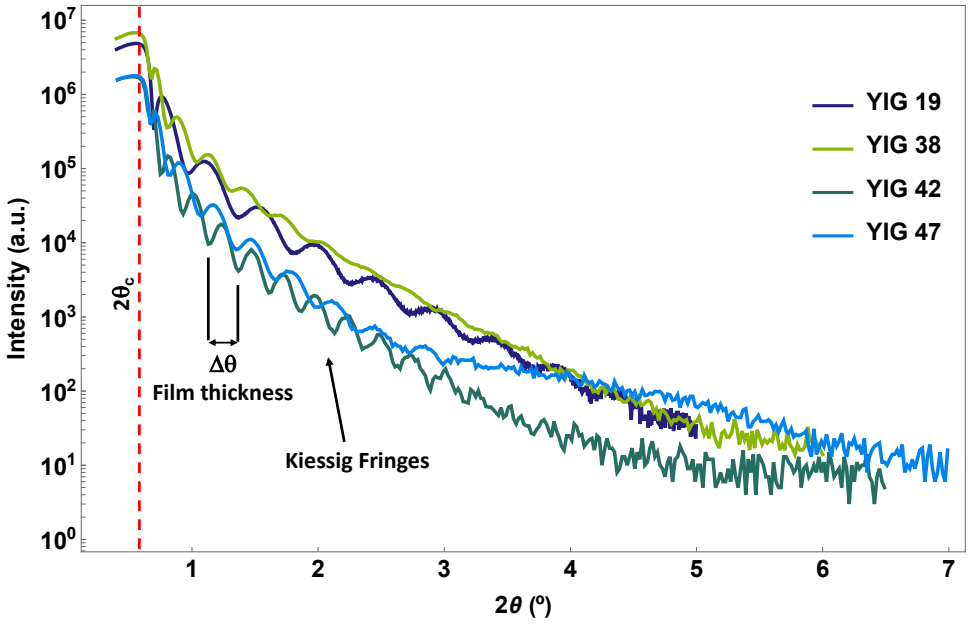

Figure 20. XRR measurements in logarithmic scale of the samples YIG 19, YIG 28, YIG 42 and YIG 47. The period of the observed Kiessig fringes,$\Delta\theta$ is inversely related to the thickness of the films

$$\theta_m^2 = \frac{\lambda^2}{4t^2}m^2 + \theta_c^2 \tag{54}$$

Here, the square of the angular values of the reflectivity maxima θ_m (in radians) versus the square of their order m. The thickness is obtained from the slope of the fitted line, while the intercept corresponds to the square of the critical angle [181], from which and according the equation 49, the absolute electron density ρ_e can be computed for each film [166] by using equation 55.

$$\rho_e = \frac{\pi\theta_c^2}{\lambda^2 r_e} \tag{55}$$

Figure 20 shows the reflectivity curves of samples YIG 19, YIG 38, YIG 42 and YIG 47. Kiessig fringes were clearly observed above the critical angle, indicating a homogeneous growth of YIG and good surface and interface quality. [182]. For all YIG/GGG bilayers deposited, Figure 21 exhibits the reflectivity curves, plot of θ_m^2 versus m^2 and their fitting according to equation 54. From this linear fit, the calculated

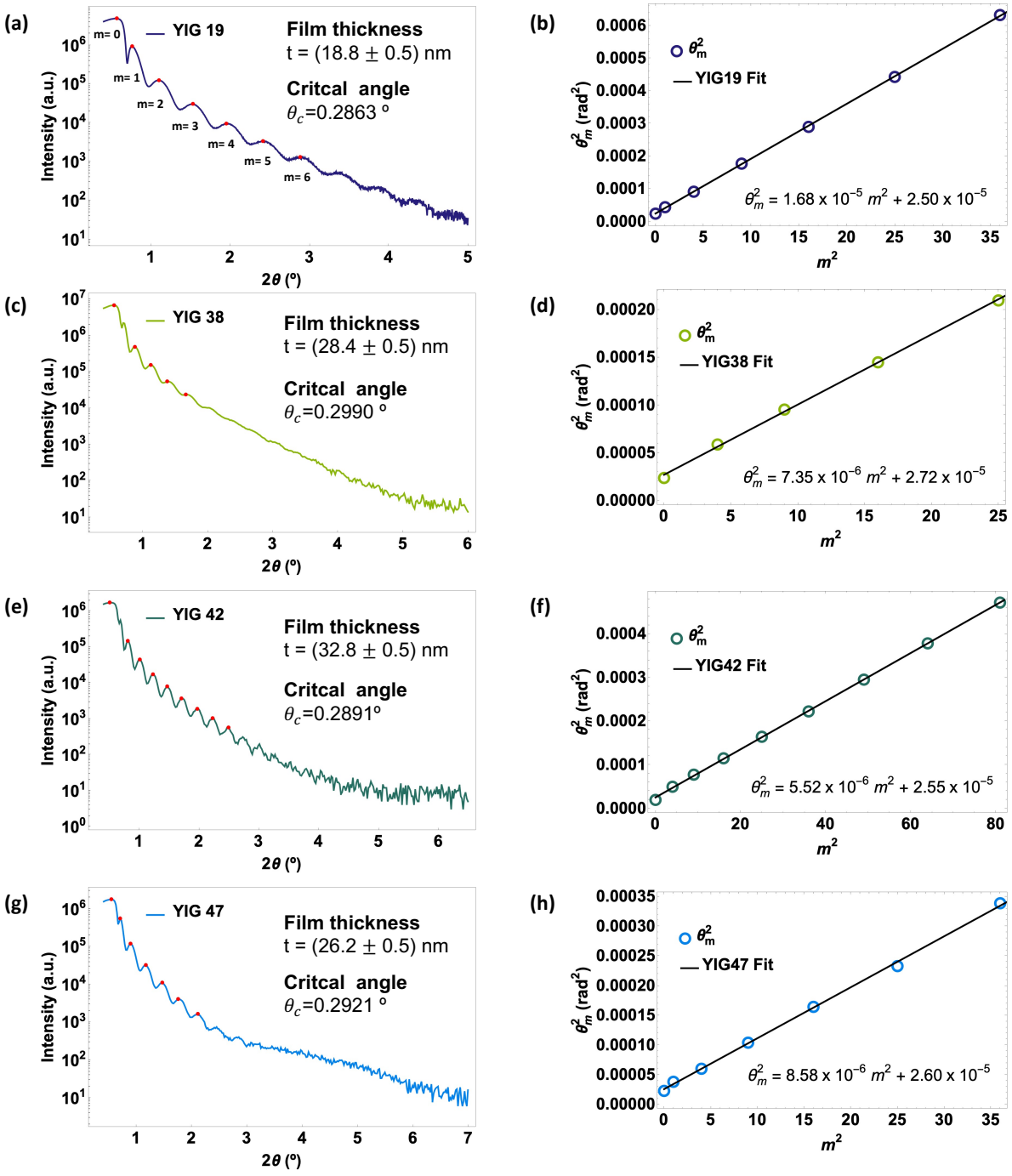

Figure 21. **(a)**, **(c)**, **(e)** and **(g)** XRR data plots. Red dots correspond to the angular values of the reflectivity maxima of each order m. **(b)**, **(d)**, **(f)** and **(h)** are the linear fits, based on equation 54, of θ_m^2 vs m^2 data for each sample. This analysis is used to determine the film thickness.

critical angle θ_c stays essentially constant, verifying the very good reproducibility of the material properties for the films grown by PLD technique. The critical angle depends on the X-rays energy and sample mass density. The critical angle, electron density and thickness of YIG layers are summarized in Table 2.

XRR provides a non-destructive technique for measuring mass density in a thin film and, so, determining the thin film optical constant. When the stoichiometric composition and the absolute electron density of a material are known, the mass density ρ (in g/cm^{-3}) is given by [183]:

$$\rho = \frac{\pi\theta_c^2}{N_A r_e \lambda^2} \frac{\sum_i x_i}{\sum_i x_i \mathrm{f}_i / M_i} \tag{56}$$

where, $N_A = 6.02214154 \times 10^{23}\ mol^{-1}$ is Avogadro's number, the subscript i refers to different atomic elements in the unit volume ($i = \{Y, Fe, O\}$), x_i is the proportion of element of type i, $\lambda = 1.54060 \times 10^{-10}\ m$ is the wavelength of incident X-ray, M_i is the molar mass of each element in g/mol and f_i is the real part of atomic scattering factor for each i element. Atomic scattering factor is a measure of the scattering amplitude of an electromagnetic wave scattered by an isolated atom, and depends on the number of electrons (Z). However, if the incident X-ray radiation has a frequency close to the natural oscillation frequency of the electrons of the atom, the so-called anomalous dispersion. In order to account for the anomalous dispersion occurs, a correction has to be applied to the atomic scattering factor: real correction $\mathrm{f}_1(E)$ and imaginary correction $i\mathrm{f}_2(E)$ at the energy $E = hc/\lambda$, which describe the dispersive and absorptive interactions [163]. Therefore, the real part of atomic scattering factor is given by:

$$\mathrm{f} = Z + \mathrm{f}_1(E) \tag{57}$$

Figure 22 shows the real part of the complex atomic scattering factor for *yttrium*, *iron* and *oxygen* as a function of X-ray energy computed by using the tabulated values from [184, 185]. Red line shows the position of atomic scattering factor at X-ray energy $E = 8044.06\ eV$ corresponding to the wavelength $\lambda = 1.54060 \times 10^{-10}\ m$ (used in x-ray characterization for this study). The inset shows the molar mass of the atoms that compound the YIG [186].

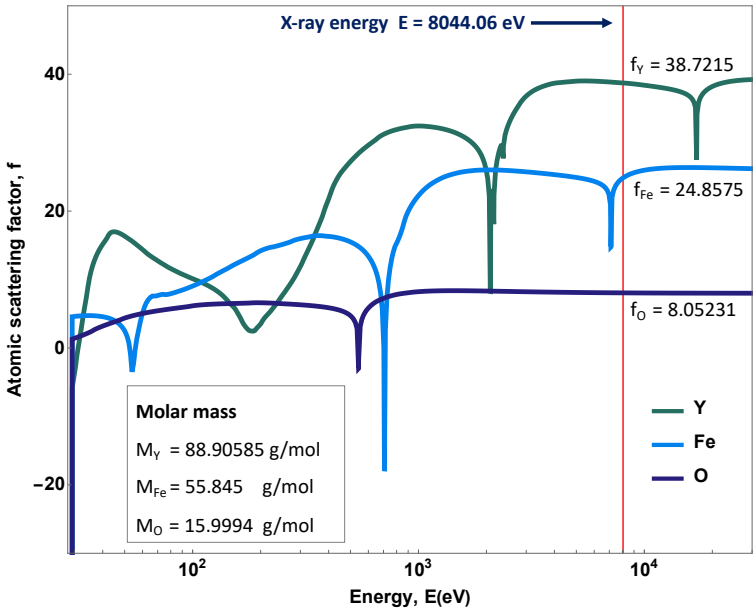

Figure 22. Atomic scattering factor of yttrium, iron and oxygen atoms as a function of incident X-ray energy computed by using the tabulated values from [184].

The average mass density of the bulk measured is 4.23 g/cm^3, which correspond to 82% of the theoretical density for pure YIG (5.17 g/cm^3) [143].

Finally, as we can see in Table 2, both methods used to determine the YIG films thickness on GGG substrate, show consistent results, however sample $YIG42$ shows a discrepancy of about 8 nm. We can explain this result considering that the XRR method is related to the global thickness of the film, while the XRD method is related to the thickness of the coherent part of the film, that is, we can attribute this discrepancy to a lost of coherence either by amorphization or by the presence of structural defects.

3.4 Magnetic characterization

The FMR absorption measurements for each of the studied YIG films were performed at a fixed microwave frequency in the range from 3 GHz to 17 GHz, while sweeping the external magnetic field up to 5 kOe. The magnetic field was applied in the in-plane (IP) configuration along the surface of the film. All measurements were performed at room temperature. Figure 23(a) shows the experimental FMR absorption spectrum of YIG 8 sample. In order to extract the resonance field and peak-to-peak linewidth at a specific frequency (e.g. 11 GHz), each of the FMR spectrum is fitted with the first derivative of an asymmetric Lorentzian function [187, 188], given by:

$$S = \frac{d}{dH}\left[\frac{A^{SYM}\Delta H^2 + A^{ANT}\Delta H(H_{res} - H)}{(H_{res} - H)^2 + \Delta H^2}\right] \tag{58}$$

where S is the signal of the asymmetric absorption spectrum at a specific frequency, ΔH_{PP} is the peak-to-peak linewidth and H_{res} is the resonance field. A^{SYM} and A^{ANT} are the amplitude of symmetric and antisymmetric parts of the signal, respectively. An example of a fitting result using equation 58 is shown by the solid purple line in figure 23(b).

From the extracted best fit parameters, we plot the the excitation frequency as a function of the resonance field shown in figure 23(c) and the linewidth as a function of excitation frequency as can be seen in figure 23(d). The data in figure 23(c) matches perfectly with the revisited Kittel formula given by equation 37. From the fit of the experimental data with the Kittel equation, we obtain the reduced gyromagnetic ratio $\gamma/2\pi$ and the effective magnetization $4\pi M_{eff}$, as best fit parameters. In figure 23(d) the linewidth fitting was performed by using the equation 43. As a result, the nonlinear behavior is described by the TMS contribution to damping.

In figure 24, experimental data for six films, represented by different symbols, are compared with theoretical curves (solid lines) defined by revisited equation 37. Their respective $4\pi M_{eff}$ and $\gamma/2\pi$ best fit parameters are listed in table 4. The gyromagnetic ratio value of all samples is in reasonable agreement with the standard values reported for YIG (2.8 GHz/kOe) [189, 190, 191].

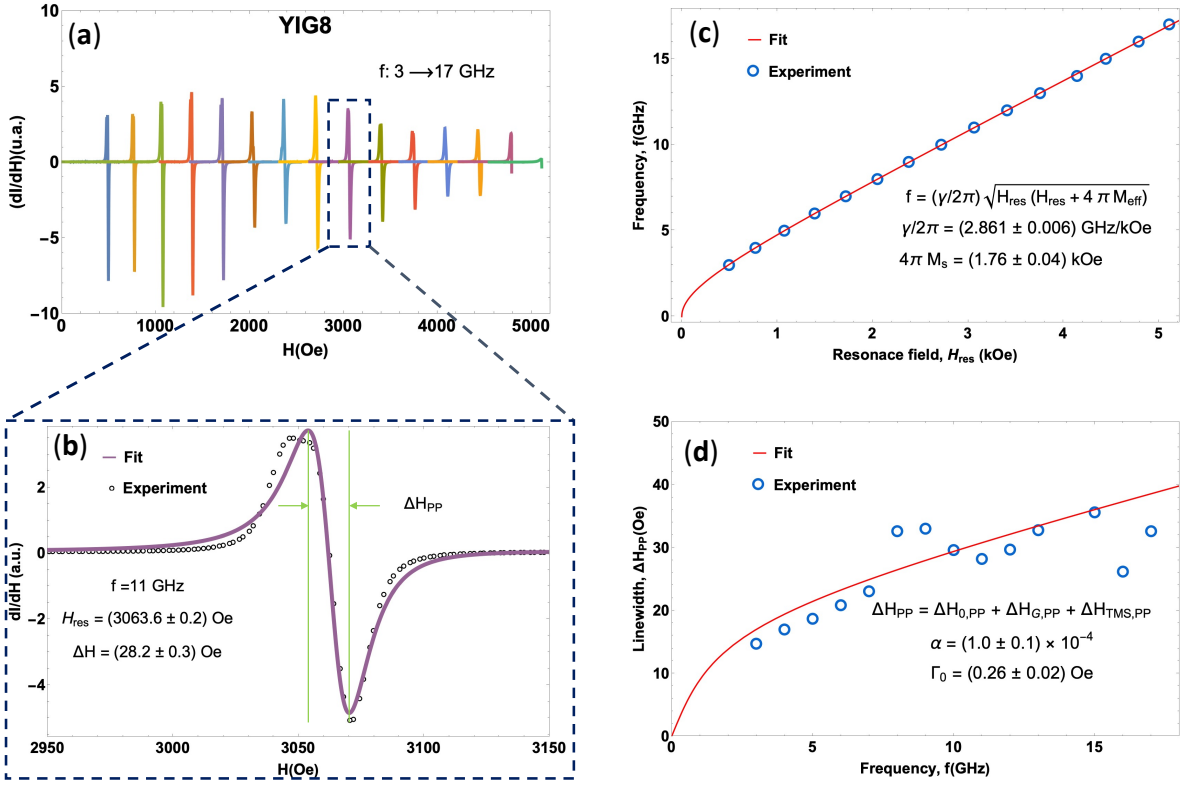

Figure 23. Ferromagnetic resonance analysis in YIG 8 sample. **(a)** FMR signal at room temperature for microwave frequencies ranging from 3 to 17 GHz in steps of 1 GHz. **(b)** FMR absorption spectrum at 11 GHz (open circles) and its fitting curve (purple curve). **(c)** Excitation frequency as a function of resonance field, overlaid with a fit to equation 36. The calculated reduced gyromagnetic ratio and the effective magnetization are displayed on the graph. **(d)** The frequency dependence of FMR peak-to-peak linewidth. The open circles show the data and the solid red line shows the fit according to equation 43. $\Delta H_{0,pp}$ is a frequency-independent inhomogeneous broadening, $\Delta H_{G,pp}$ is the Gilbert damping linewidth from which we can extract the Gilbert parameter α and ΔH_{TMS} represent the extrinsic two magnon scattering linewidth contribution, whose intensity is given by Γ_0.

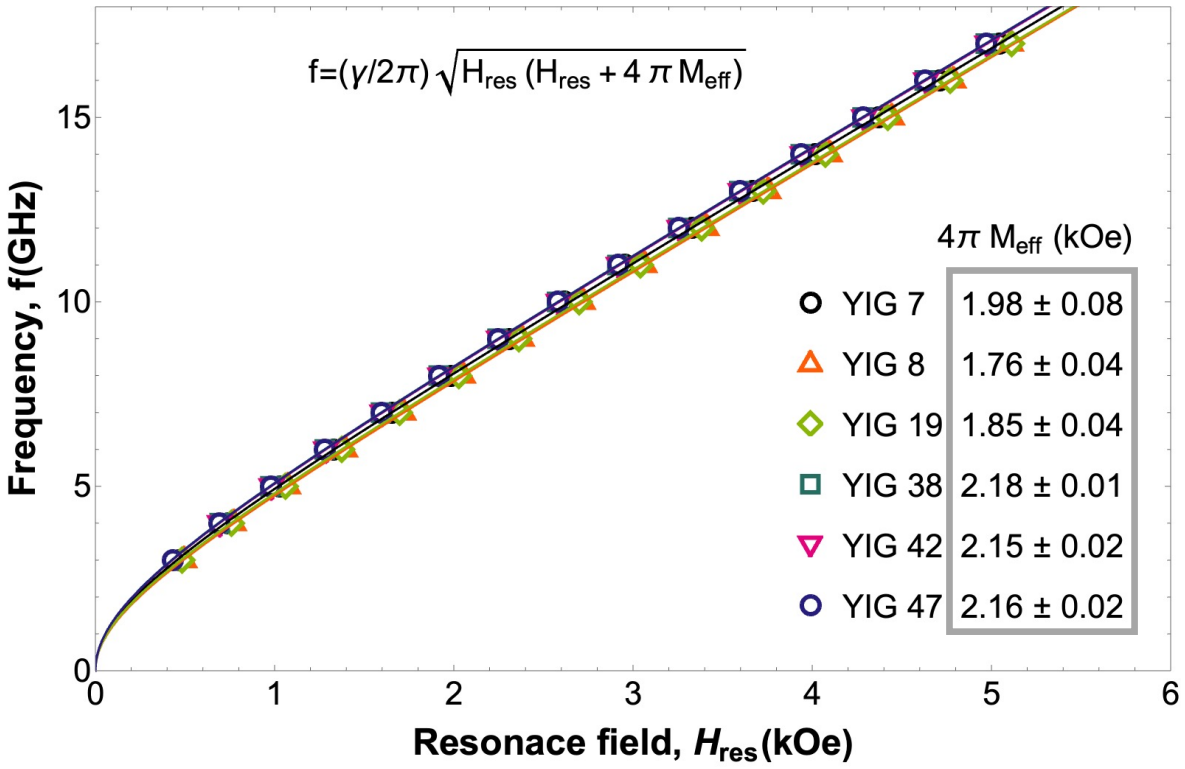

Figure 24. Ferromagnetic resonance frequency as a function of resonance magnetic field for all samples. The inset shows a close-up of the Kittel fits, represented by solid lines. From the linear fit we extract the value of the effective gyromagnetic ratio ($\gamma/2\pi$) and the effective magnetization of each sample.

The effective magnetization values are obtained from the fitting as show in figure 24. The magnetization at saturation can be obtained from the definition of effective magnetization, given by $4\pi M_{eff} = 4\pi M_s - H_{ani}$ where H_{ani} is defined in equation 38 with the values of anisotropy constants for YIG $K_1 = -6100\, erg/cm^3$ and $K_2 = -260\, erg/cm^3$. The effective uniaxial anisotropy field H_{ani} can be calculated once known both the saturation magnetization $4\pi M_s$ (from magnetometry measurements) and the effective magnetization (from FMR). The saturation magnetization values of almost all samples are above the value of the bulk YIG film, than ranges from 1.73 to 1.78 kOe [192]. Similar $4\pi M_s$ values have been reported for YIG thin films growth on GGG by; (i) magnetron sputtering with thicknesses between 4 and 250 nm

obtaining values of $4\pi M_s$ in the range 2.172 to 2.141 kOe [193] or ii) growth by PLD with thicknesses 7, 15, and 20 nm giving $4\pi M_s$ values of 2.100 kOe [173, 194]. Table 3 listed $4\pi M_{eff}$, $4\pi M_s$ and H_{ani} for our reported samples.

Higher values of $4\pi M_{eff}$ can be explained by the presence of a negative uniaxial anisotropy field given by equation 38. Assuming that the crystal structure of the YIG is still cubic, a negative H_{ani} can be caused by compressive stress [153] in the film plane, originated by a lattice parameter expansion in the YIG film [151, 195, 196, 197]. As already mentioned above, this expansion can be originated by iron deficit and antisite defects which induces a rhombohedral lattice distortion [152].

Table 3. Effective Magnetization, saturation magnetization and surface anisotropy field

Sample	$4\pi M_{eff}(kOe)$	$4\pi M_s(kOe)$	-$H_{ani}(Oe)$
YIG 7	1.98±0.08	1.90 ±0.07	87.9 ±0.2
YIG 8	1.76±0.04	1.66 ±0.04	100.24 ±0.02
YIG 19	1.85±0.02	1.76 ±0.02	94.79 ±0.01
YIG 38	2.18±0.01	2.10 ±0.01	80.0±0.8
YIG 42	2.15±0.02	2.07 ±0.02	80.4 ±0.1
YIG 47	2.16±0.02	2.08 ±0.02	81.1 ±0.2

The main property that characterizes a magnonic material is the Gilbert damping parameter, which has to be as small as possible. In order to precisely determine the Gilbert damping parameter α, the inhomegeneous linewidth broadening ΔH_0 and the strength of TMS (Γ_0) of all samples, we fit of the linewidth versus excitation frequency data with equations 42 and 43. From the best fit of Kittel formula, we calculate f_0. Figure 25 shows the whole set of obtained experimental linewidth values (open circles) and fitted curves (solid lines) in the frequency range between 3 to 17 GHz. The results of the described procedure are summarized in the last three columns of table 4. The obtained Gilbert damping parameter is in the range of $10^{-4} - 10^{-3}$, which is comparable with the lowest value so far reported in the literature for PLD grown YIG/GGG nanometer thin films [198, 150].

Table 4. Summary of the best fit parameters of the complete form of FMR linewidth given by equation 43

Sample	$\gamma/2\pi(GHz/kOe)$	$\alpha \times 10^{-4}$	$\Delta H^*_{0,PP}(Oe)$	$\Gamma_0(Oe)$
YIG 7	2.86 $\pm$0.01	7 $\pm$1	32 $\pm$1	1.00
YIG 8	2.861 $\pm$0.006	1.0 $\pm$0.1	8 $\pm$1	0.26
YIG 19	2.850 $\pm$0.003	2.2 $\pm$0.6	9 $\pm$1	0.28
YIG 38	2.853 $\pm$0.003	3.0 $\pm$0.2	9 $\pm$1	8.54×10^{-6}
YIG 42	2.854 $\pm$0.002	6.7 $\pm$0.6	23 $\pm$1	0.63
YIG 47	2.855 $\pm$0.004	7.2 $\pm$0.6	12 $\pm$1	1.18×10^{-5}

The non-linear behaviour of the linewidth with increasing excitation frequency is shown in figures 25(a) to 25(d) and it is a clear evidence of the extrinsic contribution to the linewidth. It also demonstrates the relevance of considering TMS in the magnetic relaxation process. The linewidth increase, caused by the TMS mechanism, is a measurement of the scattering rate of the uniform precession magnon into other spin-wave modes. TMS can only occur in the presence of scattering centers in the form of defects [199]. This fact is correlated with the existence of a high surface anisotropy due to structure defects or inhomogeneities of the composition in the vicinity of the film surface and film/substrate interface, and this fact is evidenced in the high value of H_{ani} [173] (see table 3).

It is necessary to remark that to obtain a correct estimation of ΔH_0, a measurement of the linewidth in the low frequency regime (below 9 GHz) is required. However, this quantity can be estimated from the intercept at zero frequency of the tangent line to the knee point of the fitted curve [133], as can be seen in subfigures 25(a) to 25(d), where we illustrate this by red solid lines. The extrapolated inhomogeneous linewidth is denoted as ΔH^*_0 and are listed in table 4. Alternatively, the inhomogeneous linewidth can be determined from the out-of-plane FMR measurement, assuming, of course, that the ΔH_0 is isotropic [200].

Samples YIG 38 and YIG 47, shown in figures 25(e) and 25(f) respectively, present a highly linear behavior of the linewidth and therefore a very low (almost negligible) two-magnon scattering strength parameter Γ_0 ($\sim 10^{-5}Oe$). This reveals highly ordered

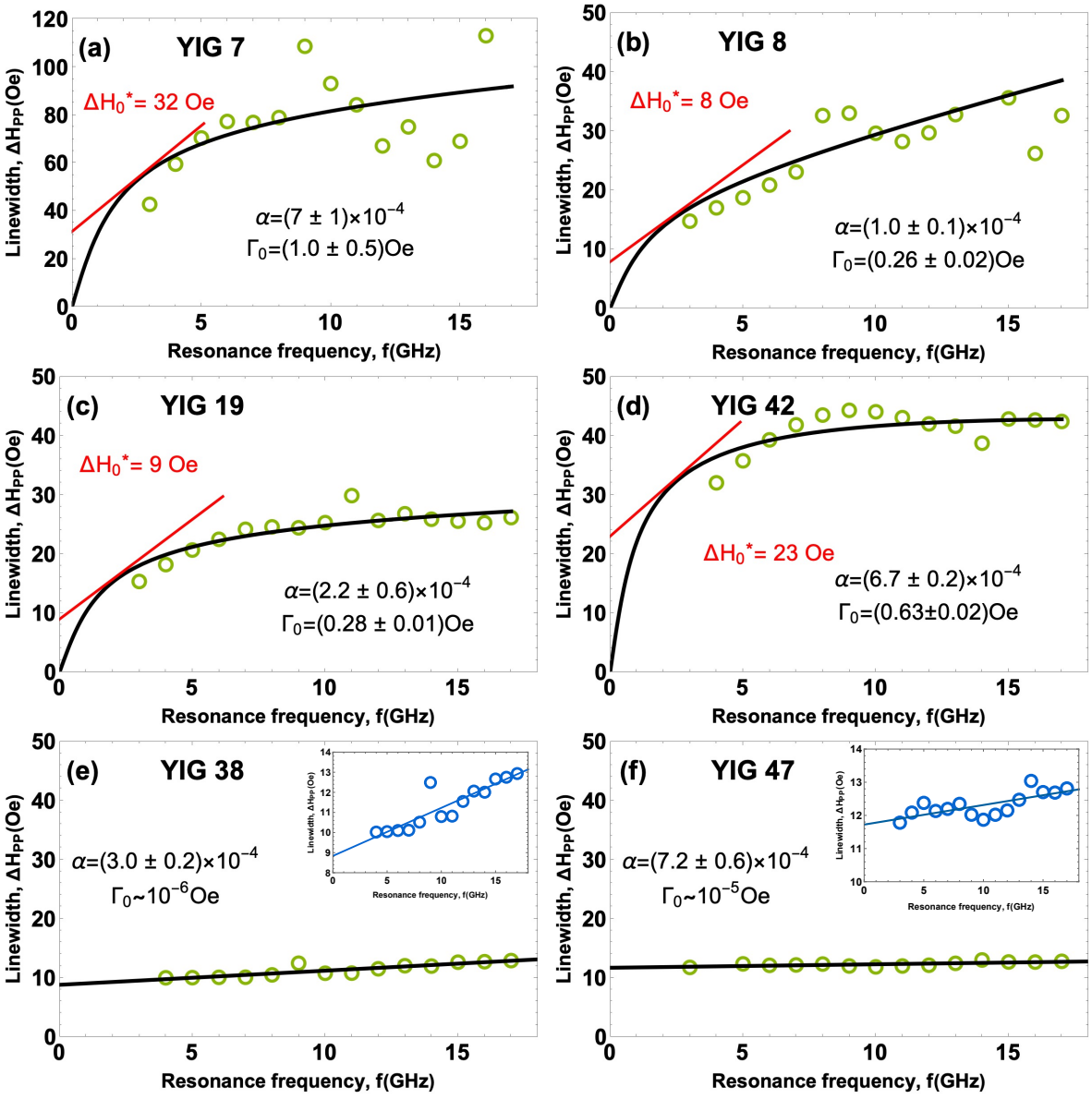

Figure 25. Frequency dependence of peak-to-peak linewidth for all samples. The open circles are experimental data. The black solid lines are fitting using equation 43. The calculated Gilbert damping parameter α and the strength of TMS contribution, Γ_0, are displayed on the graphs. Graphs **(a)-(d)** present a strong nonlinearity due to TMS. Graphs **(e)** and **(f)** present a linear frequency dependence due to a marginal contribution of TMS. The insets are intended to display the data on a more adequate scale. The red solid lines are tangent to the fitted curve at the "knee" point and their intercept at zero frequency gives the apparent linewidth broadening, ΔH_0^*, which is due to the spatial inhomogeneity of the YIG thin film.

films essentially free of defects and impurities. These samples also exhibit pronounced Laue oscillations around the Bragg pack (444) (see figure 17), indicating that the films are highly crystalline, ordered, and uniform [193] and the frequency-dependent magnetic relaxation is dominated by Gilbert damping. The calculated values of Γ_0 are summarized in the last column of table 4. Similar values of Γ_0, have been reported for other YIG thin films grown on GGG studies; in Dubs *et al.*[149] where the growth methods is liquid phase epitaxy, $\Gamma_0 \approx 0.5\ Oe$.

These results show that the TMS strength and the effective damping constant for YIG thin films reduce when increasing lattice strain (high lattice mismatch) [201, 202]. The absence of strain can be attributed to the coexistence of tilted grains (slightly rotation of the film unit cell with respect to the substrate and a series of misfit originated in the nucleation of dislocations at the interface) and well-relaxed Vernier of misfit (this relaxation mechanism occurs when the film and substrate tend to preserve its natural lattice constants because the interfacial bonding is weaker than the bonding within the film or the substrate) [203, 204]. On the other hand, the sample YIG 42 shows high TMS strength although it has a relatively high lattice mismatch. This is related to the higher degree of surface and interface roughness of this sample, which can be verified from the rapid decrease of the XRR spectra [205] shown in figure 20.

In summary, in this chapter we studied the structural and magnetic properties of ferrimagnetic iron garnet called YIG prepared in the form of single thin film by PLD technique on GGG substrates. The thickness values and out-of-plane lattice constant of the samples are derived from the HRXRD and XRR measurement techniques. The slight differences between both methods for determining the film thickness is indicative of incoherent growth close to the interface and this can be related to the generation of defects such as dislocations, grain boundaries, oxygen and iron vacancies, and antisite defects. On the other hand, the out-of-plane lattice constants for the YIG thin films are obtained from the HRXRD scans using the Bragg formulation, evidences a stretching of the order of 1%. The observed out-of-plane lattice expansion can be attributed to a small off-stoichiometry due to oxygen vacancies, migration of Ga^{3+} from the GGG substrate across the interface and antisite defects (Y^{3+} ions situated in

Fe^{3+} octahedral sites) which is an inherent one in YIG crystals. Besides, the relaxation of unit cell along the growth direction can be induced by the lattice mismatch between substrate and film. These intrinsic defects also affect the magnetic properties of YIG. In particular, FMR linewidth is broadened by surface/interface defects and inhomogeneities, leading to two spin relaxation mechanisms (i) transmission of energy from spin system into the lattice system (also called intrinsic mechanism) and (ii) internal transmission of energy into the spin system (also called extrinsic mechanism) where the energy is transferred from exited state to a degenerate magnon state via TMS, given rise to a nonlinear linewidth behavior respect to the resonance frequency in FMR experiments. The saturation magnetization values of the samples are higher that the bulk value, which can be attributable to (i) the negative anisotropy field originated in the compressive in-plane strain, and (ii) the suppression of magnetic moments in the minority octahedral sublattice.

Chapter 4
Spin Seebeck effect detection by harmonic analysis

Typically, the experimental report of SSE have all been done at a constant magnetic field, in magnetic saturation, and using different ways of generating a temperature gradient such as laser heating [206, 207], current-induced heating [208], and on-chip heater devices [209, 210]. The SSE signal is measured as a function of the temperature difference between Pt and the YIG layer and the orientation of the magnetic field with respect to the sample. In the setups previously mentioned, the thermal gradient is generated by passing an electric current along the Pt film, which produces undesired charge and spin transport effects that must be extracted thereafter. Another approach is to create a thermal gradient by ac heating and detect the SSE in the first [211] and second harmonic [212] response. AC heating improves the sensitivity and signal-noise ratio of the signal measured; however, magnetoresistive and electric drift contributions persist [213, 214].

In this chapter, the basics and experimental setup for detecting the spin Seebeck effect by an alternative technique based in harmonic analysis is described. The results of this study have been published in Appl. Phys. Lett. 116, 242402 (2020) [215]. We developed an alternative and simple method to detect in real time pure SSE signal, free of spurious effect, in magnetic insulator-based LSSE devices at low magnetic fields. The main idea of this technique is to induce a modulated V_{SSE} in the NM and analyze the different harmonics that constitute it. In the section 4.1, we demonstrate and prove that under a harmonic external magnetic field, the SSE signal can be measured by studying the odd harmonics of the total signal. Figure 26(a) sketches the experimental setup used to measure a spin Seebeck effect signal used in this thesis. In this setup, the total measured signal will be a linear combination of three sources: SSE, electromotive force caused by the rate of change of magnetic flux through the area associated with the circuit loop formed by the sample and the electrical contacts

and background electrical noise. The modulation of the signal is produced by the application of a sinusoidal magnetic field along the sample plane, while a static out-of-plane temperature gradient is induced by two external heat reservoirs. In the following section, we demonstrate that the SSE can be detected by analyzing the odd harmonics of the modulation frequency. To disentangle the SSE from the total signal measured, a lock-in detection technique is used to determine their in-phase and out-of-phase components.

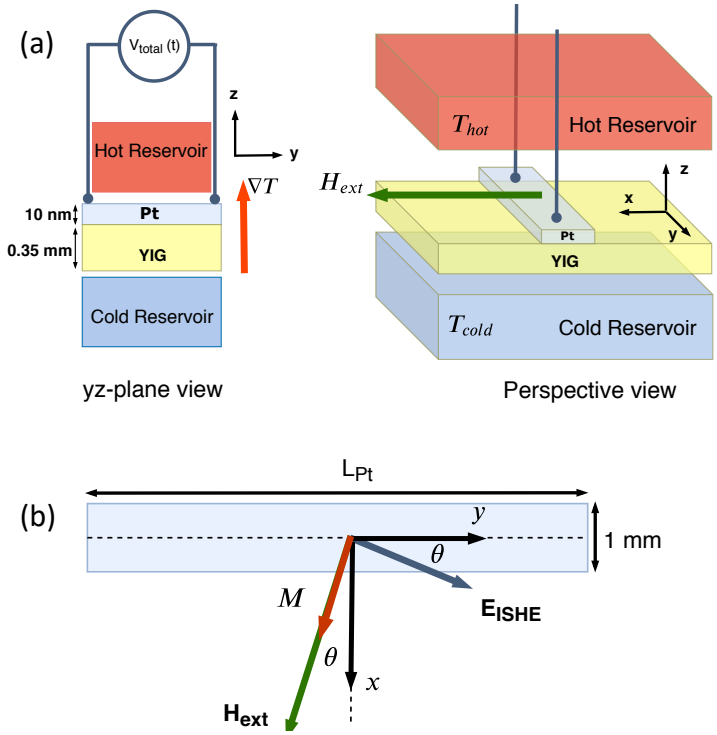

Figure 26. A schematic illustration of the insulator-based LSSE setup utilized in this work. **(a)** The yz-plane view shows the arrangement of the thermal reservoirs, which generate the thermal gradient necessary to induce the SSE. In the perspective view, we can observe the YIG/Pt sample sandwiched between two thermal reservoirs, which are in direct contact with the sample. The external magnetic field is applied parallel to the x-axis and varies sinusoidally with frequency f. **(b)** the xy-plane view of the setup, focused in the Pt layer, shows a representation of; M magnetization, H applied magnetic field, and θ azimuthal angle between the magnetic field and the x-direction. According to equation 59, the angle between $\boldsymbol{E}_{\mathrm{ISHE}}$ and y-axis is also θ.

The use of this detection technique has the following advantages over the conventional measurement techniques:

(a) magnetoresistive effects, such as the spin Hall magnetoresistance, can be completely removed.

(b) Only two electrical contact points are required, compared to the four (or more) contacts used in others techniques, thereby reducing the number of sources of unwanted and parasitic effects, such as thermoelectric artifacts.

(c) Only one lock-in amplifier is required to detect and measure the generated signal.

All measurements were carried out in the longitudinal SSE configuration at room temperature. The sample consists of a simple crystal YIG slab, (111) orientation, and a Pt strip sputtered on the YIG surface. The thickness of the YIG and Pt layers are about 0.35 mm and 10 nm, respectively. V_{total} is measured for Pt in the y direction using a mechanical microprobe system with two copper tips; the distance between tips is about 5 mm.

4.1 Harmonic analysis of the Spin Seebeck Effect induced by a.c. magnetic field

The application of a static thermal gradient ($\boldsymbol{\nabla} T$) across the bilayer interface along the $z-$direction and an alternating magnetic field ($\boldsymbol{H}_{ext}(t) = H_0 sin(\omega t)$), parallel to the sample plane along the $\pm x-$direction ($\boldsymbol{\nabla} T \perp \boldsymbol{H}_{ext}$), generate an electromotive force (EMF) in the Pt layer along the $y-$direction. The equivalent circuit model for the Pt/YIG bilayer film utilized in this work is shown in figure 27(a). In this model, the Pt layer acts as an ac-voltage source composed of two ideal ac-voltage sources connected in series. The electrical resistance (R) of the Pt layer acts as a load resistor. V_H is the voltage induced by the variation of the magnetic field flux through the circuit loop done by Faraday's law of induction. V_{SSE} is originated, via inverse spin Hall effect (ISHE), by the conversion of the spin current (produced by the SSE) and injected into the Pt layer from the YIG layer along the $z-$direction, into an electric field ($\boldsymbol{E}_{ISHE}$).

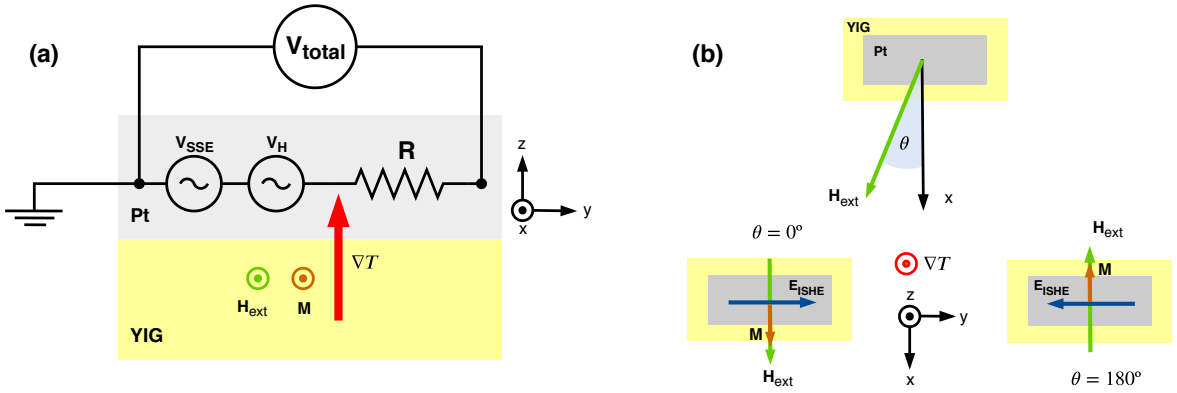

Figure 27. Equivalent circuit model for the Pt/YIG bilayer film utilized in this work. **(a)** A schematic illustration of the orientation of the external magnetic field $\boldsymbol{H}_{ext}$ and the thermal gradient. The external magnetic field oscillates harmonically along the direction defined by θ (θ is measured with respect to the x-axis in clockwise sense). It also shows the special cases for $\theta = 0°$ and $\theta = 180°$. **(b)** Circuit model for the Pt/YIG bilayer film. V_{total} is the voltage measured in open circuit conditions across the Pt layer. V_{SSE} is the voltage generated by the SSE, V_H is the voltage generated by the rate of change of the magnetic flux through the circuit loop and R is the electrical resistance of the Pt layer.

The spin current is converted to an electric field, E_{ISHE}, by the ISHE , which is given by the following equation [76, 75]:

$$\boldsymbol{E}_{ISHE} = (\theta_{SH}\rho)\,\boldsymbol{j}_s \times \boldsymbol{\sigma} \tag{59}$$

where θ_{SH} and ρ are the spin Hall angle and the electrical resistivity of the Pt layer respectively, $\boldsymbol{j}_s$ is the spin current density, and $\boldsymbol{\sigma} = \boldsymbol{M}/||\boldsymbol{M}||$ is the spin polarization unit vector, which is parallel to the magnetization $\boldsymbol{M}$ of the YIG layer. According to the SSE theory [108], $\boldsymbol{j}_s$ is parallel to the thermal gradient and proportional to the temperature difference ΔT between the Pt and the YIG layer [208]. The magnetization in the YIG layer is parallel to the external magnetic field, which in our setup is periodic with frequency f $= \omega/2\pi$.

The potential difference (voltage), caused by the ISHE-electric field, can be measured in the Pt layer by the line integration of the electric field along the platinum strip, between two electric contact points. The resulting spin Seebeck voltage is given by [216]:

$$V_{SSE} = |\boldsymbol{E}_{ISHE}| L_{Pt} cos(\theta) \tag{60}$$

where L_{Pt} is the length of Pt layer, and θ is the angle defined in figure 26(b). In our setup the external magnetic field can be oriented in an arbitrary direction, angularly spanning sample plane. Once it is oriented in the desired direction, the magnetic field oscillates harmonically. In this way, the direction of magnetic field can take only the values θ and $\theta + 180°$, and according to equation 59, we obtain a maximum signal at $\theta = 0°$ (or 180°). This angle is achieved by orienting the external magnetic field perpendicularly to the platinum line in the $\pm x$-direction. Then the $\boldsymbol{E}_{ISHE}$ is oriented along the $\pm y-$direction, oscillating harmonically, and $|\boldsymbol{E}_{ISHE}| \propto \Delta T$.

In summary, the spin Seebeck voltage will have the following dependency:

$$V_{SSE} \propto \pm \Delta T L_{Pt} \tag{61}$$

Thereby, when the sample is stimulated by an alternating magnetic field, the thermally induced spin current generates, by ISHE in the Pt, a square wave like voltage of amplitude proportional to ΔT.

The second contribution, given by Faraday's law of induction, is the EMF induced in the sample by the rate of change of the magnetic flux through the circuit loop area (A_{loop}):

$$\mathrm{V_H}(t) = -N \frac{d\Phi(t)}{dt} \tag{62}$$

where $\Phi(t) = \boldsymbol{A}_{loop} \cdot \boldsymbol{H}_{ext}(t)$ is the magnetic flux and $N = 1$ (simple circuit loop). For $\theta = 0°(180°)$, $\boldsymbol{H}_{ext}(t)$ and $\boldsymbol{A}_{loop}$ are parallel (antiparallel), then:

$$\mathrm{V_H}(t) \propto -(+) H_0 \omega \cos(\omega t) \tag{63}$$

In addition to the SSE and the magnetic flux variation, we consider a contribution originated by the background noise V_{Noise}. Thus, according to equations 60 and 63, our measured voltage V_{total} will be:

$$V_{\mathrm{total}}(t) = V_{\mathrm{SSE}}(t) + V_{\mathrm{H}}(t) + V_{Noise} \tag{64}$$

Considering that a linear combination in the time domain becomes a linear combination in the frequency domain, we can express the total voltage as [217]:

$$V_{total}(t) = \sum_{n=-\infty}^{+\infty} |V_{\mathrm{nf}}| \, \mathrm{e}^{in\omega t} \tag{65}$$

$$V_{\mathrm{nf}} = \left(V_{\mathrm{nf,SSE}}^2 + V_{\mathrm{nf,H}}^2 \right)^{1/2} \tag{66}$$

Where $\omega = 2\pi \mathrm{f}$ is the fundamental angular frequency. $V_{\mathrm{nf,SSE}}$ and $V_{\mathrm{nf,H}}$ are the coefficients of the Fourier expansion for $V_{SSE}(t)$ and $V_H(t)$ respectively.

$V_{SSE}(t)$ and $V_H(t)$ are given by

$$V_{SSE}(t) = \sum_{n=-\infty}^{+\infty} V_{\mathrm{nf,SSE}} \, \mathrm{e}^{in\omega t} \tag{67}$$

$$V_H(t) = \sum_{n=-\infty}^{+\infty} V_{\mathrm{nf,H}} \, \mathrm{e}^{in\omega t} \tag{68}$$

and their trigonometric form is:

$$V_{SSE}(t) = \frac{4V_{SSE}}{\pi} \sum_{n=1}^{\infty} \frac{sin(2n+1)\omega t}{2n+1} = \frac{4V_{SSE}}{\pi} \left(\sin(\omega t) + \frac{\sin(3\omega t)}{3} + \frac{\sin(5\omega t)}{5} + ... \right) \tag{69}$$

$$V_H(t) = H_0 \omega \cos(\omega t) + o(2\omega) \tag{70}$$

According to equation 69, the SSE signal is manifested only in the odd harmonics of the fundamental frequency (f, 3f, 5f...). On the other hand, the voltage induced by the magnetic field is mainly manifested in the fundamental frequency (see equation 70). However, due to the harmonic distortion of the power source that supplies the coils and the non-linear response of these, we may have a small contribution in the higher harmonics of $V_H(t)$.

We can experimentally separate the total signal into its harmonic contributions, each of which has one component originating from the SSE effect and the other from the Faraday effect. This experimental technique is explained in the next subsection. In this work, we focus our attention on the first three higher harmonics, since at higher values the signals become smaller, making it increasingly difficult to measure them.

4.2 Principles of Lock-in detection

In SSE experiments the signal investigated are usually small, less than 1 $\mu V/K$, so direct DC measurements are obscured by noise sources, providing a non-satisfactory signal to noise ratio. A lock-in amplification is an experimental method to detect very small modulated and overwhelmed by noise signals. In the following, we give a brief description of this method.

Lock-in detection technique uses the knowledge about a signal's time dependence to extract it from a noisy background [218]. This technique uses a reference signal to modulate the signal of interest. The signal to be measured is multiplied by the reference signal and then integrated over time. This technique is called homodyne detection. Consider a noisy cosinoidal input signal $S(t)$ defined by the following equation:

$$S(t) = V_S \cos(\omega_R t + \phi_s) + \sum_n V_n \cos(\omega_n t + \phi_n) \tag{71}$$

where ω_R is the angular frequency of the modulated signal, which is equal to the frequency of the reference signal $r(t)$ defined in equation 72, ϕ_S is the initial phase angle and V_S is the input signal amplitude. Noise sources contribution are roughly approximate as a sum of n discrete noise sources with different intensities V_n, frequencies ω_n and phases ϕ_n.

$$r(t) = V_R \cos(\omega_R t + \phi_R) \tag{72}$$

The lock-in amplifier multiplies the desired and reference signals using an analog mixer (demodulation process). This multiplied signal is then integrated over a time constant τ (equation 73). The prefactor $1/\tau$ prevents that the integral scale with τ.

$$V_{out} = \frac{1}{\tau} \int_t^{t+\tau} S(t) \times r(t)\, dt \tag{73}$$

or, from the expansion of the sum:

$$V_{out} = \frac{1}{\tau} \int_t^{t+\tau} V_S V_R \cos(\omega_R t + \phi_s) \cos(\omega_R t + \phi_R)\, dt + ... \\ ... \frac{1}{\tau} \sum_n \int_t^{t+\tau} V_n V_R \cos(\omega_n t + \phi_n) \cos(\omega_R t + \phi_R)\, dt \tag{74}$$

Since the two mixed signal have exactly the same frequency, and the time constant is much larger than the period of the desired signal we conclude that: i) the first term in the equation 74 is a dc signal proportional to the amplitude of the input signal V_S and to the cosine of the phase difference between the input and the reference signals, ii) the second term goes to zero, except for a possible noise term having frequency $\omega_m = \omega_R$. Then, after integration the output signal is:

$$V_{out} = \frac{1}{2} V_s V_R \cos(\phi_s - \phi_R) + \frac{1}{2} V_m V_R \cos(\phi_R - \phi_m) \tag{75}$$

However, we can assume that none of the noise sources match the frequency of the reference signal so, the second term in the above equation does not necessarily appear, since the argument of the second integral in equation 74 would always correspond to the product of two orthogonal functions and consequently the integration over many periods vanishes. In a lock-in amplifier the mixed signal passes through a low-pass filter that removes all noises and ac signals with frequency different to the reference, leaving the output of the lock-in amplifier as the required dc signal.

According to equation 75, the main handicap to measure V_S is that the phase shift between measurement and reference signal must be known. In order to reconstruct the amplitude and phase of the measured signal, the demodulation process is performed by using two orthogonal references, this gives two rectified values, that correspond to a in-phase (X) and out-of-phase (Y) components relative to the reference. Therefore, the reference signal to the second demodulation process is $r_{shift}(t) = V_R \cos(\omega_R t + \phi_R - \pi/2) = V_R \sin(\omega_R t + \phi_R)$ and the output signal (after integration or filtering) is given by $V_{shift,out} = (1/2) V_S V_R \sin(\phi_S - \phi_R)$. For simplicity, we consider normalized reference signals, i.e. $V_R = 1$, therefore X and Y components of the measured signal are given by the following equations:

$$X = \frac{1}{2} V_S \cos(\phi_S - \phi_R) \tag{76}$$

$$Y = \frac{1}{2} V_S \sin(\phi_S - \phi_R) \tag{77}$$

Finally, the amplitude an phase of the measured signal can be calculated as:

$$V_S = 2\sqrt{X^2 + Y^2} \tag{78}$$

$$(\phi_S - \phi_R) = \tan^{-1}(Y/X) \tag{79}$$

A block diagram of the lock-in detection algorithm is depicted in figure 28. The system (sample) is driven by a sinusoidal signal ($\boldsymbol{H}_{ext}(t)$). The output signal from the tested system is collected by an acquisition card (DAQ) and averaged over many cycles.

In general, any signal can be completely described by the sum of an infinite number of harmonic components whose frequencies are integer multiples of the fundamental frequency ω_R ($2\omega_R$, $3\omega_R$ and so on). In order to extract the desired harmonic signal, the described lock-in technique can be used, by setting the frequency of the reference signal as an integer multiple of the modulation frequency. Then, the filtered signal given by equation 73 can be rewritten as [209]:

$$V_{n\omega_R}(t) = \frac{1}{\tau}\int_t^{t+\tau} cos(n\omega_R t + \phi_R)S(t)dt \tag{80}$$

where, n is an integer number that indicates the harmonic of interest, ϕ_R is the phase of reference signal that can take the values $\phi_R = 0°$ for the in-phase component ($X_{n\omega_R}$) and $\phi_R = 90°$ for the out-of-phase component ($Y_{n\omega_R}$). These two signals contain the information on the amplitude $V_{n\omega_R}$ of the nth-harmonic component of the measured signal and its phase $\theta_{n\omega_R}$, as we can see in the following equations [219]:

$$V_{n\omega_R} = 2\sqrt{X^2_{n\omega_R} + Y^2_{n\omega_R}} \tag{81}$$

$$\theta_{n\omega_R} = tan^{-1}\left(\frac{Y_{n\omega_R}}{X_{n\omega_R}}\right) \tag{82}$$

Figure 29 shows a block diagram of the electronics used in the experimental setup for SSE measurements. An static thermal gradient is applied through the sample plane and simultaneously an a.c. magnetic field of frequency f is applied transversely. A sine-wave generator is used to modulate the electromagnet power supply and the reference signal is synthesized from the magnetic field measurement. The output signals are collected by a data acquisition card and a digital lock-in amplifier extracts the in-phase ($V_{\text{nf,SSE}} = V_{\text{nf}}\, cos(\theta_{\text{nf}})$, due to SSE) and out-of-phase ($V_{\text{nf,H}} = V_{\text{nf}}\, sin(\theta_{\text{nf}})$, due to Faraday´s law of induction) components of the first (n = 1) , second (n = 2)

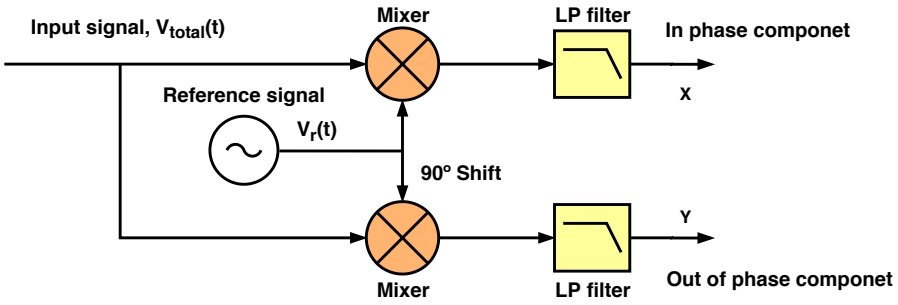

Figure 28. Block diagram of a typical lock-in amplifier. Using a quadrature version of the reference signal (90° shift) we obtain both the in phase and out of phase components. LP stands for Low-Pass (filter).

and third (n = 3) harmonics. To separate the signal from a background noise and achieve greater sensitivity in the detection of the SSE, the measurement is averaged over many cycles (1000 in our experiment).

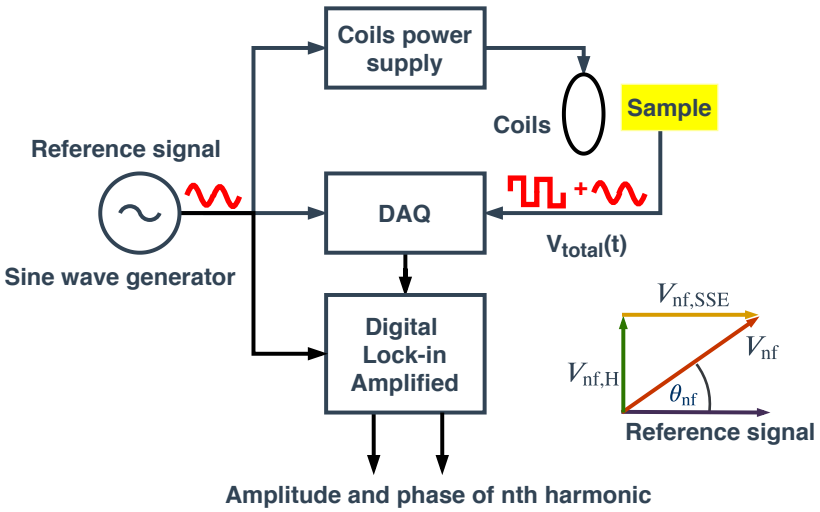

Figure 29. Block diagram of the measurement system. A sine wave function generator provides the reference signal to modulate coils power supply and starts the data acquisition by the DAQ-card. The signal collected is filtered by a digital lock-in. The FFT analysis provides the frequency spectrum for all harmonics of f. The n-harmonic is represented by a phasor of amplitude V_{nf} and a phase angle θ_{nf} respect to the reference signal. $V_{nf,SSE}$ and $V_{nf,H}$ correspond respectively to the in-phase and out-of-phase components of the n-harmonic.

4.3 Temperature measurements

A precise determination of the temperature difference at the Pt/YIG interface sample is extremely difficult. However, we can assume that it must be proportional to the thermal gradient across the sample [208, 108] and, in consequence, to the temperature difference between the thermal reservoirs, which are very close to the sample. The temperature measurement was performed by using two methods. The first method, infrared thermography technique, enables the measurement of ΔT with high temperature resolution (0.1 K) and good spatial resolution or instantaneous field of view (IFOV) of 3.7 $mrad$. In the second method, ΔT was continuously measured by using two thermocouples connected differentially to the thermal reservoirs, achieving a precision of 0.01 K and a standard deviation of 0.04 K. The experimental set-up used in our experiments is shown in figure 30. An infrared image of the device utilized in this work (See the magnified region in figure 30) is shown in figure 31(a).

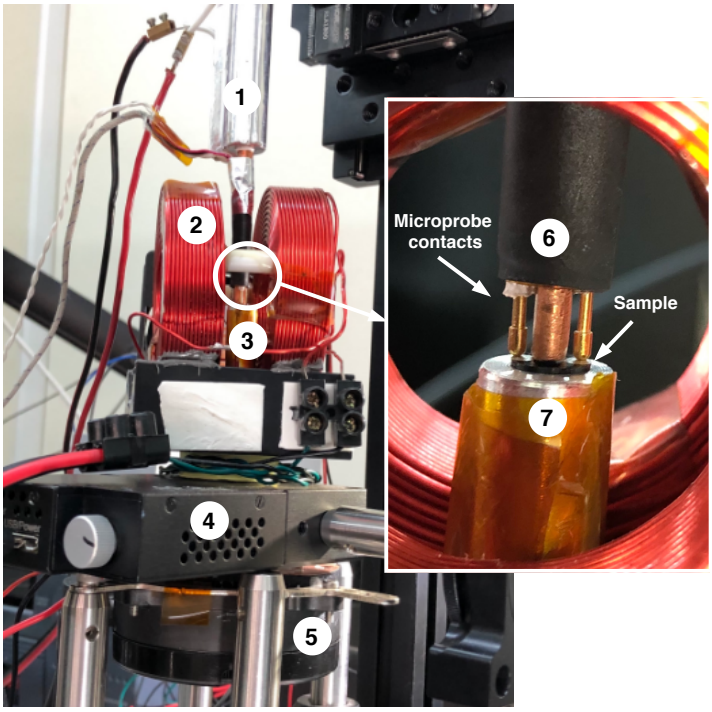

Figure 30. Experimental setup. **1** Hot reservoir, **2** Coils, **3** Cold reservoir, **4** Motorized Rotation Stage, **5** Liquid cooler. In the magnification, **6** and **7** thermocouples (inside the thermal reservoirs), the sample and the electrical contacts to the sample.

The temperature profile along a line between the hot and cold reservoirs is shown in figure 31(b), where a temperature difference of $\Delta T = (28.0 \pm 0.1)\ K$ is obtained. The peaks of the temperature profile, in the transition zone between the cold and the hot reservoirs, can be originated from the kapton tape shielding effect and the convective flow of the air around the heat reservoirs. During the measurement, the temperature difference was also continuously monitored by two thermocouples internally connected to the thermal reservoirs and very close to the sample, obtaining a value of $\Delta T = (27.45 \pm 0.04)\ K$. The quantitative comparison of these two measurement systems provides an excellent agreement in the obtained temperature difference.

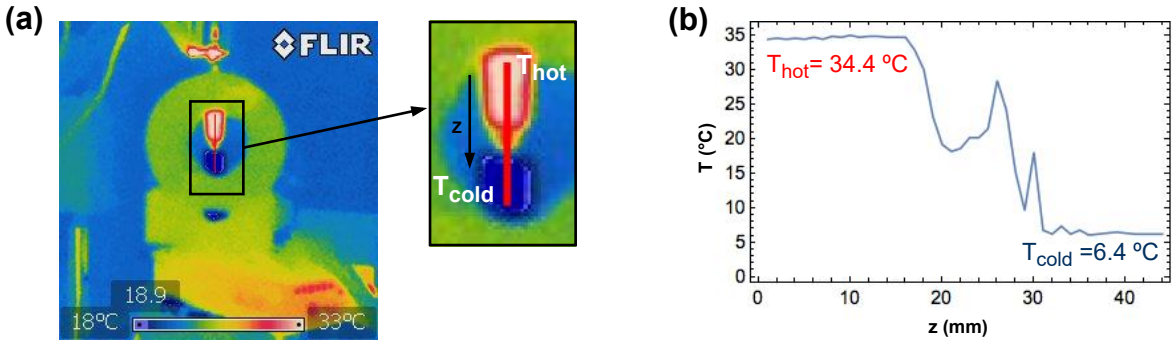

Figure 31. **(a)** Thermal image of the device when a temperature gradient is established. In the magnified region, we show the hot reservoir (upper), sample (middle), and cold reservoir (bottom). The temperature profile is determined along the red line. **(b)** Temperature profile. The temperature difference between the hot and cold reservoirs is $\Delta T = 28.0$ K.

4.4 SSE experiment Results

To confirm the presence of a square wave signal in the total voltage, we obtained the frequency domain spectrum for various temperature differences. Figure 32 shows the spectrum of a signal measured under the application of an external magnetic field of frequency f = 8 Hz. We observe a clear predominance of the odd harmonics (8, 24, 40, 56, and 72 Hz) when ΔT increases, which confirms our assumptions. For $\Delta T = 0\ K$, the response observed in the third harmonic can be attributed to the thermal fluctuations caused by the coils.

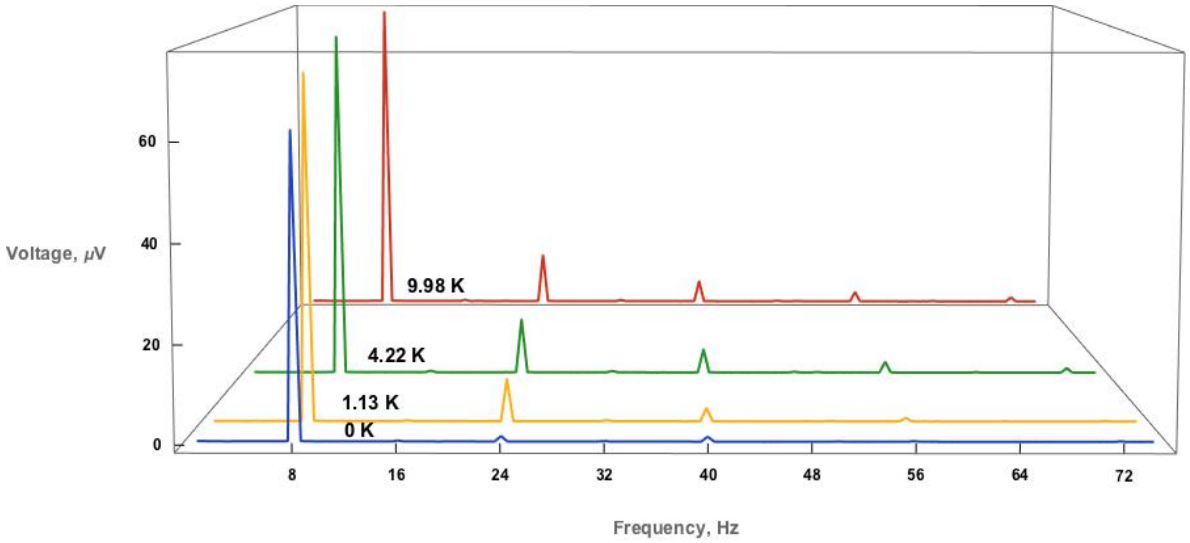

Figure 32. V_{total} in the frequency domain for four temperature differences ΔT. For ΔT from 0 K to 9.89 K. Each of the peaks in the spectrum corresponds to odd harmonics of fundamental frequency f = 8 Hz. For $\Delta T = 0\ K$ only the fundamental frequency is significantly manifested.

Regarding the contribution of each harmonic to the $V_{SSE}(t)$ signal, and according to equation 69, the amplitude of the first harmonic should be three times greater than the amplitude of the third harmonic. However, this proportion does not consider the contribution of other thermoelectric or magnetoresistive effects, which are manifested in the first and second harmonic. Figure 33 shows a ΔT - dependence of the in-phase component of the first three harmonics. In addition, a linear fit of the first and third harmonics are shown. The compared slopes of the linear fits ($S_{\mathrm{f,SSE}}/S_{\mathrm{3f,SSE}}$) reveals

that the amplitude of the $V_{\mathrm{f,IP}}$ increases 2.3 ± 0.1 times faster than the $V_{\mathrm{3f,IP}}$, this is 23% lower than the harmonics of a pure SSE signal.

This result is consistent with our initial assumption that the first harmonic includes contributions other than SSE. The observed difference between the observed signal and the corresponding to a pure SSE signal maybe attributed to the contribution of other thermoelectric and magnetoresistive effects with specific signal characteristics (magnitude and phase). The analysis of these contributions goes beyond the focus of this work.

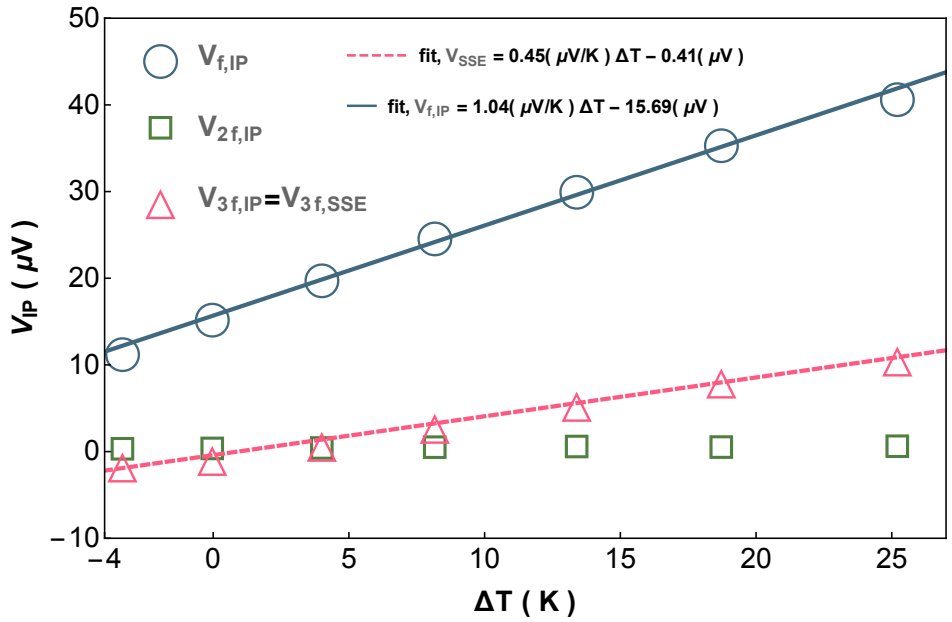

Figure 33. In-phase component of the first, second and third harmonic of the total signal as a function of ΔT. The solid and dashed line corresponds to a linear fit of the first and third harmonic respectively. The slope of the linear fit corresponds to the spin Seebeck coefficient of each odd harmonic. For the first harmonic we have $S_{\mathrm{f,IP}} = (1.04 \pm 0.03)\ \mu V/K$, while for the third harmonic we obtain $S_{\mathrm{3f,SSE}} = (0.45 \pm 0.01)\ \mu V/K$.

Figure 34(a) shows the amplitude of the three first harmonics as a function of ΔT. The signal was measured in a magnetic field with an amplitude 170 Oe and frequency 8 Hz, aligned in the $\theta = 0°$ direction. The out-of-phase and in-phase components extracted from the first, second and third harmonics are depicted as a

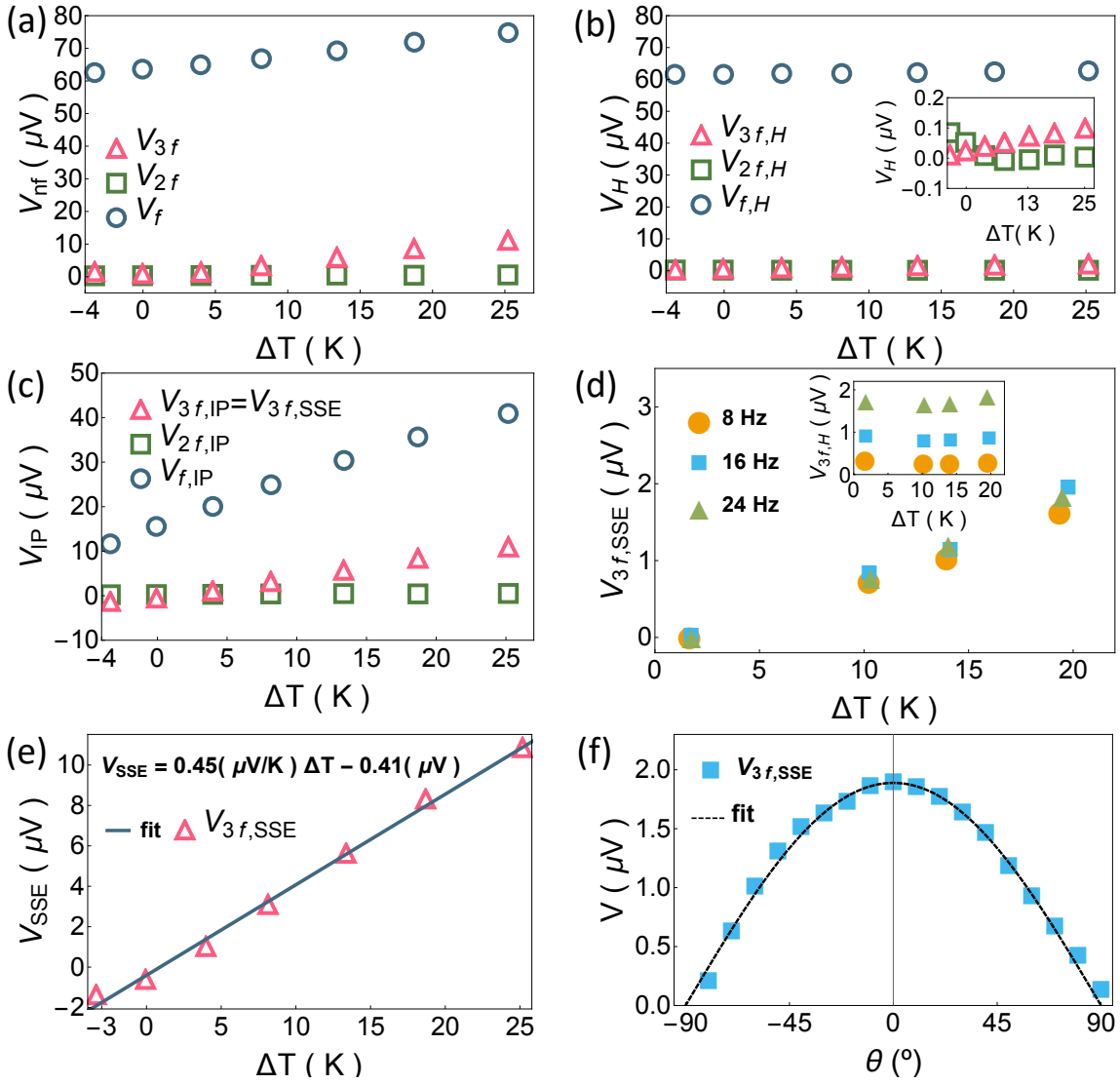

Figure 34. Principal results of SSE measurement obtained by harmonic analysis. **(a)** Amplitude of the first three harmonics of the total signal, measured as a function of ΔT for an applied magnetic field of 170 Oe and 8 Hz. From these voltages, we have extracted their out-of-phase and in-phase components, shown in **(b)** and **(c)**, respectively. The inset in **(b)** shows the out-of-phase component of the second and third harmonics on an adequate scale. **(d)** Third harmonic in-phase component ($V_{3f,SSE}$) measured for three different frequencies of the magnetic field: 8 Hz (orange circle), 16 Hz (blue square) and 24 Hz (green triangle), measured for an applied magnetic field of 175 Oe. The inset is the out-of-phase component (V_H). **(e)** Ampliation and linear fit (dashed line) of the $V_{3f,IP}$ voltage from the plot **(c)**. **(f)** θ dependence of the 3f−harmonic in-phase component measured at $\Delta T = 17\ K$ and magnetic field of 167 Oe. The dashed line is a $\cos(\theta)$ fit.

function of ΔT in figures 34(b) and 34(c), respectively. The out-of-phase component remains essentially constant as ΔT increases and is proportional to the magnetic field frequency, as expected according to the equation 70 and as shown in the inset of figure 34(d).

The inset in figure 34(b) shows $V_{2f,H}$ and $V_{3f,H}$ on an appropriate scale because their amplitudes are much smaller than the amplitude of the first harmonic. In contrast, the amplitude of the in-phase components clearly shows an increase as ΔT increases, and we can even see that $V_{3f,IP}$ becomes negative when ΔT is reversed. This result indicates that the $V_{3f,IP}$ signal is originated by the SSE. A linear fit of $V_{3f,IP}$ (hereinafter referred to as $V_{3f,SSE}$) is shown in figure 34(e). The slope of the linear fit corresponds to the spin Seebeck coefficient [220, 221] or SSE thermopower, which is given by $S_{3f,SSE} = V_{3f,SSE}/\Delta T$ [222, 223]. The SSE coefficient corresponds to a normalized voltage measured with respect to the temperature difference through the FM/NM sample, allowing the comparison of our results to other measurements in similar systems. However, there are other expressions that can be used for this purpose; for example, normalizing the SSE voltage with respect to the temperature difference and the separation between electrical contacts, normalizing the SSE electric field with respect to the thermal gradient [222] and normalizing the SSE voltage with respect to heat flux [224]. From this, we can estimate the total spin Seebeck coefficient ($S_{SSE} = \Delta V_{SSE}/\Delta T$), in effect equation, 69 (Fourier expansion of a square signal) shows that the amplitude of the third harmonic is proportional to the amplitude of the total signal $V_{3f,SSE} = 4V_{SSE}/(3\pi)$ so, we can estimate that $S_{SSE} = 3\pi V_{3f,SSE}/(4\Delta T)$. The obtained value, $S_{SSE} = 1.1\ \mu V/K$, agrees with the values reported in the literature [220, 223, 224].

To compare our method with standard techniques [225] used in the study of the SSE, we performed the SSE measurement based on the detection of V_{SSE} as a function of the amplitude and direction of an external magnetic field (i.e. magnetization in YIG) and amplitude and direction of the thermal gradient across the sample. Due to the typically small values of V_{SSE}, this voltage was measured by a Keithley nanovoltmeter model 2182A while the thermal gradient was established by two Peltier cells. The results of these measurements are shown in figure 35. We can clearly observe that

the observed voltage sign changes when the magnetic field and the thermal gradient reverse their direction, which demonstrates the thermal and magnetic origin of the observed signal. This behavior is in agreement with equations 59 and 60, that shows us that the induced electric field reverses its direction by reversing the direction of the applied magnetic field, and on the other hand the magnitude of the observed SSE voltage is proportional to the temperature difference, as shown in equation 61. The inset in figure 35 shows V_{SSE} as a linear function of ΔT. This behavior of V_{SSE} evidences the temperature-gradient origin of the measured signal, in other words, spin Seebeck effect.

To compare our result with the obtained by conventional SSE detection techniques, we used the sample to determine the spin Seebeck coefficient in a static magnetic field and static thermal gradient. We calculated S_{SSE} from the fitted slope of V_{SSE} versus ΔT shown in the insert of figure 35. The obtained result $S_{SSE} = 0{,}92\ \mu\mathrm{V/K}$ is comparable to those in the literature [220, 223, 224] and about 16% less than the one obtained with our methodology, $S_{SSE} = 1.1\ \mu\mathrm{V/K}$.

In the temperature range considered in this work, the resistance of the platinum layer increases linearly with increasing temperature, around 3% with respect to the value measured at room temperature ($R_{Pt} = 135\,\Omega$), which agrees with previous studies [226]. This residual increase in the resistance will induce a marginal variation of both the out-of-phase and in-phase voltage.

In figure 35 an interesting behavior can be observed in the low-magnetic-field range (under $300\,Oe$), it can be seen that the longitudinal SSE signal has a slow increase, producing a break in the expected behaviour. Uchida *et al.*[103] propose that when the magnetic saturation of the sample is not yet reached, the thermally excited magnons are scattered by the magnetic domain walls that have not yet aligned with the external magnetic field.

It has been recently shown that a YIG/Pt system subjected to a periodic thermal gradient with frequencies from 10 MHz to 1 GHz, generates a frequency dependent SSE signal at microwave frequency [227, 228]. On the other hand, we have that the YIG spin-lattice relaxation time [229] is much less than the variation of the magnetic field in our setup. Hence, the spin current generation and electric current conversion

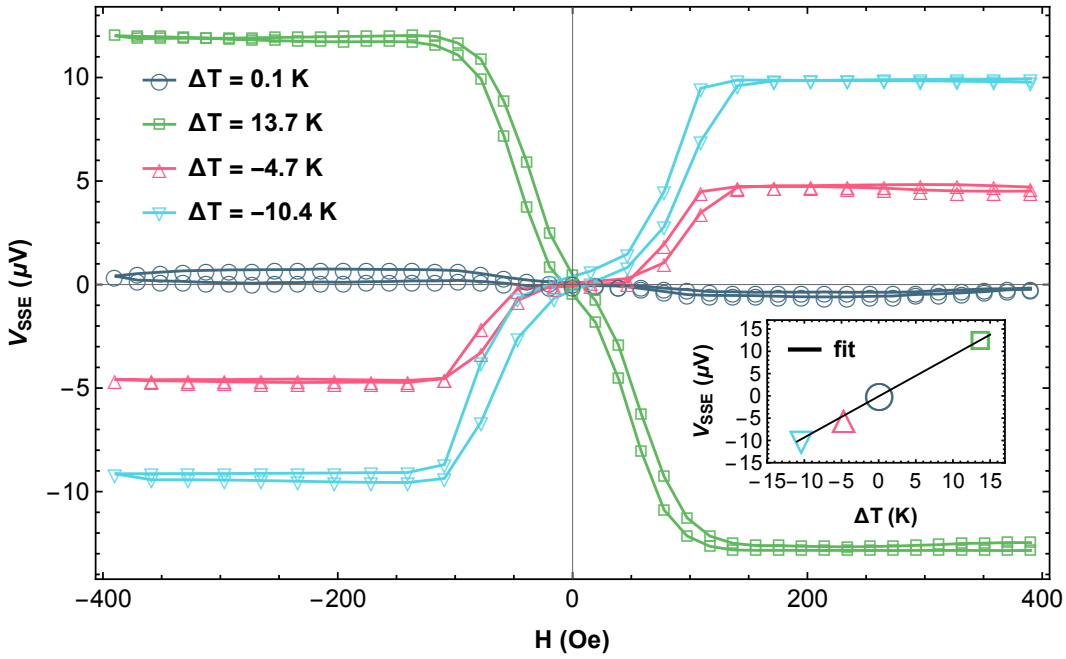

Figure 35. Hysteresis loops of V_{SSE} for different ΔT. When the direction of the temperature difference is inverted, the sign of V_{SSE} is also reversed. These curves were obtained through the standard methodology developed in previous works on spin Seebeck effect that is, static magnetic field and static thermal gradient. The inset shows the linear response of V_{SSE} respect to ΔT. The solid line is linear fits.

are in a quasi-static regime [108]. In consequence, the SSE signal should not depend on the magnetic field frequency, in agreement with equation 61 . To confirm this point, we have measured the temperature dependency of the SSE signal for three different frequencies; 8 Hz, 16 Hz and 24 Hz, and for temperature differences between 1 K to 26 K. In each measurement, the magnetic field amplitude was maintained constant at $H_{ext} = 170$ Oe. Results presented in figure 34(d) corroborates this hypothesis and also show that the in-phase component of the voltage, corresponding to the SSE, exhibits a linear dependence with the temperature gradient, in agreement with equation 60. The inset shows, for each considered frequency, that the out-of-phase component signal remains essentially constant respect to the temperature, and their amplitude are correlated with the frequency of the external magnetic field. This behavior agrees with equation 63, confirming the SSE origin of the out-of-phase signal

component in an a.c. magnetic field.

To confirm the SSE origin of the third harmonic signal[100], we show in figure 34(f) how the SSE-voltage $V_{3f,SSE}$ exhibits a $cos(\theta)$-dependence, which is in agreement with equation 60. The measurement was performed at constant $\Delta T = 17$ K, and for a magnetic field that varies its orientation in the range $\pm$ 90°.

Our results present an alternative methodology to detect the SSE in a YIG/Pt system using an alternating magnetic field at a constant thermal gradient. The platinum strip is used exclusively as a spin-current detector, reducing the impact of contributions originated from other thermoelectric effects. By minimizing the number of electrical contact points in the sample, we reduce the presence of electrical drift. In this approach, the SSE signal is manifested by an increase of the amplitude and phase of the odd harmonics of the fundamental frequency of the alternating magnetic field. The use of lock-in detection techniques and the corresponding harmonic analysis permits the detection and measurement of the third harmonic signal, originated exclusively by the SSE, removing undesired contributions coming from the conventional charge transport, thermoelectric effects and background noise. Taking into account that this technique requires the alignment of the magnetization with the external magnetic field, it is particularly recommended for soft magnetic materials, which are widely used for spincaloritronic applications.

Chapter 5
Summary & outlook

The research presented in this thesis mostly focused in two main fields: material science and spincaloritronics.

The aim of the work developed in the material science topic was the growth and the characterization of magnetic insulator yttrium iron garnet (YIG) in thin film form. YIG is the most common material in magnonics research, offering uniquely low magnetic damping and isotropic magnetic properties. Its relevance in the study of magnetic oxides and magnetism is so great that it the noted physicist Charles Kittel called the "*frut fly*" of magnetism, alluding to the role of this insect in genetics research [230]. We have fabricated YIG thin films on GGG substrate by using pulsed laser deposition technique under optimized growth condition, in order to focus our attention in their structural and magnetic properties. The XRD and XRR characterization of the growth of YIG thin films show an excellent crystalline quality, evident with clear Laue oscillations. The magnetic properties are investigated by ferromagnetic resonance between 3 and 17 GHz. The information obtained from FMR analysis evidences good magnetic properties. The measured Gilbert damping constant is extremely low, comparable to the best values reported for YIG thin films. However, characterization of some films show was observed to exhibit a strong extrinsic contribution to the ferromagnetic resonance relaxation rate and linewidth coming from the two magnon scattering process, caused by defects and impurities. We measured an increase in the value of $4\pi M_s$, which has been attributed to the strong uniaxial anisotropy caused by Fe^{3+} vacancies within octahedral sites, off-stoichiometry and ionic diffusion processes of Ga and Gd from the substrate.

Two magnon scattering relaxation processes is usually ignored in the determination of magnetic properties, however, this phenomenon can be used to manipulate and control magnetic relaxation processes and magnetic anisotropy with very interesting modern technological applications in spintronics, spin caloritronics, and topotronics (topological electronics [231]) devices. Hence, a better understanding of

magnetic relaxation physics aids development of high performance and low-power consumption spintronic devices [232].

In the spincaloritronics topic, we have presented an alternative technique to detect and measure the spin Seebeck effect in a YIG/Pt system, a standard system for studying the SSE. In the presented tool, the SSE signal is modulated by an oscillating magnetic field, while the thermal gradient, provided by an external heat reservoir, remains constant. The novel setup enable the in-plane rotation of oscillating magnetic field by the utilization of a motorized rotation stage. This enables the application of magnetic field at varied in-plane angles without the need of reassembling the sample or the electric contacts. In this technique a platinum strip is used exclusively as a spin current detector, reducing the impact of contributions originated from other thermoelectric effects. By minimizing the number of electrical contact points in the sample, we reduce the presence of electrical drift. In this approach the SSE signal is manifested by an increase in the amplitude and phase of the odd harmonics of the fundamental frequency of the oscillating magnetic field. The use of a digital lock-in detection technique and the corresponding harmonic analysis permits the detection and measurement of a third harmonic signal, originated exclusively from the SSE, removing undesired contributions coming from the conventional charge transport, thermoelectric effects, and background noise. Taking into account that this technique requires the fast alignment of the magnetization with the external magnetic field, it is particularly recommended for soft magnetic materials, which are widely used for spincaloritronic applications.

Spin-caloritronics is a relatively new research field focused on the interaction of electron spin and heat current. The magnonic spin Seebeck effect is a key element of this investigation area, which enables the efficient generation of pure spin currents driven by thermal gradients and opening the door to many new technological applications: temperature sensors, power generators that convert waste heat into electricity. In this line, the research in material science aimed in the search of new materials that enable a more efficient spin current and charge current generation is an important challenge.

References

1. Ling Bing Kong, H. H. H. F. B. T. Z. S. L. a., Tao Li. *Waste Energy Harvesting: Mechanical and Thermal Energies*. Lecture Notes in Energy 24 (Springer-Verlag Berlin Heidelberg, 2014), 1 edn.

2. Livermore Lawrence National Laboratory and Department of Energy. Estimated Chile Energy Consumption in 2011. (2022). at. https://flowcharts.llnl.gov/sites/flowcharts/files/ENERGY_2011_CHILE.png.

3. Forman, C., Muritala, I. K., Pardemann, R. & Meyer, B. Estimating the global waste heat potential. *Renew. Sustain. Energy Rev.* **57**, 1568–1579, DOI: https://doi.org/10.1016/j.rser.2015.12.192 (2016).

4. Bian, Q. Waste heat: the dominating root cause of current global warming. *Environ. Syst. Res.* **9**, 8, DOI: 10.1186/s40068-020-00169-2 (2020).

5. Heremans, J. P., Dresselhaus, M. S., Bell, L. E. & Morelli, D. T. When thermoelectrics reached the nanoscale. *Nat. Nanotechnol.* **8**, 471–473, DOI: 10.1038/nnano.2013.129 (2013).

6. Zevenhoven, R. & Beyene, A. The relative contribution of waste heat from power plants to global warming. *Energy* **36**, 3754–3762, DOI: https://doi.org/10.1016/j.energy.2010.10.010 (2011). ECOS 2009.

7. Moore, G. E. Cramming more components onto integrated circuits, reprinted from electronics, volume 38, number 8, april 19, 1965, pp.114 ff. *IEEE Solid-State Circuits Soc. Newsl.* **11**, 33–35, DOI: 10.1109/N-SSC.2006.4785860 (2006).

8. Ullmann, B. & Grasser, T. Transformation: nanotechnology—challenges in transistor design and future technologies. *e & i Elektrotechnik und Informationstechnik* **134**, 349–354, DOI: 10.1007/s00502-017-0534-y (2017).

9. Johnson, D. Ibm introduces the world's first 2-nm node chip (2021). IEEE Spectrum, https://spectrum.ieee.org/nanoclast/semiconductors/nanotechnology/ibm-introduces-the-worlds-first-2nm-node-chip.

10. Markov, I. L. Limits on fundamental limits to computation. *Nature* **512**, 147–154, DOI: 10.1038/nature13570 (2014).

11. Wu, J., Shen, Y.-L., Reinhardt, K., Szu, H. & Dong, B. A nanotechnology enhancement to moore's law. *Appl. Comput. Intell. Soft Comput.* **2013**, 426962, DOI: 10.1155/2013/426962 (2013).

12. Bader, S. & Parkin, S. Spintronics. *Annu. Rev. Condens. Matter Phys.* **1**, 71–88, DOI: 10.1146/annurev-conmatphys-070909-104123 (2010). https://doi.org/10.1146/annurev-conmatphys-070909-104123.

13. Feynman, R. There's plenty of room at the bottom, engineering and science. *California: California Inst. Of Technol.* (1960). https://resolver.caltech.edu/CaltechES:23.5.0.

14. Powell, J. R. The quantum limit to moore's law. *Proc. IEEE* **96**, 1247–1248, DOI: 10.1109/JPROC.2008.925411 (2008).

15. Snyder, G. J. & Toberer, E. S. Complex thermoelectric materials. *Nat. Mater.* **7**, 105–114, DOI: 10.1038/nmat2090 (2008).

16. Wang, X. *et al.* Direct thermal charging cell for converting low-grade heat to electricity. *Nat. Commun.* **10**, 4151, DOI: 10.1038/s41467-019-12144-2 (2019).

17. Gur, I., Sawyer, K. & Prasher, R. Searching for a better thermal battery. *Science* **335**, 1454–1455, DOI: 10.1126/science.1218761 (2012).

18. Pandya, S. *et al.* New approach to waste-heat energy harvesting: pyroelectric energy conversion. *NPG Asia Mater.* **11**, 26, DOI: 10.1038/s41427-019-0125-y (2019).

19. Vining, C. B. An inconvenient truth about thermoelectrics. *Nat. Mater.* **8**, 83–85, DOI: 10.1038/nmat2361 (2009).

20. Bauer, G. E. W., Saitoh, E. & van Wees, B. J. Spin caloritronics. *Nat. Mater.* **11**, 391–399, DOI: 10.1038/nmat3301 (2012).

21. Yu, H., Brechet, S. D. & Ansermet, J.-P. Spin caloritronics, origin and outlook. *Phys. Lett. A* **381**, 825–837, DOI: https://doi.org/10.1016/j.physleta.2016.12.038 (2017).

22. UCHIDA, K.-I. Transport phenomena in spin caloritronics. *Proc. Jpn. Acad. Ser. B* **97**, 69–88, DOI: 10.2183/pjab.97.004 (2021).

23. Jaworski, C. M., Myers, R. C., Johnston-Halperin, E. & Heremans, J. P. Giant spin seebeck effect in a non-magnetic material. *Nature* **487**, 210–213, DOI: 10.1038/nature11221 (2012).

24. Benenti, G., Casati, G., Saito, K. & Whitney, R. Fundamental aspects of steady-state conversion of heat to work at the nanoscale. *Phys. Reports* **694**, 1–124, DOI: https://doi.org/10.1016/j.physrep.2017.05.008 (2017). Fundamental aspects of steady-state conversion of heat to work at the nanoscale.

25. Gholami, Z. & Khoeini, F. Pure thermal spin current and perfect spin-filtering with negative differential thermoelectric resistance induced by proximity effect in graphene/silicene junctions. *Sci. Reports* **11**, 104, DOI: 10.1038/s41598-020-80616-3 (2021).

26. Yadav, A., Deshmukh, P., Roberts, K., Jisrawi, N. & Valluri, S. An analytic study of the wiedemann–franz law and the thermoelectric figure of merit. *J. Phys. Commun.* **3**, 105001, DOI: 10.1088/2399-6528/ab444a (2019).

27. Uchida, K.-i. *et al.* Thermoelectric generation based on spin seebeck effects. *Proc. IEEE* **104**, 1946–1973, DOI: 10.1109/JPROC.2016.2535167 (2016).

28. Tan, G., Ohta, M. & Kanatzidis, M. G. Thermoelectric power generation: from new materials to devices. *Philos. Transactions Royal Soc. A: Math. Phys. Eng. Sci.* **377**, 20180450, DOI: 10.1098/rsta.2018.0450 (2019).

29. Kim, M. Y., Park, S. J., Kim, G.-Y., Choi, S.-Y. & Jin, H. Designing efficient spin seebeck-based thermoelectric devices via simultaneous optimization of bulk and interface properties. *Energy Environ. Sci.* **14**, 3480–3491, DOI: 10.1039/D1EE00667C (2021).

30. Kajiwara, Y. *et al.* Transmission of electrical signals by spin-wave interconversion in a magnetic insulator. *Nature* **464**, 262—266, DOI: 10.1038/nature08876 (2010).

31. Kamra, A. *et al.* Spin hall noise. *Phys. Rev. B* **90**, 214419, DOI: 10.1103/PhysRevB.90.214419 (2014).

32. Cornelissen, L. J., Liu, J., Duine, R. A., Youssef, J. B. & van Wees, B. J. Long-distance transport of magnon spin information in a magnetic insulator at room temperature. *Nat. Phys.* **11**, 1022–1026, DOI: 10.1038/nphys3465 (2015).

33. Wesenberg, D., Liu, T., Balzar, D., Wu, M. & Zink, B. L. Long-distance spin transport in a disordered magnetic insulator. *Nat. Phys.* **13**, 987–993, DOI: 10.1038/nphys4175 (2017).

34. Anil Prabhakar, D. D. S. a. *Spin waves: theory and applications* (Springer US, 2009), 1 edn.

35. Dionne, G. F. *Magnetic Oxides* (Springer US, 2009).

36. Oitmaa, J. & Falk, T. Ferrimagnetism in the rare-earth iron garnets: a monte carlo study. *J. Physics: Condens. Matter* **21**, 124212, DOI: 10.1088/0953-8984/21/12/124212 (2009).

37. Helmut Kronmüller, S. P. *Handbook of magnetism and advanced magnetic materials* (Wiley-Interscience, 2007), 1 edn.

38. Ohanian, H. C. What is spin? *Am. J. Phys.* **54**, 500–505, DOI: 10.1119/1.14580 (1986). https://doi.org/10.1119/1.14580.

39. Pauli, W. Über den Zusammenhang des Abschlusses der Elektronengruppen im Atom mit der Komplexstruktur der Spektren. *Zeitschrift fur Physik* **31**, 765–783, DOI: 10.1007/BF02980631 (1925).

40. Giulini, D. Electron spin or "classically non-describable two-valuedness". *Stud. Hist. Philos. Sci. Part B: Stud. Hist. Philos. Mod. Phys.* **39**, 557–578, DOI: https://doi.org/10.1016/j.shpsb.2008.03.005 (2008).

41. Baibich, M. N. *et al.* Giant magnetoresistance of (001)fe/(001)cr magnetic superlattices. *Phys. Rev. Lett.* **61**, 2472–2475, DOI: 10.1103/PhysRevLett.61.2472 (1988).

42. Binasch, G., Grünberg, P., Saurenbach, F. & Zinn, W. Enhanced magnetoresistance in layered magnetic structures with antiferromagnetic interlayer exchange. *Phys. Rev. B* **39**, 4828–4830, DOI: 10.1103/PhysRevB.39.4828 (1989).

43. Wolf, S. A., Chtchelkanova, A. Y. & Treger, D. M. Spintronics—a retrospective and perspective. *IBM J. Res. Dev.* **50**, 101–110, DOI: 10.1147/rd.501.0101 (2006).

44. Jackson, J. D. *Classical electrodynamics* (Wiley, New York, NY, 1999), 3rd ed. edn.

45. Cohen-Tannoudji, C., Diu, ., Bernard & Laloe, F. *Quantum mechanics / Claude Cohen-Tannoudji, Bernard Diu, Franck Laloe ; translated from the French by Susan Reid Hemley, Nicole Ostrowsky, Dan Ostrowsky* (Wiley New York, 1977).

46. Maekawa, S., Valenzuela, S., Saitoh, E. & Kimura, T. *Spin Current* (Oxford University Press, United Kingdom, 2017).

47. Mott, N. F. & Fowler, R. H. The electrical conductivity of transition metals. *Proc. Royal Soc. London. Ser. A - Math. Phys. Sci.* **153**, 699–717, DOI: 10.1098/rspa.1936.0031 (1936). https://royalsocietypublishing.org/doi/pdf/10.1098/rspa.1936.0031.

48. Coey, J. M. D. *Magnetism and Magnetic Materials* (Cambridge University Press, 2010).

49. Das Sarma, S., Fabian, J., Hu, X. & Zutic, I. Issues, concepts, and challenges in spintronics. In *58th DRC. Device Research Conference. Conference Digest (Cat. No.00TH8526)*, 95–98, DOI: 10.1109/DRC.2000.877105 (2000).

50. Sugimoto, N. & Nagaosa, N. Spin-orbit echo. *Science* **336**, 1413–1416, DOI: 10.1126/science.1217346 (2012). https://www.science.org/doi/pdf/10.1126/science.1217346.

51. Linder, J., Yokoyama, T. & Sudbø, A. Pure spin current generated by reflection at a normal metal/two-dimensional electron gas interface. *Phys. Rev. B* **81**, 075312, DOI: 10.1103/PhysRevB.81.075312 (2010).

52. Chumak, A. V., Vasyuchka, V. I., Serga, A. A. & Hillebrands, B. Magnon spintronics. *Nat. Phys.* **11**, 453–461, DOI: 10.1038/nphys3347 (2015).

53. Bloch, F. Zur theorie des ferromagnetismus. *Zeitschrift für Physik* **61**, 206–219, DOI: 10.1007/bf01339661 (1930).

54. Auerbach, A. *Interacting Electrons and Quantum Magnetism* (Springer New York, 1994).

55. Kittel, C. *Introduction to Solid State Physics* (Wiley, 2004), 8 edn.

56. Aharoni, A. *Introduction to the Theory of Ferromagnetism (International Series of Monographs on Physics)*. International Series of Monographs on Physics (Oxford University Press, 2001), 2nd edn.

57. Pires, A. S. T. *Theoretical Tools for Spin Models in Magnetic Systems*. 2053-2563 (IOP Publishing, 2021).

58. Dieterle, G. *et al.* Coherent excitation of heterosymmetric spin waves with ultrashort wavelengths. *Phys. Rev. Lett.* **122**, 117202, DOI: 10.1103/PhysRevLett.122.117202 (2019).

59. Chumak, A. V., Serga, A. A. & Hillebrands, B. Magnonic crystals for data processing. *J. Phys. D: Appl. Phys.* **50**, 244001, DOI: 10.1088/1361-6463/aa6a65 (2017).

60. Stancil, D. & Prabhakar, A. *Spin Waves: Theory and Applications* (2009).

61. Gurevich, A. & Melkov, G. *Magnetization Oscillations and Waves* (Taylor & Francis, 1996).

62. Cornelissen, L. J., Peters, K. J. H., Bauer, G. E. W., Duine, R. A. & van Wees, B. J. Magnon spin transport driven by the magnon chemical potential in a magnetic insulator. *Phys. Rev. B* **94**, 014412, DOI: 10.1103/PhysRevB.94.014412 (2016).

63. Goennenwein, S. T. B. *et al.* Non-local magnetoresistance in yig/pt nanostructures. *Appl. Phys. Lett.* **107**, 172405, DOI: 10.1063/1.4935074 (2015). https://doi.org/10.1063/1.4935074.

64. Giles, B. L., Yang, Z., Jamison, J. S. & Myers, R. C. Long-range pure magnon spin diffusion observed in a nonlocal spin-seebeck geometry. *Phys. Rev. B* **92**, 224415, DOI: 10.1103/PhysRevB.92.224415 (2015).

65. Zhang, S. S.-L. & Zhang, S. Magnon mediated electric current drag across a ferromagnetic insulator layer. *Phys. Rev. Lett.* **109**, 096603, DOI: 10.1103/PhysRevLett.109.096603 (2012).

66. Pottier, N. *Physique statistique hors d'équilibre* (EDP Sciences, 2021).

67. Olsson, K. S. *et al.* Pure spin current and magnon chemical potential in a nonequilibrium magnetic insulator. *Phys. Rev. X* **10**, 021029, DOI: 10.1103/PhysRevX.10.021029 (2020).

68. Rezende, S. M., Azevedo, A. & Rodríguez-Suárez, R. L. Magnon diffusion theory for the spin seebeck effect in ferromagnetic and antiferromagnetic insulators. *J. Phys. D: Appl. Phys.* **51**, 174004, DOI: 10.1088/1361-6463/aab5f8 (2018).

69. Streib, S., Vidal-Silva, N., Shen, K. & Bauer, G. E. W. Magnon-phonon interactions in magnetic insulators. *Phys. Rev. B* **99**, 184442, DOI: 10.1103/PhysRevB.99.184442 (2019).

70. D'Yakonov, M. I. & Perel', V. I. Possibility of Orienting Electron Spins with Current. *ZhETF Pisma Redaktsiiu* **13**, 657 (1971).

71. Kato, Y. K. Observation of the spin hall effect in semiconductors. *Science* **306**, 1910–1913, DOI: 10.1126/science.1105514 (2004).

72. Awschalom, D. & Samarth, N. Spintronics without magnetism. *Physics* **2**, DOI: 10.1103/physics.2.50 (2009).

73. Seifert, J. A review of the magnus effect in aeronautics. *Prog. Aerosp. Sci.* **55**, 17–45, DOI: https://doi.org/10.1016/j.paerosci.2012.07.001 (2012).

74. Manchon, A. A new moment for berry. *Nat. Phys.* **10**, 340–341, DOI: 10.1038/nphys2957 (2014).

75. Saitoh, E., Ueda, M., Miyajima, H. & Tatara, G. Conversion of spin current into charge current at room temperature: Inverse spin-hall effect. *Appl. Phys. Lett.* **88**, 182509, DOI: 10.1063/1.2199473 (2006). https://doi.org/10.1063/1.2199473.

76. Ando, K. *et al.* Inverse spin-hall effect induced by spin pumping in metallic system. *J. Appl. Phys.* **109**, 103913, DOI: 10.1063/1.3587173 (2011). https://doi.org/10.1063/1.3587173.

77. Chazalviel, J. N. & Solomon, I. Experimental evidence of the anomalous hall effect in a nonmagnetic semiconductor. *Phys. Rev. Lett.* **29**, 1676–1679, DOI: 10.1103/PhysRevLett.29.1676 (1972).

78. Bakun, A. A., Zakharchenya, B. P., Rogachev, A., Tkachuk, M. N. & Fleĭsher, V. G. Observation of a surface photocurrent caused by optical orientation of electrons in a semiconductor. *Jetp Lett.* **40**, 1293 (1984).

79. Engel, H.-A., Halperin, B. I. & Rashba, E. I. Theory of spin hall conductivity in n-doped gaas. *Phys. Rev. Lett.* **95**, 166605, DOI: 10.1103/PhysRevLett.95.166605 (2005).

80. Victor, B. M. Quantal phase factors accompanying adiabatic changes. *Proc. R. Soc. Lond. A* **392**, 45–57, DOI: http://doi.org/10.1098/rspa.1984.0023 (1984).

81. Murakami, S. *Intrinsic Spin Hall Effect*, 197–209 (Springer Berlin Heidelberg, Berlin, Heidelberg, 2006).

82. Hoffmann, A. & Bader, S. D. Opportunities at the frontiers of spintronics. *Phys. Rev. Appl.* **4**, 047001, DOI: 10.1103/PhysRevApplied.4.047001 (2015).

83. Saitoh, K., Eiji; Sato. *Spintronics for next generation innovative devices*. Wiley series in materials for electronic and optoelectronic applications (John Wiley Sons Inc, 2015).

84. Takahashi, S. & Maekawa, S. Spin current, spin accumulation and spin hall effect. *Sci. Technol. Adv. Mater.* **9**, 014105, DOI: 10.1088/1468-6996/9/1/014105 (2008).

85. Liu, L. *et al.* Spin-torque switching with the giant spin hall effect of tantalum. *Science* **336**, 555–558, DOI: 10.1126/science.1218197 (2012).

86. Hao, Q., Chen, W. & Xiao, G. Beta () tungsten thin films: Structure, electron transport, and giant spin hall effect. *Appl. Phys. Lett.* **106**, 182403, DOI: 10.1063/1.4919867 (2015). https://doi.org/10.1063/1.4919867.

87. Niimi, Y. *et al.* Giant spin hall effect induced by skew scattering from bismuth impurities inside thin film cubi alloys. *Phys. Rev. Lett.* **109**, 156602, DOI: 10.1103/PhysRevLett.109.156602 (2012).

88. Zhu, L., Ralph, D. C. & Buhrman, R. A. Highly efficient spin-current generation by the spin hall effect in $au_{1-x}pt_x$. *Phys. Rev. Appl.* **10**, 031001, DOI: 10.1103/PhysRevApplied.10.031001 (2018).

89. Deng, Y., Yang, M., Ji, Y. & Wang, K. Estimating spin hall angle in heavy metal/ferromagnet heterostructures. *J. Magn. Magn. Mater.* **496**, 165920, DOI: https://doi.org/10.1016/j.jmmm.2019.165920 (2020).

90. Hoffmann, A. Spin hall effects in metals. *IEEE Transactions on Magn.* **49**, 5172–5193, DOI: 10.1109/TMAG.2013.2262947 (2013).

91. Kikkawa, J. M. & Awschalom, D. D. Lateral drag of spin coherence in gallium arsenide. *Nature* **397**, 139–141, DOI: 10.1038/16420 (1999).

92. Tserkovnyak, Y., Brataas, A. & Bauer, G. E. W. Enhanced gilbert damping in thin ferromagnetic films. *Phys. Rev. Lett.* **88**, 117601, DOI: 10.1103/PhysRevLett.88.117601 (2002).

93. Heinrich, B. *et al.* Dynamic exchange coupling in magnetic bilayers. *Phys. Rev. Lett.* **90**, 187601, DOI: 10.1103/PhysRevLett.90.187601 (2003).

94. Kim, M., Park, S. J. & Jin, H. Enhancing the spin seebeck effect by controlling interface condition in pt/polycrystalline nickel ferrite slabs. *J. Appl. Phys.* **127**, 085105, DOI: 10.1063/1.5142671 (2020). https://doi.org/10.1063/1.5142671.

95. Tserkovnyak, Y., Brataas, A., Bauer, G. E. W. & Halperin, B. I. Nonlocal magnetization dynamics in ferromagnetic heterostructures. *Rev. Mod. Phys.* **77**, 1375–1421, DOI: 10.1103/RevModPhys.77.1375 (2005).

96. Bender, S. A. & Tserkovnyak, Y. Interfacial spin and heat transfer between metals and magnetic insulators. *Phys. Rev. B* **91**, 140402, DOI: 10.1103/PhysRevB.91.140402 (2015).

97. Adachi, H., ichi Uchida, K., Saitoh, E. & Maekawa, S. Theory of the spin seebeck effect. *Reports on Prog. Phys.* **76**, 036501, DOI: 10.1088/0034-4885/76/3/036501 (2013).

98. Rowe, D. (ed.) *CRC Handbook of Thermoelectrics* (CRC Press, 2018).

99. Seebeck, T. J. Magnetische polarization der metalle und erze durck temperatur-differenz. *Abh. k. Akad. Wiss. Berlin* **265** (1823).

100. Uchida, K. *et al.* Observation of the spin seebeck effect. *Nature* **455**, 778–781, DOI: 10.1038/nature07321 (2008).

101. Jaworski, C. M. *et al.* Observation of the spin-seebeck effect in a ferromagnetic semiconductor. *Nat. Mater.* **9**, 898–903, DOI: 10.1038/nmat2860 (2010).

102. Uchida, K. *et al.* Spin seebeck insulator. *Nat. Mater.* **9**, 894–897, DOI: 10.1038/nmat2856 (2010).

103. Uchida, K.-i. *et al.* Observation of longitudinal spin-seebeck effect in magnetic insulators. *Appl. Phys. Lett.* **97**, 172505, DOI: 10.1063/1.3507386 (2010). https://doi.org/10.1063/1.3507386.

104. Schmid, M. *et al.* Transverse spin seebeck effect versus anomalous and planar nernst effects in permalloy thin films. *Phys. Rev. Lett.* **111**, 187201, DOI: 10.1103/PhysRevLett.111.187201 (2013).

105. Meier, D. *et al.* Longitudinal spin seebeck effect contribution in transverse spin seebeck effect experiments in pt/YIG and pt/NFO. *Nat. Commun.* **6**, DOI: 10.1038/ncomms9211 (2015).

106. Uchida, K. *et al.* Thermal spin pumping and magnon-phonon-mediated spin-seebeck effect. *J. Appl. Phys.* **111**, 103903, DOI: 10.1063/1.4716012 (2012).

107. Behnia, K. & Aubin, H. Nernst effect in metals and superconductors: a review of concepts and experiments. *Reports on Prog. Phys.* **79**, 046502, DOI: 10.1088/0034-4885/79/4/046502 (2016).

108. Xiao, J., Bauer, G. E. W., Uchida, K.-c., Saitoh, E. & Maekawa, S. Theory of magnon-driven spin seebeck effect. *Phys. Rev. B* **81**, 214418, DOI: 10.1103/PhysRevB.81.214418 (2010).

109. Sanders, D. J. & Walton, D. Effect of magnon-phonon thermal relaxation on heat transport by magnons. *Phys. Rev. B* **15**, 1489–1494, DOI: 10.1103/PhysRevB.15.1489 (1977).

110. Foros, J., Brataas, A., Tserkovnyak, Y. & Bauer, G. E. W. Magnetization noise in magnetoelectronic nanostructures. *Phys. Rev. Lett.* **95**, 016601, DOI: 10.1103/PhysRevLett.95.016601 (2005).

111. Brataas, A., Nazarov, Y. V. & Bauer, G. E. W. Finite-element theory of transport in ferromagnet–normal metal systems. *Phys. Rev. Lett.* **84**, 2481–2484, DOI: 10.1103/PhysRevLett.84.2481 (2000).

112. Xia, K., Kelly, P. J., Bauer, G. E. W., Brataas, A. & Turek, I. Spin torques in ferromagnetic/normal-metal structures. *Phys. Rev. B* **65**, 220401, DOI: 10.1103/PhysRevB.65.220401 (2002).

113. Dolui, K., Bajpai, U. & Nikolić, B. K. Effective spin-mixing conductance of topological-insulator/ferromagnet and heavy-metal/ferromagnet spin-orbit-coupled interfaces: A first-principles floquet-nonequilibrium green function approach. *Phys. Rev. Mater.* **4**, 121201, DOI: 10.1103/PhysRevMaterials.4.121201 (2020).

114. Vlietstra, N. *et al.* Exchange magnetic field torques in yig/pt bilayers observed by the spin-hall magnetoresistance. *Appl. Phys. Lett.* **103**, 032401, DOI: 10.1063/1.4813760 (2013). https://doi.org/10.1063/1.4813760.

115. Weiler, M. *et al.* Experimental test of the spin mixing interface conductivity concept. *Phys. Rev. Lett.* **111**, 176601, DOI: 10.1103/PhysRevLett.111.176601 (2013).

116. Landau, L. D. & Lifshitz, E. On the theory of the dispersion of magnetic permeability in ferromagnetic bodies. *Phys. Z. Sowjet.* **8**, 153 (1935).

117. Gilbert, T. L. A phenomenological theory of damping in ferromagnetic materials. *IEEE Transactions on Magn.* **40**, 3443–3449, DOI: 10.1109/TMAG.2004.836740 (2004).

118. Harder, M., Gui, Y. & Hu, C.-M. Electrical detection of magnetization dynamics via spin rectification effects. *Phys. Reports* **661**, 1–59, DOI: https://doi.org/10.1016/j.physrep.2016.10.002 (2016). Electrical detection of magnetization dynamics via spin rectification effects.

119. Kittel, C. On the theory of ferromagnetic resonance absorption. *Phys. Rev.* **73**, 155–161, DOI: 10.1103/PhysRev.73.155 (1948).

120. Sun, Y. & Wu, M. Chapter six - yttrium iron garnet nano films: Epitaxial growth, spin-pumping efficiency, and pt-capping-caused damping. In Wu, M. & Hoffmann, A. (eds.) *Recent Advances in Magnetic Insulators – From Spintronics to Microwave Applications*, vol. 64 of *Solid State Physics*, 157–191, DOI: https://doi.org/10.1016/B978-0-12-408130-7.00006-X (Academic Press, 2013).

121. Heinrich, B. & Cochran, J. Ultrathin metallic magnetic films: magnetic anisotropies and exchange interactions. *Adv. Phys.* **42**, 523–639, DOI: 10.1080/00018739300101524 (1993). https://doi.org/10.1080/00018739300101524.

122. Mizukami, S., Ando, Y. & Miyazaki, T. Effect of spin diffusion on gilbert damping for a very thin permalloy layer in cu/permalloy/cu/pt films. *Phys. Rev. B* **66**, 104413, DOI: 10.1103/PhysRevB.66.104413 (2002).

123. Kalarickal, S. S. *et al.* Ferromagnetic resonance linewidth in metallic thin films: Comparison of measurement methods. *J. Appl. Phys.* **99**, 093909, DOI: 10.1063/1.2197087 (2006). https://doi.org/10.1063/1.2197087.

124. Heinrich, B. *et al.* Spin pumping at the magnetic insulator (yig)/normal metal (au) interfaces. *Phys. Rev. Lett.* **107**, 066604, DOI: 10.1103/PhysRevLett.107.066604 (2011).

125. Celinski, Z., Urquhart, K. & Heinrich, B. Using ferromagnetic resonance to measure the magnetic moments of ultrathin films. *J. Magn. Magn. Mater.* **166**, 6–26, DOI: https://doi.org/10.1016/S0304-8853(96)00428-3 (1997).

126. Zakeri, K. *et al.* Spin dynamics in ferromagnets: Gilbert damping and two-magnon scattering. *Phys. Rev. B* **76**, 104416, DOI: 10.1103/PhysRevB.76.104416 (2007).

127. Krivosik, P., Mo, N., Kalarickal, S. & Patton, C. E. Hamiltonian formalism for two magnon scattering microwave relaxation: Theory and applications. *J. Appl. Phys.* **101**, 083901, DOI: 10.1063/1.2717084 (2007). https://doi.org/10.1063/1.2717084.

128. Zhu, L., Zhu, L., Ralph, D. & Buhrman, R. Origin of strong two-magnon scattering in heavy-metal/ferromagnet/oxide heterostructures. *Phys. Rev. Appl.* **13**, 034038, DOI: 10.1103/PhysRevApplied.13.034038 (2020).

129. Anjan Barman, J. S. a. Spin dynamics and damping in ferromagnetic thin films and nanostructures. DOI: 10.1007/978-3-319-66296-1 (2018).

130. Kurebayashi, H. *et al.* Uniaxial anisotropy of two-magnon scattering in an ultrathin epitaxial fe layer on gaas. *Appl. Phys. Lett.* **102**, 062415, DOI: 10.1063/1.4792269 (2013). https://doi.org/10.1063/1.4792269.

131. Sparks, M. *Ferromagnetic-relaxation Theory*. McGraw-Hill advanced physics monograph series (McGraw-Hill, 1964).

132. Lindner, J. *et al.* Two-magnon damping in thin films in case of canted magnetization: Theory versus experiment. *Phys. Rev. B* **80**, 224421, DOI: 10.1103/PhysRevB.80.224421 (2009).

133. Lenz, K. *et al.* Two-magnon scattering and viscous gilbert damping in ultrathin ferromagnets. *Phys. Rev. B* **73**, 144424, DOI: 10.1103/PhysRevB.73.144424 (2006).

134. Arias, R. & Mills, D. L. Extrinsic contributions to the ferromagnetic resonance response of ultrathin films. *Phys. Rev. B* **60**, 7395–7409, DOI: 10.1103/PhysRevB.60.7395 (1999).

135. Xue, X. *et al.* Voltage control of two-magnon scattering and induced anomalous magnetoelectric coupling in ni–zn ferrite. *ACS Appl. Mater. & Interfaces* **9**, 43188–43196, DOI: 10.1021/acsami.7b15433 (2017). PMID: 29171255, https://doi.org/10.1021/acsami.7b15433.

136. Bhatti, S. *et al.* Spintronics based random access memory: a review. *Mater. Today* **20**, 530–548, DOI: https://doi.org/10.1016/j.mattod.2017.07.007 (2017).

137. Hurben, M. J. & Patton, C. E. Theory of two magnon scattering microwave relaxation and ferromagnetic resonance linewidth in magnetic thin films. *J. Appl. Phys.* **83**, 4344–4365, DOI: 10.1063/1.367194 (1998). https://doi.org/10.1063/1.367194.

138. Bertaut, F. & Forrat, F. Structure des ferrites ferrimagnetiques des terres rares. *Comptes Rendus Hebdomadaires Des Seances De L Acad. Des Sci.* **242**, 382–384 (1956).

139. Sokolov, N. S. *et al.* Thin yttrium iron garnet films grown by pulsed laser deposition: Crystal structure, static, and dynamic magnetic properties. *J. Appl. Phys.* **119**, 023903, DOI: 10.1063/1.4939678 (2016).

140. A.K. Zvezdin, V. K. *Modern Magnetooptics and Magnetooptical Materials* (Taylor Francis, 1997), 1 edn.

141. Princep, A. J. *et al.* The full magnon spectrum of yttrium iron garnet. *npj Quantum Mater.* **2**, DOI: 10.1038/s41535-017-0067-y (2017).

142. Momma, K. & Izumi, F. *VESTA3* for three-dimensional visualization of crystal, volumetric and morphology data. *J. Appl. Crystallogr.* **44**, 1272–1276, DOI: 10.1107/S0021889811038970 (2011).

143. Wu, M. Nonlinear spin waves in magnetic film feedback rings. In *Solid State Physics*, 163–224, DOI: 10.1016/b978-0-12-374293-3.00003-1 (Elsevier, 2010).

144. Pardavi-Horvath, M. Microwave applications of soft ferrites. *J. Magn. Magn. Mater.* **215-216**, 171–183, DOI: 10.1016/s0304-8853(00)00106-2 (2000).

145. Haubenreisser, W. Physics of magnetic garnets. a. paoletti (ed.). proceedings of the international school of physics „enrico fermi". *Kristall und Tech.* **14**, 1490–1490, DOI: https://doi.org/10.1002/crat.19790141215 (1979). https://onlinelibrary.wiley.com/doi/pdf/10.1002/crat.19790141215.

146. Serga, A. A., Chumak, A. V. & Hillebrands, B. YIG magnonics. *J. Phys. D: Appl. Phys.* **43**, 264002, DOI: 10.1088/0022-3727/43/26/264002 (2010).

147. Chikazumi, S. & Graham, C. *Physics of Ferromagnetism 2e*. International Series of Monographs on Physics (OUP Oxford, 2009).

148. Stancil, D. D. & Prabhakar, A. *Spin Waves* (Springer US, 2009).

149. Dubs, C. *et al.* Low damping and microstructural perfection of sub-40nm-thin yttrium iron garnet films grown by liquid phase epitaxy. *Phys. Rev. Mater.* **4**, 024416, DOI: 10.1103/PhysRevMaterials.4.024416 (2020).

150. Onbasli, M. C. *et al.* Pulsed laser deposition of epitaxial yttrium iron garnet films with low gilbert damping and bulk-like magnetization. *APL Mater.* **2**, 106102, DOI: 10.1063/1.4896936 (2014). https://doi.org/10.1063/1.4896936.

151. Ding, J., Liu, T., Chang, H. & Wu, M. Sputtering growth of low-damping yttrium-iron-garnet thin films. *IEEE Magn. Lett.* **11**, 1–5, DOI: 10.1109/LMAG.2020.2989687 (2020).

152. Manuilov, S. A., Khartsev, S. I. & Grishin, A. M. Pulsed laser deposited y3fe5o12 films: Nature of magnetic anisotropy i. *J. Appl. Phys.* **106**, 123917, DOI: 10.1063/1.3272731 (2009). https://doi.org/10.1063/1.3272731.

153. Bhoi, B. *et al.* Stress-induced magnetic properties of pld-grown high-quality ultrathin yig films. *J. Appl. Phys.* **123**, 203902, DOI: 10.1063/1.5031198 (2018). https://doi.org/10.1063/1.5031198.

154. Willmott, P. R. & Huber, J. R. Pulsed laser vaporization and deposition. *Rev. Mod. Phys.* **72**, 315–328, DOI: 10.1103/RevModPhys.72.315 (2000).

155. Mihailescu, I. N. & Caricato, A. P. (eds.) *Pulsed Laser Ablation: advances and Applicationsin Nanoparticles and Nanostructuring Thin Films* (Pan Stanford, 2018).

156. Huang, S. Y. *et al.* Transport magnetic proximity effects in platinum. *Phys. Rev. Lett.* **109**, 107204, DOI: 10.1103/PhysRevLett.109.107204 (2012).

157. Fache, T., Rojas-Sanchez, J. C., Badie, L., Mangin, S. & Petit-Watelot, S. Determination of spin hall angle, spin mixing conductance, and spin diffusion length in cofeb/ir for spin-orbitronic devices. *Phys. Rev. B* **102**, 064425, DOI: 10.1103/PhysRevB.102.064425 (2020).

158. Braun, M. Magnetron sputtering technique. In *Handbook of Manufacturing Engineering and Technology*, 2929–2957, DOI: 10.1007/978-1-4471-4670-4_28 (Springer London, 2014).

159. Rossnagel, S. M. Magnetron sputtering. *J. Vac. Sci. & Technol. A* **38**, 060805, DOI: 10.1116/6.0000594 (2020). https://doi.org/10.1116/6.0000594.

160. Birkholz, M. *Thin film analysis by X-ray scattering* (Wiley-VCH, 2006).

161. Epp, J. 4 - x-ray diffraction (xrd) techniques for materials characterization. In Hübschen, G., Altpeter, I., Tschuncky, R. & Herrmann, H.-G. (eds.) *Materials Characterization Using Nondestructive Evaluation (NDE) Methods*, 81–124, DOI:

https://doi.org/10.1016/B978-0-08-100040-3.00004-3 (Woodhead Publishing, 2016).

162. Hecht, E. *Optics* (Addison Wesley, 2002), 4 edn.

163. Oliver H. Seeck, B. M. *X-Ray Diffraction: Modern Experimental Techniques* (Pan Stanford, 2014), 1 edn.

164. Lee, A. J., Guo, S., Ahmed, A. S. & Yang, F. Crystal orientation dependence of interfacial magnetic anisotropy at heavy-metal/magnetic-garnet interfaces. *Phys. Rev. B* **102**, 174434, DOI: 10.1103/PhysRevB.102.174434 (2020).

165. Linker, G. *et al.* The growth of ultra-thin epitaxial ceo2 films on r-plane sapphire. *Thin Solid Films* **471**, 320–327, DOI: https://doi.org/10.1016/j.tsf.2004.05.126 (2005).

166. Switzer, J. A., Hill, J. C., Mahenderkar, N. K. & Liu, Y.-C. Nanometer-thick gold on silicon as a proxy for single-crystal gold for the electrodeposition of epitaxial cuprous oxide thin films. *ACS Appl. Mater. & Interfaces* **8**, 15828–15837, DOI: 10.1021/acsami.6b04552 (2016).

167. B.D. Cullity, S. S. *Elements of X-Ray Diffraction* (Pearson Education Limited, 2014), third edn.

168. Su, T., Ning, S., Cho, E. & Ross, C. A. Magnetism and site occupancy in epitaxial y-rich yttrium iron garnet films. *Phys. Rev. Mater.* **5**, 094403, DOI: 10.1103/PhysRevMaterials.5.094403 (2021).

169. Brune, H. & Kern, K. Chapter 5 heteroepitaxial metal growth: the effects of strain. In King, D. & Woodruff, D. (eds.) *Growth and Properties of Ultrathin Epitaxial Layers*, vol. 8 of *The Chemical Physics of Solid Surfaces*, 149–206, DOI: https://doi.org/10.1016/S1571-0785(97)80008-9 (Elsevier, 1997).

170. Cooper, D., Denneulin, T., Bernier, N., Béché, A. & Rouvière, J.-L. Strain mapping of semiconductor specimens with nm-scale resolution in a transmission electron microscope. *Micron* **80**, 145–165, DOI: https://doi.org/10.1016/j.micron.2015.09.001 (2016).

171. Krichevtsov, B. B. *et al.* Magnetization reversal in yig/ggg(111) nanoheterostructures grown by laser molecular beam epitaxy. *Sci. Technol. Adv. Mater.* **18**, 351–363, DOI: 10.1080/14686996.2017.1316422 (2017). PMID: 28685003, https://doi.org/10.1080/14686996.2017.1316422.

172. Łopuszyński, M. & Majewski, J. A. Ordering in ternary nitride semiconducting alloys. *Phys. Rev. B* **85**, 035211, DOI: 10.1103/PhysRevB.85.035211 (2012).

173. d'Allivy Kelly, O. *et al.* Inverse spin hall effect in nanometer-thick yttrium iron garnet/pt system. *Appl. Phys. Lett.* **103**, 082408, DOI: 10.1063/1.4819157 (2013). https://doi.org/10.1063/1.4819157.

174. Howe, B. M. *et al.* Pseudomorphic yttrium iron garnet thin films with low damping and inhomogeneous linewidth broadening. *IEEE Magn. Lett.* **6**, 1–4, DOI: 10.1109/LMAG.2015.2449260 (2015).

175. Suturin, S. M. *et al.* Role of gallium diffusion in the formation of a magnetically dead layer at the $y_3fe_5o_{12}/gd_3ga_5o_{12}$ epitaxial interface. *Phys. Rev. Mater.* **2**, 104404, DOI: 10.1103/PhysRevMaterials.2.104404 (2018).

176. Tan, S., Zhang, W., Yang, L., Chen, J. & Wang, Z. Intrinsic defects in yttrium iron garnet: A first-principles study. *J. Appl. Phys.* **128**, 183904, DOI: 10.1063/5.0021862 (2020). https://doi.org/10.1063/5.0021862.

177. Jens Als-Nielsen, D. M. *Elements of Modern X-ray Physics* (Wiley, 2011), 2nd ed. edn.

178. Chandran, S., Begam, N. & Basu, J. K. Dispersion of polymer grafted nanoparticles in polymer nanocomposite films: Insights from surface x-ray scattering and microscopy. *J. Appl. Phys.* **116**, 222203, DOI: 10.1063/1.4902964 (2014). https://doi.org/10.1063/1.4902964.

179. Petty, M. C. *Molecular Electronics: From Principles to Practice (Wiley Series in Materials for Electronic Optoelectronic Applications)*. Wiley Series in Materials for Electronic Optoelectronic Applications (Wiley-Interscience, 2008), 1 edn.

180. Kiessig, H. Interferenz von röntgenstrahlen an dünnen schichten. *Annalen der Physik* **402**, 769–788, DOI: https://doi.org/10.1002/andp.19314020702 (1931). https://onlinelibrary.wiley.com/doi/pdf/10.1002/andp.19314020702.

181. Ying, A. J., Murray, C. E. & Noyan, I. C. A rigorous comparison of x-ray diffraction thickness measurement techniques using silicon-on-insulator thin films. *J. Appl. Crystallogr.* **42**, 401–410, DOI: https://doi.org/10.1107/S0021889809006888 (2009). https://onlinelibrary.wiley.com/doi/pdf/10.1107/S0021889809006888.

182. Kago, K. *et al.* Characterization of thin polymer films by x-ray reflectometry with synchrotron radiation. *J. Synchrotron Radiat.* **5**, 1304–1308, DOI: https://doi.org/10.1107/S0909049598006797 (1998). https://onlinelibrary.wiley.com/doi/pdf/10.1107/S0909049598006797.

183. F. de Bergevin (auth.), A. G. e., Jean Daillant. *X-ray and Neutron Reflectivity: Principles and Applications*. Lecture Notes in Physics 770 (Springer-Verlag Berlin Heidelberg, 2009), 1 edn.

184. Chantler, C. T. Theoretical form factor, attenuation, and scattering tabulation for z=1–92 from e=1–10 ev to e=0.4–1.0 mev. *J. Phys. Chem. Ref. Data* **24**, 71–643, DOI: 10.1063/1.555974 (1995). https://doi.org/10.1063/1.555974.

185. The atomic scattering factor files. Berkeley Lab, http://henke.lbl.gov/optical_constants/asf.html.

186. Chantler, C. T. *et al.* X-ray form factor, attenuation and scattering tables (version 2.1) (2005). https://physics.nist.gov/PhysRefData/FFast/html/form.html.

187. Mecking, N., Gui, Y. S. & Hu, C.-M. Microwave photovoltage and photoresistance effects in ferromagnetic microstrips. *Phys. Rev. B* **76**, 224430, DOI: 10.1103/PhysRevB.76.224430 (2007).

188. Fukui, N. *et al.* Ferromagnetic-resonance induced electromotive forces in ni81fe19 | p-type diamond. *Solid State Commun.* **243**, 44–48, DOI: https://doi.org/10.1016/j.ssc.2016.06.001 (2016).

189. Sun, Y., Song, Y.-Y. & Wu, M. Growth and ferromagnetic resonance of yttrium iron garnet thin films on metals. *Appl. Phys. Lett.* **101**, 082405, DOI: 10.1063/1.4747465 (2012). https://doi.org/10.1063/1.4747465.

190. Kurebayashi, H. *et al.* Controlled enhancement of spin-current emission by three-magnon splitting. *Nat. Mater.* **10**, 660–664, DOI: 10.1038/nmat3053 (2011).

191. Haertinger, M. *et al.* Spin pumping in yig/pt bilayers as a function of layer thickness. *Phys. Rev. B* **92**, 054437, DOI: 10.1103/PhysRevB.92.054437 (2015).

192. Lax, B. & Button, K. J. *Microwave ferrites and ferrimagnetics*. Lincoln Laboratory publications. (McGraw-Hill, New York, 1962). 752 p.

193. Gallagher, J. C. *et al.* Exceptionally high magnetization of stoichiometric y3fe5o12 epitaxial films grown on gd3ga5o12. *Appl. Phys. Lett.* **109**, 072401, DOI: 10.1063/1.4961371 (2016). https://doi.org/10.1063/1.4961371.

194. Hahn, C. *et al.* Measurement of the intrinsic damping constant in individual nanodisks of y3fe5o12 and y3fe5o12|pt. *Appl. Phys. Lett.* **104**, 152410, DOI: 10.1063/1.4871516 (2014). https://doi.org/10.1063/1.4871516.

195. Gurjar, G., Sharma, V., Patnaik, S. & Kuanr, B. K. Control of magnetization dynamics by substrate orientation in YIG thin films. *Mater. Res. Express* **8**, 066401, DOI: 10.1088/2053-1591/ac0311 (2021).

196. Sakimura, H. *et al.* Enhancement of two-magnon scattering induced by a randomly distributed antiferromagnetic exchange field. *Phys. Rev. B* **98**, 144406, DOI: 10.1103/PhysRevB.98.144406 (2018).

197. Dubs, C. *et al.* Sub-micrometer yttrium iron garnet LPE films with low ferromagnetic resonance losses. *J. Phys. D: Appl. Phys.* **50**, 204005, DOI: 10.1088/1361-6463/aa6b1c (2017).

198. Hamadeh, A. *et al.* Full control of the spin-wave damping in a magnetic insulator using spin-orbit torque. *Phys. Rev. Lett.* **113**, 197203, DOI: 10.1103/PhysRevLett.113.197203 (2014).

199. Conca, A., Keller, S., Schweizer, M. R., Papaioannou, E. T. & Hillebrands, B. Separation of the two-magnon scattering contribution to damping for the de-

termination of the spin mixing conductance. *Phys. Rev. B* **98**, 214439, DOI: 10.1103/PhysRevB.98.214439 (2018).

200. Peria, W. K. *et al.* Interplay of large two-magnon ferromagnetic resonance linewidths and low gilbert damping in heusler thin films. *Phys. Rev. B* **101**, 134430, DOI: 10.1103/PhysRevB.101.134430 (2020).

201. Sposito, A., May-Smith, T. C., Stenning, G. B. G., de Groot, P. A. J. & Eason, R. W. Pulsed laser deposition of high-quality μm-thick yig films on yag. *Opt. Mater. Express* **3**, 624–632, DOI: 10.1364/OME.3.000624 (2013).

202. Krysztofik, A., Özoğlu, S., McMichael, R. D. & Coy, E. Effect of strain-induced anisotropy on magnetization dynamics in y3fe5o12 films recrystallized on a lattice-mismatched substrate. *Sci. Reports* **11**, 14011, DOI: 10.1038/s41598-021-93308-3 (2021).

203. Popova, E. *et al.* Interplay between epitaxial strain and low dimensionality effects in a ferrimagnetic oxide. *J. Appl. Phys.* **121**, 115304, DOI: 10.1063/1.4978508 (2017). https://doi.org/10.1063/1.4978508.

204. Markov, I. V. *Crystal Growth For Beginners. Fundamentals of Nucleation, Crystal Growth and Epitaxy* (World Scientific, 2017), 3 edn.

205. Yasaka, M. X-ray thin-film measurement techniques v . x-ray reflectivity measurement (2010).

206. Weiler, M. *et al.* Local charge and spin currents in magnetothermal landscapes. *Phys. Rev. Lett.* **108**, 106602, DOI: 10.1103/PhysRevLett.108.106602 (2012).

207. Wang, S., Li, G., Wang, J., Yan, H. & Jin, K. Laser-heating spin seebeck effect of yttrium iron garnet/platinum heterostructure below room temperature. *J. Magn. Magn. Mater.* **468**, 50–55, DOI: https://doi.org/10.1016/j.jmmm.2018.07.076 (2018).

208. Schreier, M. *et al.* Current heating induced spin seebeck effect. *Appl. Phys. Lett.* **103**, 242404, DOI: 10.1063/1.4839395 (2013). https://doi.org/10.1063/1.4839395.

209. Vlietstra, N. *et al.* Simultaneous detection of the spin-hall magnetoresistance and the spin-seebeck effect in platinum and tantalum on yttrium iron garnet. *Phys. Rev. B* **90**, 174436, DOI: 10.1103/PhysRevB.90.174436 (2014).

210. Wu, S. M., Fradin, F. Y., Hoffman, J., Hoffmann, A. & Bhattacharya, A. Spin seebeck devices using local on-chip heating. *J. Appl. Phys.* **117**, 17C509, DOI: 10.1063/1.4916188 (2015). https://doi.org/10.1063/1.4916188.

211. Chen, Y. *et al.* First harmonic measurements of the spin seebeck effect. *Appl. Phys. Lett.* **113**, 202403, DOI: 10.1063/1.5053120 (2018). https://doi.org/10.1063/1.5053120.

212. Collet, M. *et al.* Spin seebeck effect in nanometer-thick yig micro-fabricated strips. *AIP Adv.* **7**, 055924, DOI: 10.1063/1.4976332 (2017). https://doi.org/10.1063/1.4976332.

213. Nakayama, H. *et al.* Spin hall magnetoresistance induced by a nonequilibrium proximity effect. *Phys. Rev. Lett.* **110**, 206601, DOI: 10.1103/PhysRevLett.110.206601 (2013).

214. Wang, W. X. *et al.* Joule heating-induced coexisted spin seebeck effect and spin hall magnetoresistance in the platinum/y3fe5o12 structure. *Appl. Phys. Lett.* **105**, 182403, DOI: 10.1063/1.4901101 (2014). https://doi.org/10.1063/1.4901101.

215. Romanque-Albornoz, C., Gonzalez-Fuentes, C., Orellana, C. & Garcia, C. Spin seebeck effect detection by harmonic analysis. *Appl. Phys. Lett.* **116**, 242402, DOI: 10.1063/5.0011413 (2020). https://doi.org/10.1063/5.0011413.

216. Uchida, K. *et al.* Longitudinal spin seebeck effect: from fundamentals to applications. *J. Physics: Condens. Matter* **26**, 343202, DOI: 10.1088/0953-8984/26/34/343202 (2014).

217. Alkin, O. *Signals and Systems: A MATLAB Integrated Approach* (CRC Press, Inc., USA, 2014).

218. Thorn, P. H. S. R. *Handbook of Measuring System Design [3 Vols]* (Wiley, 2005).

219. Bhattacharyya, S., Ahmed, R. N., Purkayastha, B. B. & Bhattacharyya, K. Implementation of digital lock-in amplifier. *J. Physics: Conf. Ser.* **759**, 012096, DOI: 10.1088/1742-6596/759/1/012096 (2016).

220. Imamura, M., Asada, H., Tashima, D. & Kitagawa, J. Spin-thermoelectric voltage in longitudinal sse elements incorporating lpe yig films and polycrystalline yig slabs with an ultrathin pt layer. *Electr. Eng. Jpn.* **208**, 10–20, DOI: 10.1002/eej.23232 (2019). https://onlinelibrary.wiley.com/doi/pdf/10.1002/eej.23232.

221. Kirihara, A. *et al.* Spin-current-driven thermoelectric coating. *Nat. Mater.* **11**, 686–689, DOI: 10.1038/nmat3360 (2012).

222. Morrison, K., Caruana, A. J. & Cox, C. Scaling of the spin seebeck effect in bulk and thin film, DOI: 10.48550/ARXIV.1705.02491 (2017).

223. Iguchi, R., Uchida, K.-i., Daimon, S. & Saitoh, E. Concomitant enhancement of the longitudinal spin seebeck effect and the thermal conductivity in a pt/yig/pt system at low temperatures. *Phys. Rev. B* **95**, 174401, DOI: 10.1103/PhysRevB.95.174401 (2017).

224. Sola, A. *et al.* Longitudinal spin seebeck coefficient: heat flux vs. temperature difference method. *Sci. Reports* **7**, DOI: 10.1038/srep46752 (2017).

225. Sola, A. *et al.* Spincaloritronic measurements: A round robin comparison of the longitudinal spin seebeck effect. *IEEE Transactions on Instrumentation Meas.* **68**, 1765–1773 (2019).

226. Lacy, F. Developing a theoretical relationship between electrical resistivity, temperature, and film thickness for conductors. *Nanoscale Res. Lett.* **6**, 636, DOI: 10.1186/1556-276X-6-636 (2011).

227. Xu, Y., Zhao, W. & Mangin, S. Frequency dependence of the longitudinal spin seebeck effect. *Phys. Rev. B* **98**, 144408, DOI: 10.1103/PhysRevB.98.144408 (2018).

228. Schreier, M. *et al.* Spin seebeck effect at microwave frequencies. *Phys. Rev. B* **93**, 224430, DOI: 10.1103/PhysRevB.93.224430 (2016).

229. Vaterlaus, A., Beutler, T. & Meier, F. Spin-lattice relaxation time of ferromagnetic gadolinium determined with time-resolved spin-polarized photoemission. *Phys. Rev. Lett.* **67**, 3314–3317, DOI: 10.1103/PhysRevLett.67.3314 (1991).

230. Cruickshank, D. *Microwave Materials for Wireless Applications*. Artech House microwave library (Artech House, 2011).

231. Tian, G., Yang, W. D., Gao, X. S. & Liu, J.-M. Emerging phenomena from exotic ferroelectric topological states. *APL Mater.* **9**, 020907, DOI: 10.1063/5.0039139 (2021). https://doi.org/10.1063/5.0039139.

232. Dieny, B. *et al.* Opportunities and challenges for spintronics in the microelectronics industry. *Nat. Electron.* **3**, 446–459, DOI: 10.1038/s41928-020-0461-5 (2020).